Combined Experimental and Modeling Study of the Interactions of Acid Gas with Common Spacecraft Surfaces for Fire Safety Applications

Dissertation

Presented in Partial Fulfillment of the Requirements for the Degree Doctor of Philosophy in the Graduate School of The Ohio State University

By

Justin Niehaus, M.S., B.S.

Graduate Program in Aerospace Engineering

The Ohio State University

2023

Dissertation Committee:

Dr. Sandip Mazumder

Dr. Jeffrey Bons

Dr. Hyun Seung Kim

Dr. Barbara Wyslouzil

Abstract

A fire in a spacecraft poses detrimental consequences and risks mission success in addition to crew safety. This is compounded during long-duration missions when the crew has limited options to recover from a fire. A common spacecraft fire concern is the smoldering of wire insulation, typically made from Polyvinyl chloride (PVC) or Polytetrafluoroethylene (PTFE). This creates acid gases such as Hydrogen Chloride (HCl), Hydrogen Fluoride (HF) and Hydrogen Cyanide (HCN). These poisonous gases are hazardous to the crew. They also interact with common surfaces within the spacecraft more than dominant combustion products such as CO_2 and H_2O. This makes them more difficult to track for potential fire detection techniques, or for post-fire clean-up. It is imperative to be able to understand and predict the fate of these poisonous species in a microgravity environment in order to design a safe vehicle.

HCl interacts with a number of materials inside a spacecraft. Primary among these materials is aluminum, which is abundantly used due to its strong and light weight nature. Aluminum has a natural oxide layer that protects it from corrosion but is typically treated to enhance this oxide layer. Among these treatments is a chromate conversion coating (CCC), which provides a thin enough protective oxide layer to still conduct electricity, and a traditional anodized material that has a thicker oxide layer that does not conduct electricity. Nomex is another common material found inside a spacecraft. It is a flame-resistant woven polymer that is related to nylon. This commercially available material is used for cargo storage bags and as a fire barrier.

Physics-based models were developed to predict the uptake of HCl by these materials. The ultimate objective of these models is to predict the fate of HCl within the spacecraft so that sensors

can be placed in meaningful locations in future missions based on the model predictions. To support these modeling efforts, experiments were performed in a cast acrylic test cell that measured the difference between the inlet and outlet concentration of HCl after inserting a sample rod of the test material. Different uptake capacities were realized for each type of sample tested. A computational fluid dynamics model (CFD) model of the reactor was then constructed that used a one-step global reaction rate with calibratable reaction (or kinetic) constants. These constants were calibrated to match the HCl uptake on the CCC aluminum samples, and the same kinetic constants were then tested for the stock and anodized aluminum samples. Model predictions matched the experimental data for the stock aluminum, and to a much lesser extent, the anodized aluminum. The model was additionally validated at different flow rates, sample surface areas, and inlet concentrations, and showed good agreement for all stock and CCC samples.

The model did not accurately predict the HCl uptake in the anodized samples compared to the other two types of aluminum. Adjusting the kinetic constants and transport properties did little to improve the prediction. X-Ray Photoelectron Spectroscopy (XPS) was used to determine that the oxide layer thickness of anodized aluminum is approximately 5,000 nm, compared to 250 nm for CCC and 50 nm for stock. XPS also revealed presence of chlorine further down in the aluminum oxide layer in anodized samples than CCC and stock samples after the samples were saturated with HCl, indicating that accounting for diffusion of HCl into the oxide layer is important for accurate prediction of HCl uptake onto anodized aluminum. Consequently, a multi-scale model was developed and tested. First, a single pore inside the anodized aluminum oxide layer was modeled and is referred to as the *pore-scale* model. In this model, HCl diffused through the pore and reacted with the aluminum oxide pore wall to create aluminum chloride. The sample was then saturated when the mass transfer resistance through the growing aluminum chloride layer became

too large for the HCl to reach the aluminum oxide wall and continue the reaction. This pore-scale model was coupled to the reactor-scale model using a concentration-dependent diffusion coefficient, resulting in much more accurate predictions (approximately half the sum square error of the aforementioned reactor-scale model that produced good agreement for stock and CCC) for a variety of operating conditions.

The amount of water vapor or relative humidity (RH) in the flow during a reactor experiment was determined to influence HCl uptake. Experiments were performed to understand the interaction of gaseous HCl with aluminum surfaces in the presence of water vapor. The results show that increasing levels of RH increased the capacity of aluminum to adsorb HCl but decreased the capacity of Nomex to uptake HCl. A series of tests were performed on individual aluminum samples after they had been saturated with a fixed concentration of HCl in dry air conditions with the goal of determining how their HCl uptake capacity changes after various treatments with water relative to the original saturation tests. HCl-saturated aluminum samples subjected to a second dry air flow at the same HCl concentration as the original test had an uptake of 23.5% of the original sample with no treatment in between. Saturated aluminum samples subjected to an air flow with a RH of 90% in between tests had an uptake of 35.6% of the original. Saturated aluminum samples submerged in distilled water for 12 hours in between tests had an uptake of 82.2% of the original sample. Previously saturated aluminum tested with HCl and a 50% RH air flow resulted in similar uptake characteristics in multiple repeated tests. The experiments show the profound effect water vapor has on HCl uptake onto aluminum surfaces.

In the samples subjected to water vapor or liquid water, capillary condensation and capillary diffusion alters the transport of HCl significantly. A model was proposed that developed a relationship between RH and the coefficient of HCl diffusion in aluminum chloride. This produced an “S-shaped” curve with diffusion coefficient as a function of RH, with 45% RH represented as the point where the diffusion coefficient is halfway between no water saturation and 100% water saturation in the aluminum chloride product layer. No difference in uptake characteristics for the experiment or model were realized between 50% and 62% RH.

The results from the large-scale microgravity experiment, Saffire, are discussed as they pertain to the fate of HCl throughout a spacecraft. HCl was released, both as a standalone event, and in concurrence with the burning of a structured cloth. These events only produced a small response in the far field HCl sensor, while a PMMA burn that did not produce HCl had a significantly greater response. A ground-based large-scale facility was constructed to flow acid gas at the scale and configuration realized in the Saffire experiments. A CFD model of this duct was constructed to test kinetic parameters developed in this work at a larger scale and different geometric configuration and to predict the results of the large-scale facility. The models developed in this work were used to interpret the results of the microgravity tests and lead the discussion on what further experiments and models are needed in order to predict the fate of acid gas in a spacecraft environment.

To summarize, the major contributions of this work are as follows: the capacity to uptake HCl, with and without the presence of water vapor, was measured for a variety of real spacecraft surfaces. Several different models (single reactor-scale, multiscale, spacecraft-scale) were developed and with the aid of modeling, the rate of uptake for those surfaces was also predicted and validated. The kinetic parameters determined from the small-scale reactor experiments and models were used to predict large-scale and microgravity tests. Conclusions from this research will be used in the design of spacecraft vehicles and large-scale microgravity fire safety experiments. The models built by this work will aid designers in sensor placement and could be

used to predict acid gas transport from fires in partial gravity, as would be seen in Lunar and Martian habitats.

Acknowledgments

First and foremost, I owe much gratitude to my advisor, Dr. Sandip Mazumder, for pushing my research abilities farther than I could have imagined. From making journal-quality figures, to producing high-quality writing I can be proud of, I am now confident in my ability to conduct independent research and think critically about a problem. He is the only professor I have ever had at any education level that will sit down and help debug a code, and I have learned so much about problem solving through that process. The skills I have developed under Dr. Mazumder's advisement will serve me well in my scientific career and life and are things I hope to pass down as a mentor.

I would like to thank Dr. Jeffrey Bons, Dr. Barbara Wyslouzil and Dr. Seung Hyun Kim for serving on my committee. A big thank you is in order for administering my written and oral exams and providing enlightening discussion, especially when I found myself stuck.

My "NASA advisor", Dr. Suleyman Gokoglu was instrumental in moving along my research. I know that I definitely took sharing an office with you for granted, which made our conversations free flowing and easy. But even after the reorganization, you were always available to help.

David Urban and Gary Ruff provided excellent programmatic support, keeping Saffire well-run and funded, and were great advocates for my work and continued education. I would also like to thank Dan Gotti and Dorothy Lukco for their technical support and engineering expertise.

It was an honor to follow in Marit Meyer's and Michael Hicks' footsteps as the combustion representative in NASA's graduate studies program. While watching their struggles and triumphs in their research, they would always joke with me about never pursuing a PhD. But they were both very excited after I was accepted and have provided encouragement even since.

I would like to thank John Easton and Gordon Berger for being excellent lab mates. They kept the lab stocked and safety permits current, especially during long shutdowns. They provided an ear to bounce off research ideas, and more importantly, fantasy football advice.

Finally, my entire family was instrumental in my achievements. My mother Gail Niehaus and father Bob Niehaus provided the work ethic necessary to complete such a long-term project, and the perseverance to never give up. My brother Brandon usually gave me a welcome distraction and worse fantasy football advice, while my sister Shannon welcomed me into her home whenever I was staying in Columbus. My father in law, Dave, mother in law, Sue, and brother in law, John all provided amazing encouragement and support. My wife Kelsey has always had my back through all of this. From the late nights, to giving me the space to work through a problem that was stuck in my head over dinner, she continued to encourage me. During the pandemic, Kelsey and Lucy were great office mates. Finally, Kellan, my first-born child provided the last bit of motivation and inspiration to really push through to the end.

Vita

2005 . . . . William Mason High School,
Mason, OH

2010 . . . . .B.S. Aerospace Engineering,
University of Cincinnati

2010 . . . . M.S. Aerospace Engineering
University of Cincinnati

2011-present . . . . Research Engineer,
NASA Glenn Research Center
Cleveland, OH

Publications

Niehaus, J., Mazumder, S., “Multiscale Modeling of the Uptake of Hydrogen Chloride on Anodized Aluminum in Relevance to Spacecraft Fire Safety,” International Mechanical Engineering Congress and Exposition, IMECE 2022-95243, American Society of Mechanical Engineers, 2022.

Niehaus, J., Mazumder, S., “Multiscale model for Hydrogen Chloride uptake on Aluminum for Spacecraft Fire Safety,” *Journal of Spacecraft and Rockets*, 2023. Under Review

Niehaus, J., Gokoglu, S., Mazumder, S., Berger, G., Easton, J., “Modeling the Uptake of Hydrogen Chloride onto Interior Spacecraft Materials,” 50th International Conference on Environmental Systems, ICES-2021-271, Texas Tech University Libraries, 2021.

Niehaus, J., Gokoglu, S., Mazumder, S., Berger, G., Easton, J., “Effect of Humidity on Surface Interaction of Gaseous HCl and Aluminum for Spacecraft Fire Safety Applications,” International Conference on Environmental Systems, ICES-2020-341, Texas Tech University Libraries, 2020.

Niehaus, J. E., Gokoglu, S. A., Berger, G., Easton, J., & Mazumder, S., “Modeling Hydrogen Chloride and Aluminum Surface Interactions for Spacecraft Fire Safety Applications,” *Journal of Spacecraft and Rockets*, Vol. 57.2, 2020, pp. 217-224.

Niehaus, J., Gokoglu, S., Mazumder, S., Berger, G., Easton, J., “Development and Validation of a Model to Account for Gaseous HCl and Aluminum Surface Interactions for Spacecraft Fire Safety Applications,” 49th International Conference on Environmental Systems, ICES-2019-180, Texas Tech University Libraries, 2019.

Fields of Study

Major Field: Aerospace Engineering

Table of Contents

List of Tables

List of Figures

List of Symbols

A	Pre-exponential factor for global reaction (1/s)
A_w	Local surface area of pore (m^2)
c	Concentration of HCl (mol/m^3)
c_w	Wall or surface concentration of HCl (mol/m^3)
D	Diameter (m)
D_{eff}	Effective diffusion coefficient of HCl (m^2/s)
D_{fluid}	Diffusion coefficient of HCl in fluid (open pore) (m^2/s)
D_{Al2O3}	Diffusion coefficient of HCl in alumina (m^2/s)
D_{AlCl3}	Diffusion coefficient of HCl in aluminum chloride (m^2/s)
D_{rs}	Diffusion coefficient of HCl in air in reactor-scale model (m^2/s)
E_a	Activation energy (J)
k	Reaction rate constant in reactor model (1/s)
k_{pore}	Reaction rate constant in pore model (m/s)
lpm	Liter per minute
M	Molar mass (kg/kmol)
$\dot{m}$	Mass flow rate (kg/s)

m_{AlCl3}	Mass of aluminum chloride deposited on pore wall (kg)
n	Number of test points taken in reactor experiment
r	Radial coordinate (m)
R	Universal gas constant, (J/mol-K)
$\dot{R}$	Reaction rate (kmol/m^3-s)
s	Surface site
Sl	Slope in Eq. 5.2
t	Time (s)
T	Temperature (K)
u	Flow speed (m/s)
$\dot{V}$	Volume flow rate (SLPM)
y	Experimental concentration in reactor (ppm)
$\bar{y}$	Model predicted concentration in reactor model (ppm)
Y	Mass fraction (kg/kg)
z	Axial coordinate (m)

Greek

ε_{Al2O3}	Volume fraction of alumina
ε_{AlCl3}	Volume fraction of aluminum chloride
ε_{fluid}	Volume fraction of fluid (open pore)
v	Kinematic viscosity (m^2/s)
ρ_{site}	Surface site density ($\mu mol/m^2$)
θ	Surface site fraction
μ	Concentration exponent for surface sites

Abbreviations

BET	Brunauer–Emmett–Teller
CCC	Chromate Conversion Coating
CFD	Computational Fluid Dynamics
CSM	Crew Service Module
ccm	cubic centimeters per minute
ECLSS	Environmental Control and Life Support System
FFD	Far Field Device

ISS	International Space Station
lpm	liters per minute
MFC	Mass Flow Controller
NASA	National Aeronautics and Space Administration
NG	Northrop Grumman
PMMA	Poly(methyl methacrylate)
ppm	parts per million
PSIG	Pounds per Square Inch
PTFE	Polytetrafluoroethylene
PVC	Poly(vinyl chloride)
RH	Relative Humidity
SEM	Scanning Electron Microscopy
SFU	Saffire Flow Unit
SIBAL	Solid Inflammatory Boundary at Low-Speed fabric
SSE	Sum Square Error
RS	Remote Sensor
UHV	Ultra-High Vacuum
2D	Two-dimensional
3D	Three-dimensional

Chapter 1: INTRODUCTION

This chapter lays out the foundation of the research. The primary work centers around the uptake of Hydrogen Chloride (HCl), produced during the smoldering of electrical insulation within spacecraft environments, by treated or untreated aluminum and other surfaces. Tracking the poisonous gas as it interacts with the surfaces prevalent in a spacecraft is necessary for crew health and safety as it can lead to better placement of sensors that ultimately trigger safety measures. The fate and lifetime of HCl within the spacecraft is dictated by its transport within the spacecraft environment and how it interacts with common surfaces within the spacecraft. This chapter will discuss the background of spacecraft fire safety, acid gas, and spacecraft materials. The state-of-the-art in acid gas and surface interactions is provided, as well as the questions that need to be answered to determine the fate of acid gas during a smoldering fire. This chapter also specifies the objectives of this dissertation, as well as an outline of the chapters to follow.

1.1 Background

A fire in a spacecraft is a catastrophic event that halts mission success and endangers the crew. The National Aeronautics and Space Administration (NASA) is interested in the prediction and prevention of fire propagation on spacecraft to reduce the risk to crew and cargo for long-duration missions. Work has been done to study the size of a fire that would require evacuation, vs. a fire that would be deemed "survivable" [1]. While a relatively small fire would be enough to cause an evacuation of a vehicle, as compared to a fire on Earth, the vast majority of fire events revolve around smoldering, particularly of electrical wire insulation. While these smoldering events are not enough to cause an evacuation, they are a danger by damaging equipment, creating smoke which reduces visibility and breathable oxygen, and creating poisonous acid gas. More information is needed about the fate of acid gases in a spacecraft environment. Learning how acid gases move around the spacecraft compartment and interact with surfaces will also aid in developing strategies for post-fire cleanup.

The International Space Station (ISS) has been continuously occupied since the year 2000 and has been without a major fire event. However, the amount of flammable material has continued to increase throughout the years [2]. Figure 1.1 shows a cluttered environment, which includes many cables that could be the cause of an electrical fire. While great care and testing is provided on items shipped to the ISS to limit the risk of a fire, some materials must be waived out of necessity, such as clothing, towels, camera mounts and cables. A common fire safety scenario in a spacecraft is an electrical fire. Table 1.1 shows previous fire events tracked on spacecrafts, while Table 1.2 reports events specifically on shuttle missions [3, 4]. A common theme in these events is the involvement of electronics and wires. Smoldering of wire insulation such as Polytetrafluoroethylene (PTFE), and Poly(vinyl chloride) (PVC) create acid gases such as Hydrogen Chloride (HCl), Hydrogen Fluoride (HF) and Hydrogen Cyanide (HCN) [5, 6]. These gases tend to stick to surfaces and participate in other reactions. It is essential to characterize the uptake of these acid gases by common interior spacecraft surfaces if the transport of acid gas through a spacecraft is to be predicted. The fire events on the space shuttle, highlighted in Table 1.2, demonstrate how most do not trigger an alarm. The experimental results in this work could help track acid gas for potential smoke detection applications, while the models developed could be used to guide designs on where to place the sensors.

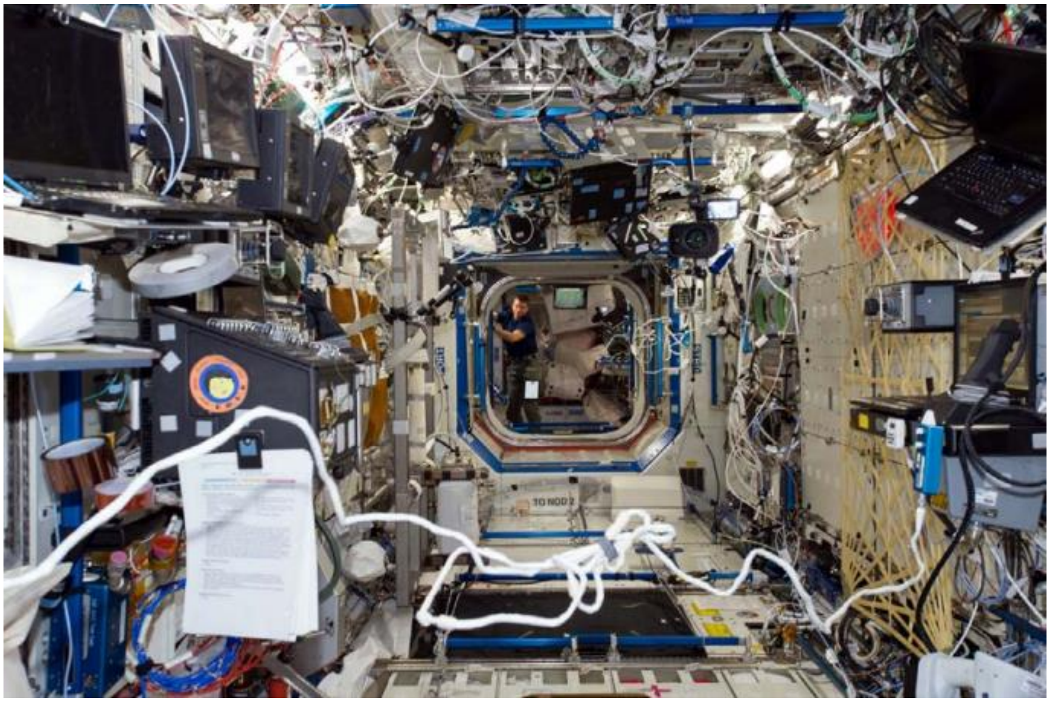

Figure 1.1: Photo of ISS highlighting cable and clutter [2].

Another common material found inside a spacecraft is Nomex, a flame-resistant synthetic polymer related to nylon. This commercially available material is used for cargo storage bags and as a fire barrier. It is particularly abundant in cargo vehicles like Northrop Grumman's (NG) Cygnus where Nomex bags are used to contain trash and other items to be removed from the ISS. While the majority of the research highlighted in this dissertation focuses on aluminum, Nomex is also included due to its importance in a spacecraft, as a comparison material, and as a proxy for a material with an effective oxide layer thickness of zero. The environment of a typical spacecraft has relative humidity (RH) levels between 40 to 60%, similar to many terrestrial habitats. This is to ensure that the crew has the conditions for optimal health and performance [7, 8] and to prohibit microbial growth [9, 10]. Given the humid environment inside the spacecraft, it is imperative to also understand how water vapor affects the interaction of HCl with aluminum surfaces.

Table 1.1: Spacecraft fire events [3].

Year	Spacecraft	Ignition source (* presumed)	Smoke/flames	Detection	Mitigation	Significant consequences
1967	Apollo 1	*wiring, flammable coolant	flames	Visual	no	Destruction of the CSM, death of three astronauts
1970	Apollo 13	*short circuit	flames	visual, instruments	no	Destruction of the CSM
1971	Salyut-I	fan mechanical failure	smoke	odor	power off	none
1977	Salyut-VI	*electrical	smoke	visual	power off	loss of scientific equipment
1978	Salyut-VI	*electrical	smoke	visual	water extinguisher	4 control panels lost: 1 to the fire, 3 to water
1983	Space Shuttle	wire fuse	smoke	odor	power off	none
1989	Space Shuttle	short circuit	smoke	visual, instruments	power off	none
1990	Space Shuttle	resistor overeating	smoke	odor	power off	none
1991	Space Shuttle	fan mechanical failure	smoke	odor	power off	contaminated atmosphere
1992	Space Shuttle	electronic failure	smoke	odor	power off	none
1994	Mir	failed cooling of the cloth filter	flames	visual	power off, quenched with jumpsuit	damaged canister
1997	Mir	*oxygen canister contamination	heavy smoke, flames	instruments	complete burn out	canister destroyed, one cable removed

Table 1.2: Shuttle fire-risk experience [4].

Mission	Date	Incident	Result	Response
STS-6	Apr. 1983	Wires fused near material processing unit; crew detected an odor	No Atmospheric contamination measured	No alarm
STS-28	Aug. 1989	Cable strain at connector to teleprinter caused insulation failure and electrical short circuit; crew detected a few embers and smoke	Smoke and particle concentration recorded	Circuit breaker did not open; no alarm
STS-35	Dec. 1990	Overheated resistor in digital display unit; crew detected an odor	No Atmospheric contamination measured	No alarm
STS-40	Jun. 1991	Refrigerator - freeze fan motor failed; crew noted an irritating odor	Atmospheric contamination identified post-flight	No alarm
STS-50	Jun. 1992	Electric capacitor in negative body pressure apparatus failed; crew detected and odor	No Atmospheric contamination measured	No alarm

Microgravity presents challenges in early-stage fire detection. Gravity induces a buoyant flow which directs any combustion products in the upward direction during terrestrial fires, allowing the most strategic location of smoke detectors to be on the ceiling. In the absence of gravity, smoke transport in a spacecraft is dominated by diffusive mixing within the cabin. Consequently, mixing of combustion products from small pyrolysis events might not trigger alarms, allowing them to grow into a more destructive fire prior to detection [11, 12].

The Saffire project aims to study large-scale flame spread in microgravity while also providing opportunities to test novel gas species sensor technology in a realistic flight configuration [13 - 14]. These experiments are expected to obtain data on the length of time to detection and detector signal level for a species release event in a spacecraft cabin. The Saffire experiments are conducted on the NG Cygnus vehicle after departing from the (ISS) during a resupply mission. The series of experiments and data downlink are performed in the three weeks between undocking from the ISS and destructive reentry in Earth's atmosphere.

The Cygnus vehicle is approximately 4 meters in length by 3 meters in diameter. During the experiment, a Far Field Device (FFD), located in the zenith section of the spacecraft, measures the temperature and product species (acid gas, CO_2, CO, water vaper, soot, etc.). Additionally, six remote sensors (RS) that measure CO_2 and temperature are also located throughout Cygnus. The air inside Cygnus was recirculated throughout the cabin by the Environmental Control and Life Support System (ECLSS), taking in air from the cabin in the zenith section near the FFD and expelling it in the nadir section close to the Saffire inlet. The crew maintained a generally prescribed free-air volume in the vehicle, consisting of interconnected channels made from trash and cargo, which transported heat, species, and smoke from the Saffire outlet to the zenith section during the campaign events. Figure 1.2 shows the Cygnus vehicle, with no trash or cargo, while Fig. 1.3 shows the loaded configuration before the experimental events.

Flame spread was the primary focus of the first three Saffire campaigns in order to compare large-scale microgravity tests to 1-g and small-scale tests [15 - 17]. Saffire IV moved the focus to the entire vehicle, incorporating gas species release events and diagnostics tools such as the FFD. These measurements will provide a deeper understanding of smoke plume transport and combustion products on the vehicle [12, 18]. In general, the Saffire payload would intake cabin air, which is the oxidizer for the solid fuel combustion, and output the heat and products to the forward port standoff. In particular, for Saffire IV, the solid fuel consisted of two samples: a cotton/fiber glass blend known as SIBAL and the transparent rigid plastic Poly(methyl methacrylate) (PMMA). The Saffire flow unit (SFU), where these fuels were housed in, was 30 cm high by 45 cm wide and 109 cm long. The experimental events in the Saffire IV test campaign

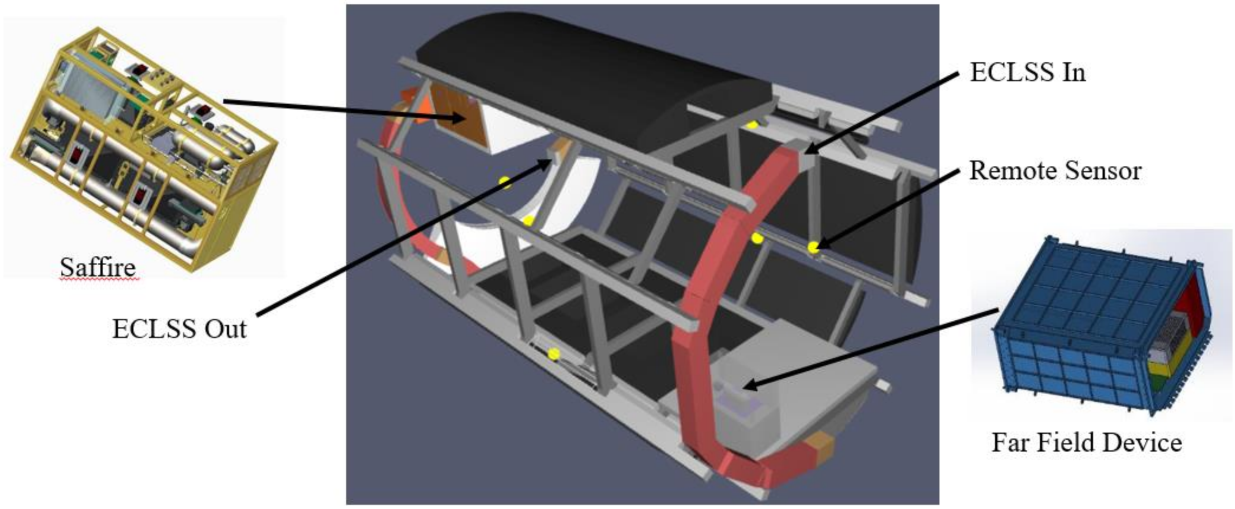

Figure 1.2: Empty Cygnus vehicle highlighting the Saffire payload, ECLSS inlet and outlet, remote sensors and FFD.

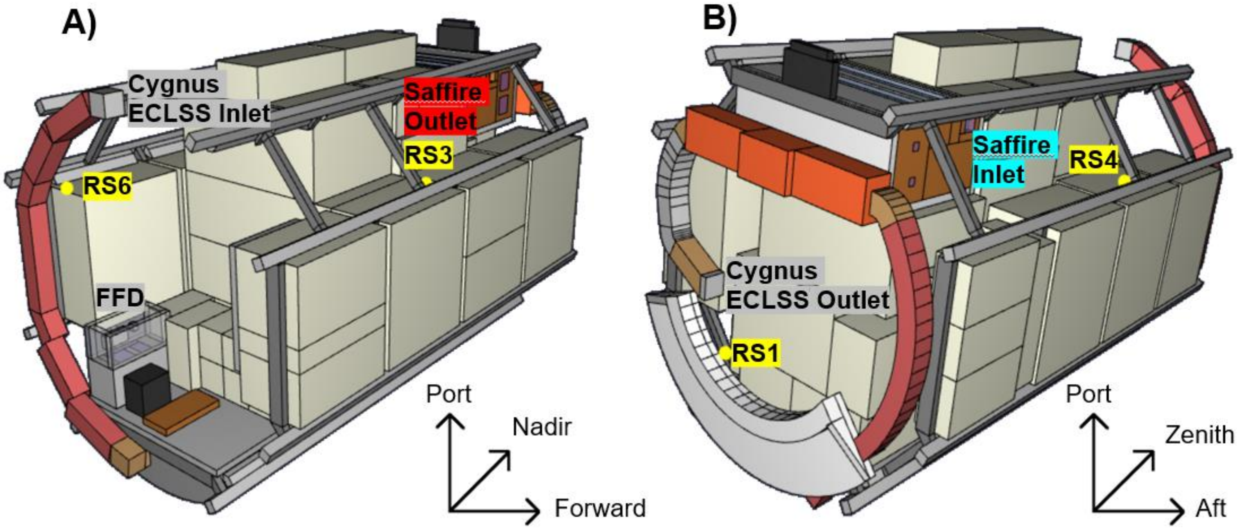

Figure 1.3: Cygnus vehicle with cargo configuration before the experimental events.

and their purpose are provided in Table 1.3. An unexpected reignition of the PMMA sample caused the cancelation of some events, but the same naming convention is retained. Since the focus of this work are the events that measured HCl in the FFD, those will be discussed in more detail.

Table 1.3: Summary of Saffire-IV Events [12].

Event Number	Description of Event	Purpose of Event
1	CO_2 Scrub	Reduce background CO_2, evaluate CO_2 scrubber performance
2	CO_2 and HCl release	Track tracer gas transport throughout cabin for vehicle volume calculation and observe HCl surface adsorption
3	Flow visualization test	Assess SFU air flow
4	Burn: 40.64 cm wide × 50 cm long SIBAL	Sample burn with concurrent HCl release
5	Burn: 40 cm wide × 18 cm long × 1 cm thick 2-sided PMMA	Sample burn, no HCl release
6	CO_2 Scrub	Evaluate CO_2 scrubber performance
9	Flow visualization test	Assess SFU air flow

Event 2 released a bottle of CO_2 and HCl into Cygnus. Each bottle was one liter with the CO_2 bottle having a concentration of 100% at a pressure of 500 pounds per square inch gauge (PSIG), which provided 1.883 mols of gas. The bottle of HCl had a concentration of 5% with an N_2 balance at 101 PSIG for a total of 0.016 mols. The released CO_2 was used to calculate a free volume in Cygnus of 18.7 m^3. This volume, along with the initial pressure of 1 atm was used to calculate an initial air mass of 21.7 kg (753.1 mols) in Cygnus. Assuming no interaction between HCl and any surface, there would be 21.2 ppm of HCl in Cygnus once all the gas diffuses throughout the vehicle. However, no HCl was detected in the FFD during this release. Following the Event 3 flow visualization test, Event 4 released another one liter, 100 PSIG cylinder of HCl, while simultaneously burning the SIBAL sample. A small response on the FFD was realized during this bottle release. Event 5 burned a PMMA sample, with no bottle release. This event produced the largest HCl response in the FFD, despite the combustion products of PMMA not including HCl.

The experiments and models conducted in this research will be used to attempt to explain these results.

1.2 State-of-the-Art on HCl Interactions

The decay of HCl from the atmosphere as it relates to terrestrial fire safety has been studied. Pyrolyzed polyvinyl chloride (PVC) was used as the source of the fire products, which include HCl [19 - 23]. Beitel et al. [19] found that unlike other fire products, such as CO_2 and CO, the HCl concentration in the room during the burning of the PVC reached a peak value and then decreased. Many typical building materials were used in the studies, such as PMMA, painted gypsum, ceiling tile and cement block. A model was developed by Galloway and Hirschler [20, 21] that considered the generation of HC1 from PVC, the transport of HC1 to the surface boundary layer, and the reaction on the surface. Parameters of the model were obtained by fitting experimental data. Tests with pure HCl as the source were compared to pyrolyzed PVC as the source and produced little difference [22]. This implies that the smoke particulates play little to no effect in the decay of HCl. It was shown that water concentration at the surface increased the capacity to uptake HCl [20, 21]. This agreed with the work of Tsia [24] who showed that HCl and nitric acid (HNO_3) adsorption increased with humidity on Teflon and Nylon filters. The model was used to predict uptake for a variety of test cell shapes and sizes, as well as changes in temperature and humidity [22]. The model was used to predict the decay of HCl in a full-scale room and corridor fire scenario [23].

One of the most abundant materials on a spacecraft is aluminum due to its strong and lightweight nature. Aluminum has a natural oxide due to its interaction with the atmosphere that protects it from corrosion. This oxide layer (i.e., alumina) is often artificially enhanced to increase its thickness [25 - 27]. Two common enhancements are chromate conversion coating (CCC), or anodization. CCC, which is commonly referred to as its commercially known name Iridite, produces a thinner oxide layer but allows the aluminum to continue to conduct electricity, while anodization provides a thicker oxide layer for more protection.

This alumina layer can be divided into an amorphous barrier layer and a porous, hydrous layer consisting of gelatinous boehmite or bayerite [28 - 30]. Water vapor from the atmosphere can affect the structure and, hence, reactivity of alumina. Schuttlefield et al. [31] has shown that alumina can uptake a monolayer of water at 50% RH, and about 2.5 monolayers at 80% RH. This relationship between water uptake and humidity is approximately linear. Al-Abadleh and Grassian [32] have shown that for alpha alumina, a monolayer of water first forms at 17% RH. Volpe [33] found similar results on other aluminum alloy surfaces. Hunter and Fowle [34] studied natural and thermally formed oxide films, determining that the outer portion, which is formed by components of the environment like moisture, can pass current freely in either direction, similar to the porous portion of anodically formed oxide films. Peri and Hannan [35] described water adsorption on alumina as non-dissociative chemisorption through very strong hydrogen bonds between surface oxide groups and water. The uptake of water through hydrogen bonding can be found in other oxides, such as calcite [36]. It was also found that below 55% RH, an ordered ice-like 2D island structure seems to prevail until a monolayer at a RH of 55% is formed. Beyond this value, multilayer adsorption of H_2O occurs with a 3D-structure resembling liquid water. McCafferty [37] found that a natural or enhanced aluminum oxide layer will form an aluminum hydroxyl layer by contact with H_2O in its environment. This layer is porous and contains many active sites for HCl to adsorb [38 - 40].

Anodized or anodic aluminum form reproducible circular pores and are often modeled as a hexagonal array of circular pores [41 - 43]. Additionally, there are numerous studies that produce anodized oxide pores for various purposes (humidity sensors, pressure sensitive paint, nanoscale research) [44 - 47]. Pictures and schematics of how pores are ideally ordered are shown in Figs. 1.4 - 1.6. There are many ways to tune the pore size and structure, from the type of acid bath, its concentration, voltage strength and time. Using the voltage and preparation time of these studies, the structure of the anodized aluminum used in this study is inferred. These findings will be used to guide this work.

The uptake of adsorbates by porous media are usually studied in packed bed or pebble bed reactors. Kameda et al. [48] was able to remove HCl generated from industrial waste incinerators in a batch reactor by using magnesium–aluminum. They showed that more is removed with the addition of water vapor, and at lower temperatures. In a similar reactor, they also showed the magnesium – aluminum removed chloride from various solutions [49]. Cao et al. [50] synthesized a calcium−magnesium−aluminum sorbent for removal of HCl from flue gas due to municipal solid waste in a fixed bed reactor. A summary of typical adsorbents used in reactors, and analysis methods to determine their performance, such as breakthrough curves, is given by Paereli [51].

Gas-solid interactions are commonly found in the study of catalysts. Alumina is an important oxide material used as the support of numerous catalytic active phases [52]. Modelers of catalytic reactions use a finite active surface site density, and the reaction slows as the sites fill (get deactivated/poisoned), such as in Deutschmann’s analysis of methane combustion on platinum

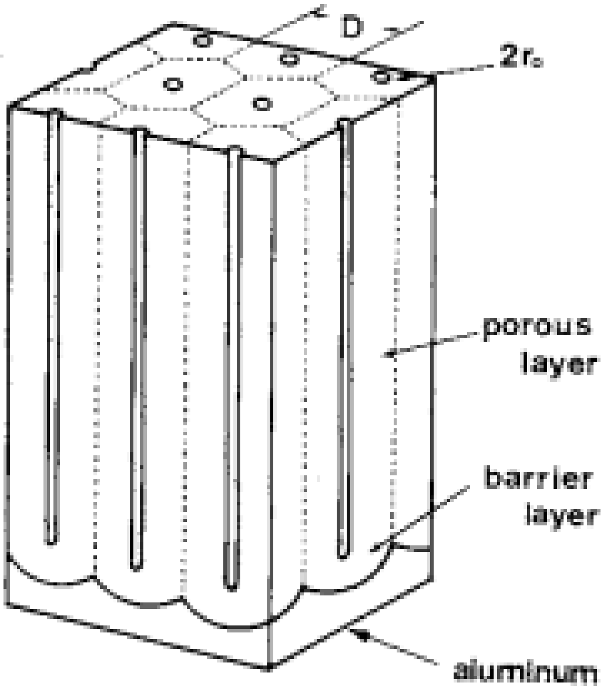

Figure 1.4: Structure of anodic aluminum oxide. Dimensions of pore ($2r_o$) and cell D are indicated [41].

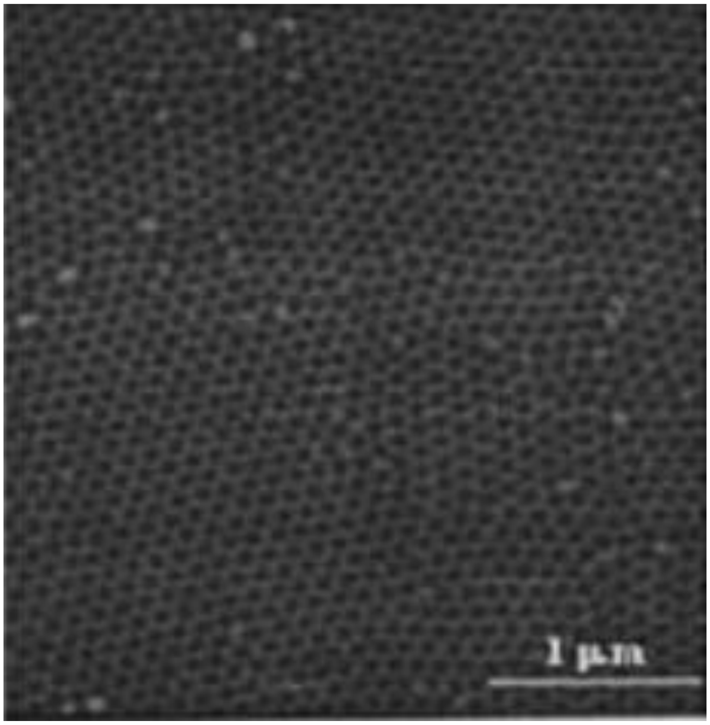

Figure 1.5: SEM images of anodic alumina films anodized at 40 V in 3% H2C2O4 at 15 ℃ three times: for 10 min, then 11.5 h and then 3 min [42].

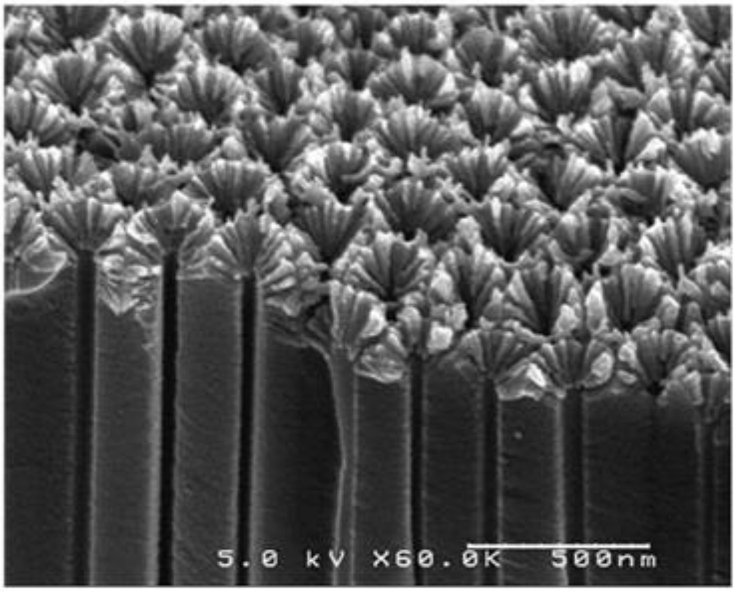

Figure 1.6: Scanning electron micrograph of anodic alumina film prepared using oxalic solution 3% (w/w), at 10 °C under 72 Volts, showing cross-sectional view with open pores on top surface after removing caps and aluminum substrate by electrochemical treatment [43].

catalysts [53]. A surface coverage dependent rate expression was used to describe adsorption, desorption, and surface reactions on the platinum surface. Coltrin et al. [54] developed a kinetic formalism, Surface-CHEMKIN for treating heterogeneous reactions at gas-surface interfaces. The rate of progress of the surface reactions follows the law of mass action, and the rate has terms that vary as a function of open surface sites.

Several studies have detailed the reaction between HCl and alumina. Cofer et al. [55] has found that the reaction of gaseous HCl and H_2O with alumina from space shuttle exhaust produce water-soluble aluminum chlorides and oxychlorides in a laboratory environment. Other researchers observed those same reactions, with aluminum chloride being prevalent in high temperature (above 200 °C) systems and aluminum oxychloride in lower temperature (room temperature) systems [56, 57]. HCl has been shown to adsorb and react with other metal oxides and hydroxides. Bausach et al. [58] showed that the reaction between HCl and $Ca(OH)_2$ at low temperature most likely forms Ca(OH)Cl, which was found to be a stable product in contact with the atmosphere. Peterson and Rossin [59] used Zr(OH) to remove HCl, Cl_2 and $COCl_2$ from air streams. They showed HCl being able to react directly with Zr(OH) while Cl_2 and $COCl_2$ must first be hydrolyzed.

The capacity of alumina to uptake HCl has been previously measured. Bailey and Wightman [39, 60] determined the capacity of alumina to uptake HCl to be 0.224 grams of HCl per gram alumina in a study of solid rocket exhaust. It is difficult to compare and infer uptake capacity and rates from the various studies, as the aluminum adsorbent is ground into fine pellets, pebbles, or particles of differing coarseness. While using methods, such as Brunauer–Emmett–Teller (BET) [51] can determine the surface area of these ground adsorbents, this surface area is much higher than the superficial or geometric surface area that would be known in engineering materials and would be useful in large-scale modeling efforts.

Although HCl is a simple molecule, alumina is more complex, being heterogeneous with several bonding sites and interaction modes, making reactions not easily quantifiable [48]. The aforementioned studies investigated either the reaction of HCl with pure alumina, or outgassed oxide materials at high temperatures to remove any water vapor or impurities. [55 - 60]. However, the interaction of HCl with real engineering materials, such as the aluminum used in the structural support of spacecraft vehicles at ambient temperature and atmosphere have not been investigated. The interactions of HCl with aluminum of specific treatments found in a space vehicle must be measured if they are to be used to guide development of models to predict the uptake of HCl by surfaces in a spacecraft.

Typical techniques to directly measure uptake of gas onto surfaces, or adsorption in general, is to use a gravimetric method, such as a quartz crystal microbalance [31, 61]. These techniques directly measure the mass increase of a sample per unit area to determine in real time the rate of uptake by the gas. These techniques often employ very precise equipment that needs to be under ultra-high vacuum (UHV) conditions to work properly or include delicate and expensive instrumentation that could be damaged by acid gases, especially at high humidity levels. It is desirable to design an alternative solution to measure uptake with robust parts that can be easily replaced if damaged, as well as work under atmospheric pressure. Another typical technique to measure uptake includes volumetric methods, where changes in the atmosphere, such as partial pressure of the adsorbed gas, are measured. While not directly measuring the interaction of the sample surface and gas, it can reliably be used (in conjunction with modeling) to connect concentration of the adsorbate measured in the atmosphere to the rate of uptake by the adsorbent.

1.3 Objectives

The overall goal of this study is to provide a better understanding of the interaction between HCl and alumina and to develop engineering models that can be used to predict the fate of HCl in spacecraft environments. With the previously discussed difficulties and gaps in knowledge in mind, the specific objectives of this research are as follows:

- Measure the capacity of the three common treatments of aluminum found in a spacecraft (untreated, Chromate Conversion Coated, anodized), and Nomex to uptake HCl in a dry environment to eliminate the effect of moisture.
- Develop physics-based models that can predict the rate of uptake of HCl onto these surfaces.
- Investigating the effect of moisture (humidity) on uptake capacity and rate.

- Test acid gas-surface interactions at the scale and conditions realized in full-scale microgravity experiments.
- Use validated models at the laboratory-scale to interpret the results of large-scale microgravity experiments and vehicle fire safety design in general.

The following tasks were undertaken to accomplish the aforementioned objectives:

-A reactor for flowing acid gas and inserting samples was designed and constructed.

-The test reactor was modeled in order to determine the rate of uptake of samples.

-The reactor model was validated against different flow rates, concentrations, and sample surface area.

-A bubbler was integrated into the reactor flow path to control the humidity of the flow.

-X-Ray Photoelectron Spectroscopy was used to determine the structure and chemical composition of the oxide layer and products from interaction with HCl.

-A model was developed to account for transport of HCl into the oxide layer

-Acid gas was flowed through a large-scale facility constructed with walls of the different sample material.

-The kinetic parameters developed in this work were used in a model of the large-scale facility to predict the large-scale tests.

1.4 Outline of Dissertation

The experimental methods and apparatus used to determine the rate and uptake capacity of HCl onto aluminum surfaces is discussed in Chapter 2, in addition to some experimental results.

This experimental methodology includes design and construction of a small-scale reactor for flowing HCl over the surfaces of interest, XPS for determining depth of chlorine in the saturated samples, a thermal vacuum system for controlling water in the oxide layer of aluminum samples, and a large-scale duct for flowing acid gas on the scale of full-scale vehicle microgravity tests.

In Chapter 3, a model using commercial computational fluid dynamics (CFD) software, which predicts the HCl update in the reactor-scale experiments under dry conditions, is set up and validated under different operating conditions. Comparison between the 3D model and less computationally demanding 2D axisymmetric model is discussed. A sensitivity and uncertainty analysis is presented.

Chapter 4 details the development of a model of the pores within the anodized aluminum's oxide layer. In this model, the HCl diffuses through the pores, and reacts with the aluminum oxide pore wall to create an aluminum chloride product layer. The sample is saturated when the product layer becomes too large for HCl to reach the wall and react. This pore-scale model is then coupled with the reactor-scale model to create the so-called *multiscale* model.

The effect of moisture on the uptake of HCl on aluminum surfaces is examined in Chapter 5. Experiments, where HCl uptake is measured under moist conditions, as well as modeling strategies are discussed. Hysteresis tests are completed to determine the repeatability of the same sample after it had been saturated or subjected to HCl and water vapor, and these results are also presented in Chapter 5.

The large-scale microgravity experiment, Saffire, as it relates to this research and to spacecraft fire safety in general, is discussed in Chapter 6. The large-scale ground facility was used to flow acid gases, at the scale and operational conditions found in the Saffire experiments. A numerical model of the duct is used to predict these experimental results and test the reaction mechanisms developed during this research. This model is expanded to include a volume similar to the zenith hatch in the Cygnus vehicle to better interpret the acid gas results in Saffire.

Chapter 7 summarizes the key results from the research in addition to outlining future work needed to better determine the fate of acid gas in a spacecraft.

Chapter 2: EXPERIMENTAL METHODS AND RESULTS

The methods used to collect data are described in this chapter. Some sample results are also presented. The primary experimental setup is a reactor used to determine the uptake of HCl over surfaces of interest, most notably aluminum. Secondary test methods include X-Ray Photoelectron Spectroscopy (XPS) of the aluminum sample surfaces to determine the chemical species on the surface of the samples before and after testing, a thermal vacuum used to measure the water saturation of samples and an attempt to test samples at lower water saturation. A large-scale flow facility was also constructed to test the reaction mechanisms and models developed using the data collected from the reactor, as well as to interpret and compare the results of the Saffire microgravity tests.

2.1 Reactor Apparatus

An experiment was designed to determine the uptake of HCl on aluminum with three different surface treatments (Chromate Conversion Coating (CCC), anodized and untreated stock). A test cell (reactor) made of cast acrylic was constructed and an air stream with a known HCl concentration flowed through it. In this work, HCl represents the other acid gases since it was deemed less hazardous from a safety standpoint compared to HF or HCN and is assumed to act similarly. Acrylic is not known to react with HCl. The variation of the same test cell was made from Polytetrafluoroethylene (PTFE) since HF has the potential to react with acrylic, and as part of future studies, there is a desire to test with HF. The PTFE and cast acrylic test cells both performed the same in terms of minimal HCl saturation and time to saturation during dry acid gas tests, but far more HCl was adsorbed on the PTFE during humid HCl flow tests as compared to cast acrylic. Since no HF tests were performed in this research, the cast acrylic test cell was chosen. A picture of the PTFE test cell with the CCC sample is displayed in Fig. 2.1, and the cast acrylic test cell with an anodized aluminum sample is shown in Fig. 2.2.

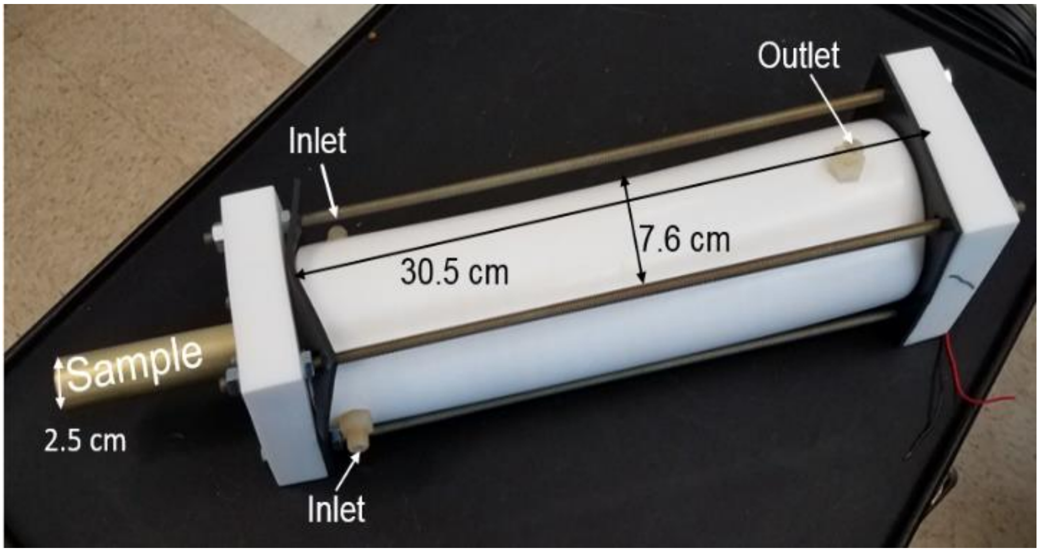

Figure 2.1: PTFE test reactor with gold CCC sample.

Figure 2.2: Cast acrylic test reactor with anodized aluminum sample. The same dimensions as the PTFE reactor were used in the cast acrylic reactor.

The HCl was supplied from a cylinder containing nearly 50 parts per million (ppm) HCl balanced by dry air. Another bottle of pure dry air was available to dilute the stream to allow for inlet concentrations less than the HCl bottle concentration. The electrochemical HCl sensors (ATI F12/D), which were used to measure the concentration of HCl at the inlet and outlet, have a range up to 50 ppm and a resolution of 0.1 ppm. The mass flow controllers used (MKS 1179A) enable gas flow up to 5.0 liters per minute (lpm) with a resolution of 0.05 lpm. The accuracy of the mass flow controller is 1.0% of this full-scale value. There is approximately 7.2 meters of stainless-steel tube between the mass flow controller and the test cell. On most dry days, it takes between 5 and 20 minutes to saturate these stainless-steel lines and test cell with HCl to prepare for a test. This varies since the system is exposed to the outside environment through the ventilation system and can vary depending on the previous tests completed that day.

Figure 2.3 shows a schematic of the apparatus. The test began by flowing HCl through the empty test cell until the inlet and outlet HCl sensors reach a steady state. After inlet and outlet HCl sensors showed stable, nearly equal values (equilibrium), the aluminum rod or sample was inserted. The outlet sensor concentration dropped rapidly upon the insertion of the aluminum rod and gradually returned to its initial value. The experiment ended when the outlet sensor recovered to its initial value.

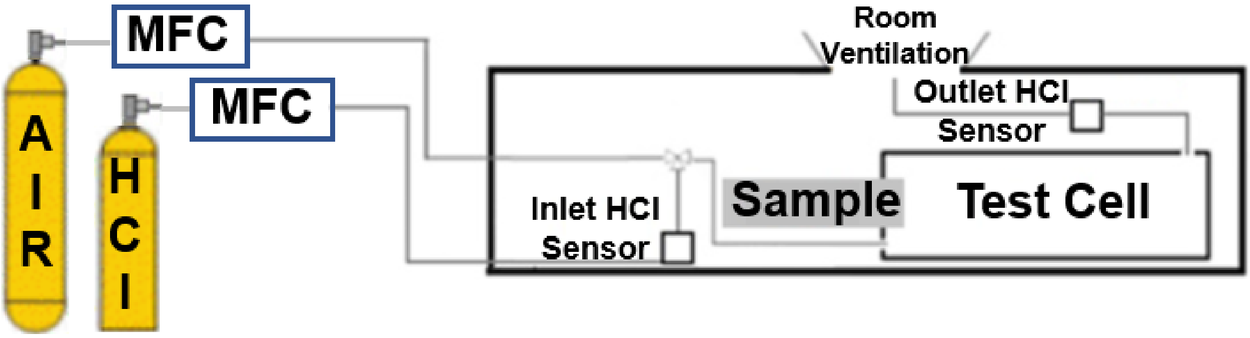

Figure 2.3: Schematic of laboratory setup. The sample is pushed into the test cell after inlet and outlet HCl sensors showed equilibrium.

Figure 2.4 shows a typical outlet sensor curve realized from these tests after the test cell and supply lines are passivated and stable, making the test piece the only surface newly exposed to HCl. In particular, Fig. 2.4 shows the outlet sensor data during an anodized aluminum test after the rod has been inserted, showing the outlet sensor drop for approximately 5 minutes, before recovering to its initial value over the next 60 minutes. This increase in the outlet sensor is due to the aluminum becoming saturated with HCl, indicating there is a finite capacity to uptake HCl by the sample. The inlet HCl sensor does creep up 0.3 ppm on average from the start to the end of the test due to the supply lines from the bottle becoming slightly more saturated over time. Since this increase is small relative to the measured levels, it is assumed the inlet concentration remains constant throughout the test.

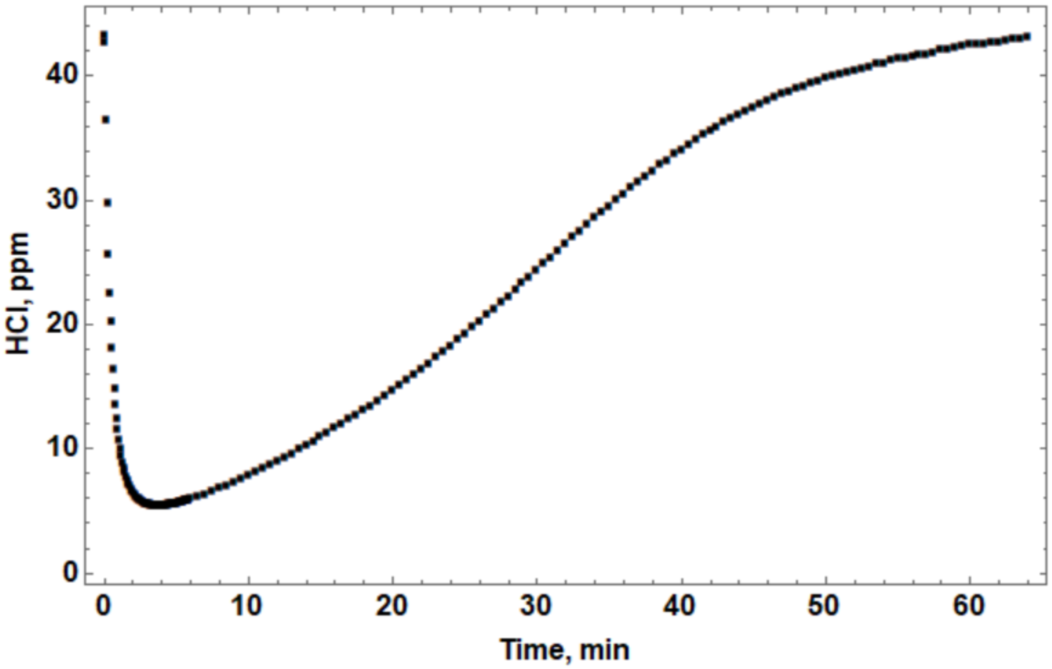

Figure 2.4: Outlet HCl sensor during an anodized aluminum test.

Another sample that was tested is Nomex, which is a fire-retardant cloth usually used to wrap trash and cargo in a spacecraft. The Nomex sample is displayed in Fig. 2.5 along with the insertion mechanism.

6061-T6 aluminum rods of 2.5-cm diameter and 30.5-cm length were used as samples. The rods were treated by chromate conversion coating (CCC) using MIL-DTL-5541F Type I, anodized by MIL-A-8625F TYP II Class 1, or left with a native oxide layer. The samples were kept in a humidity-controlled container which kept the samples at 50% relative humidity (RH) since it was determined that water vapor affects the amount of HCl uptake, and a typical spacecraft environment is between 40 and 60% RH [7 - 10]. Attempts were made to control the humidity of the sample throughout the entire testing process, specifically after the sample is taken out from humid storage and loaded outside of the test cell and before the sample is inserted into the test cell while the supply lines and test cell are being saturated. During this time, the sample is in the same environment as the lab in general, which is uncontrolled in terms of humidity. However, testing

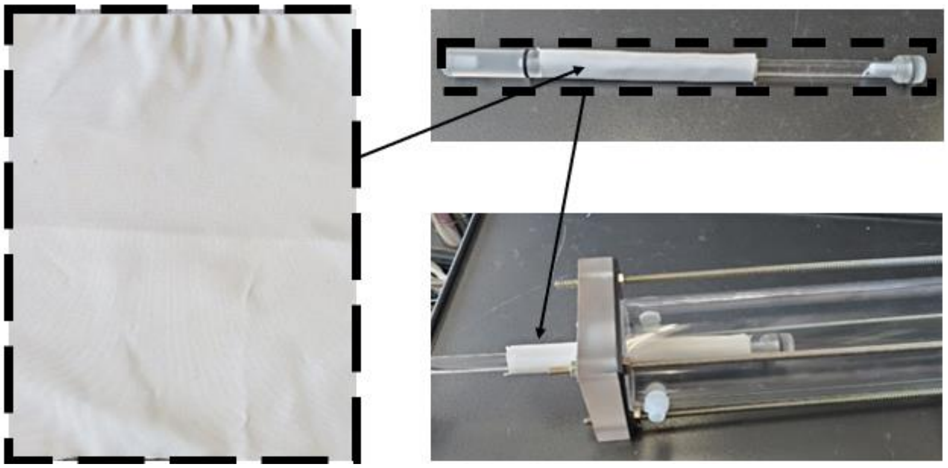

Figure 2.5: Nomex sample with cast acrylic inserter.

was done that deemed no significant changes in water saturation would take place within an hour. These tests are discussed in a subsequent section.

A bubbler (Electromantle EM1000) was added in the path of the air flow to add water vapor to the gas stream to determine the effect of humidity on the uptake of HCl. Figure 2.6 shows this setup. The bubbler was also used to flow humid air over a saturated sample post-test in order to study the effect of water vapor on cleaning of the aluminum after the test. The amount of humidity was controlled by varying the flow controllers of the air and HCl cylinders. The RH level was confirmed with a separate sensor before the test began with air flow, (Lascar EL-USB-2) with a resolution of 0.5% RH and an accuracy of 2.25% of the value measured. In most cases, the RH in the chamber was the average of the dry air flow and wet air flow. For example, if the test cell received 1000 ccm of dry air flow directly from the cylinder, and 1000 ccm of flow going through the bubbler, the RH would be 50% (11,540 ppm of water vapor at 20 °C).

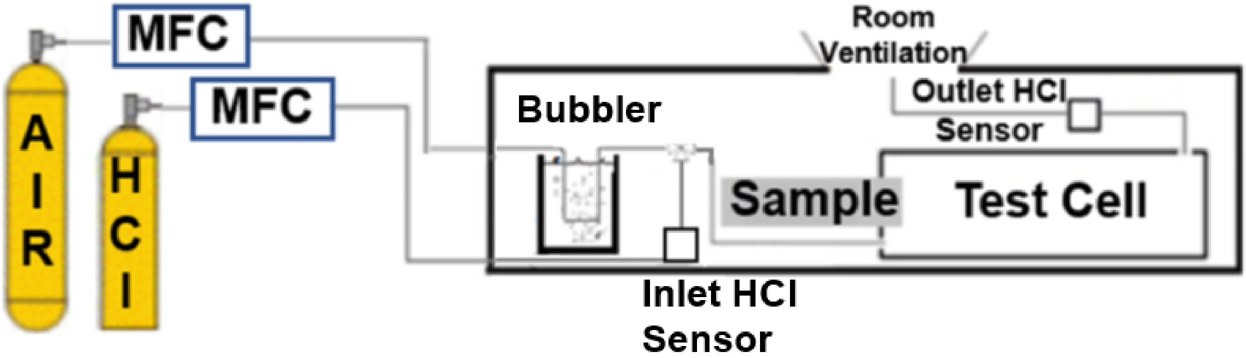

Figure 2.6: Laboratory setup with humidifier. Air flows through the humidifier and mixes with HCl to create humid air and HCl mixture. Mass flow controllers (MFC) determine how much humidity is in the mixture.

2.2 Sample Results

As discussed in the previous section, the outlet HCl concentration was measured as a function of time to determine the uptake of HCl on the surface. The baseline case considered was that of 43.1 ppm inlet concentration of HCl, 1.0 lpm flow rate, and a rod length of 20.3 cm, with a room temperature of 20 °C and 50% RH. These flow conditions were chosen to align with the large-scale tests in the Saffire microgravity experiments. Figure 2.7 shows the three-time histories of the outlet sensor under baseline conditions for each type of aluminum surface. Figure 2.8 shows the Nomex sample, giving a similar response. The shape of each curve is similar—the outlet HCl concentration drops sharply within the first three minutes and then increases gradually to the same value as the inlet. Initially, the entire reactor has a uniform concentration of HCl. The sharp drop in the first few minutes occurs when the sample is inserted and HCl encounters the fresh aluminum

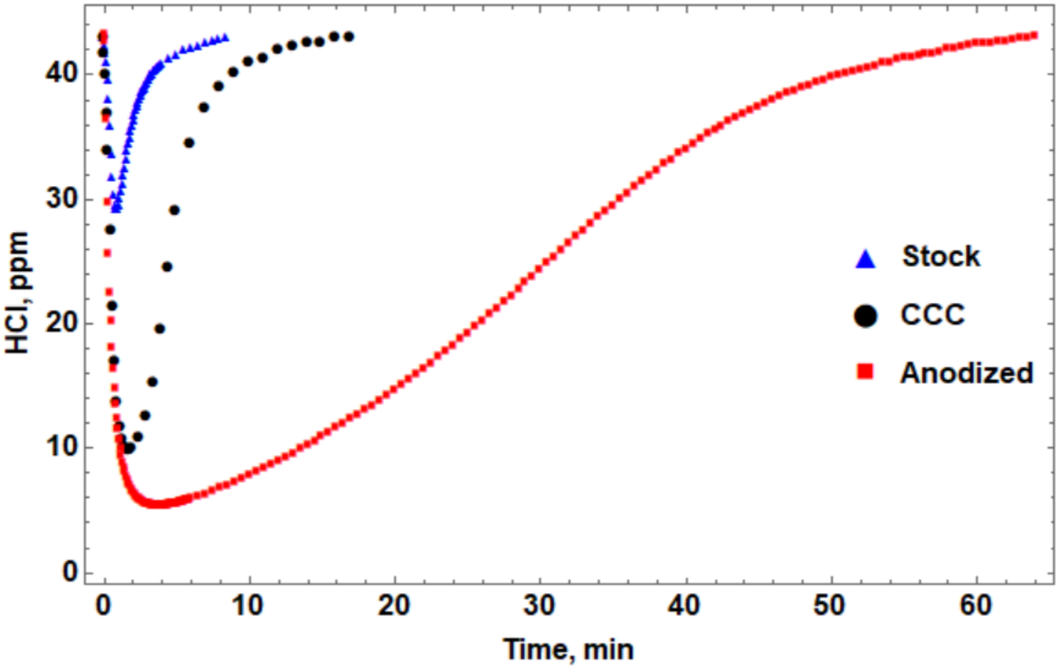

Figure 2.7: Time histories of HCl outlet sensor for the three aluminum surface treatments.

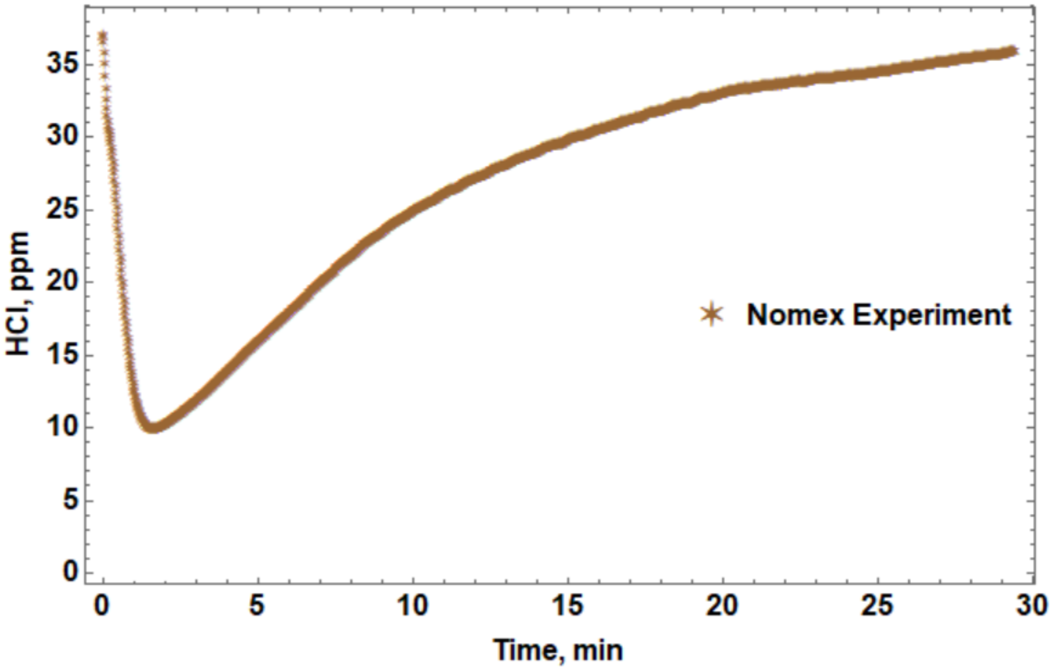

Figure 2.8: Time history of HCl outlet sensor for the Nomex sample.

surface. At this point, the surface is “clean” and none of the active sites are occupied. As time progresses, these sites are occupied by HCl, and the overall adsorption rate decreases. This causes the outlet concentration to rise slowly again until the surface sites are completely occupied, and no adsorption is possible anymore. At this point, the outlet concentration becomes equal to the inlet concentration again. For the stock samples, this required approximately 9 minutes, while it took nearly 20 minutes and 60 minutes for the CCC and anodized samples, respectively, suggesting that there are more active sites in these samples. The experimental data were integrated over time to determine the net uptake of HCl expressed as site density. Specifically, area under the curve is integrated using the trapezoid rule (representing mols of HCl that makes it to the outlet of the reactor). This value is subtracted from the mols of HCl that enter the reactor. This is shown in equation Eq. 2.1, where ρ_{site} is the site density in μmol/m^2, M_{HCl} is the molar mass of HCl, $\dot{m}$ is the mass flow rate in kg/s, A is the surface area of the sample in m^2, Y is the mass fraction of HCl in

$$\rho_{site} = \frac{\dot{m}}{A} M_{HCl}(Y_{in}t - \int Y_{out}) \tag{2.1}$$

air, and t is the time of the entire experiment from sample insertion to saturation. For the baseline case, the average uptake of HCl and standard deviation, based on 3 test runs, is 80.1 ± 4.5 μmol/m^2 for stock aluminum, 407 ± 20 μmol/m^2 for CCC, 2901 ± 230 μmol/m^2 for anodized, and 814 ± 32 μmol/m^2 for Nomex. These numbers were input into the model as the surface site density in keeping with the law of mass conservation. It is to be noted that these are not actual site densities, but site densities based on the surface area of the sample. They are useful for modeling purposes as we shall see in Ch. 3.

In order to establish repeatability of the experiments, three different CCC samples were tested under the baseline condition. Minor variability was noticed as shown in Fig. 2.9. The first data set was ultimately chosen to be the data set to be used for calibration of the model. Table 2.1 lists the total HCl uptake for the three CCC baseline cases, as well as cases run at different operating conditions for the CCC samples that will be presented in Ch. 3.

Elam et al. [62] studied HCl adsorption on a single crystal of alumina. They found that the sticking coefficient decreased nearly exponentially with surface coverage from about 10^{-3} to 10^{-11}. They were able to determine the saturation coverage of $1.0\text{x}10^{14}$ molecules/cm^2. This is significantly less uptake than the aluminum surfaces used in this study ($4.8\text{x}10^{15}$ molecules/cm^2 for stock, $2.5\text{x}10^{16}$ molecules/cm^2 for CCC and $1.7\text{x}10^{17}$ molecules/cm^2 for anodized). This could be due to the difference in surface area between the pure alumina crystal and oxide-coated aluminum surfaces or due to water vapor uptake by the aluminum surface.

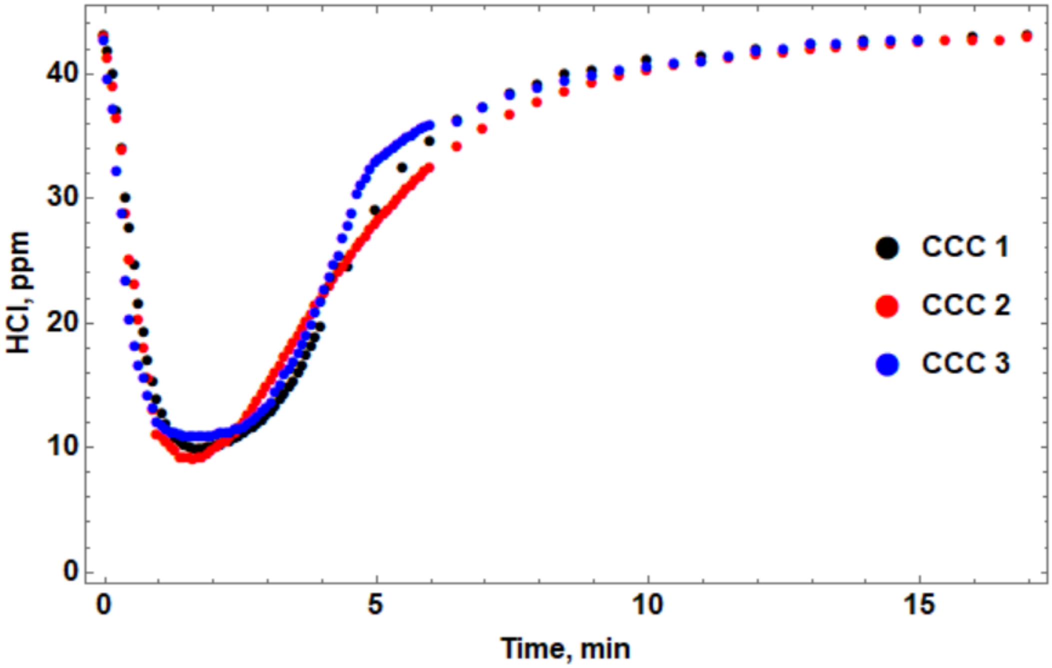

Figure 2.9: Time history of outlet HCl concentration for the three tests with CCC samples under baseline conditions.

Table 2.1:Uptake of HCl from CCC aluminum samples.

Test	Uptake (μmol/m^2)
Baseline CCC Test 1	409
Baseline CCC Test 2	426
Baseline CCC Test 3	387
2L/min	403
10.2 cm Length	428
Half Baseline Inlet Concentration	392

2.3 X-Ray Photoelectron Spectroscopy (XPS)

XPS, also referred to as Electron Spectroscopy for Chemical Analysis (ESCA), can determine the chemical elements that exist in a material, particularly on the surface. The technique uses the photoelectric effect to determine elemental composition, chemical state, and electronic structure of a solid sample. This phenomenon is observed when a material absorbs electromagnetic radiation, and then releases electrically charged particles. In the case of XPS, the radiant energy is in the form of X-rays, and the released particles are electrons. The higher frequency of X-rays compared to other radiation, can release electrons near the atomic nucleus, where they are tightly bound. The ejection of the inner electron forces a higher-energy outer electron to drop down and fill the vacancy. The excess energy results in the emission of one or more additional electrons (secondary electrons) from the atom, which is called the Auger effect. These secondary electrons are measured by a detector, also known as a spectrometer, which provides a graph of the intensity in counts per second against the binding energy, usually in eV. Figure 2.10 gives a schematic of the XPS process.

The sample is exposed to photons having energy $\bar{h}\omega$, where h is Planck's constant and ω is the frequency, which is inversely proportional to wavelength. The energy from the X-ray source is high enough to eject inner-shell electrons. The process is represented by:

$$A + \bar{h}\omega \rightarrow A^{+} + e^{-} \tag{2.2}$$

where A is an atom, A^{+} is a positively charged ion and e^{-} is the photoelectron. The kinetic energy, E_{kin}, of the photoelectron can be expressed in as:

$$E_{kin} = \bar{h}\omega - E_{b} - W \tag{2.3}$$

where E_b is the binding energy of the electron and W is the work function. A concentric hemispherical analyzer (CHA) is commonly used to detect the kinetic energy. It acts as a band pass filter, opening a window for only a small energy band around a given energy, which increases signal-to-noise ratio and sensitivity.

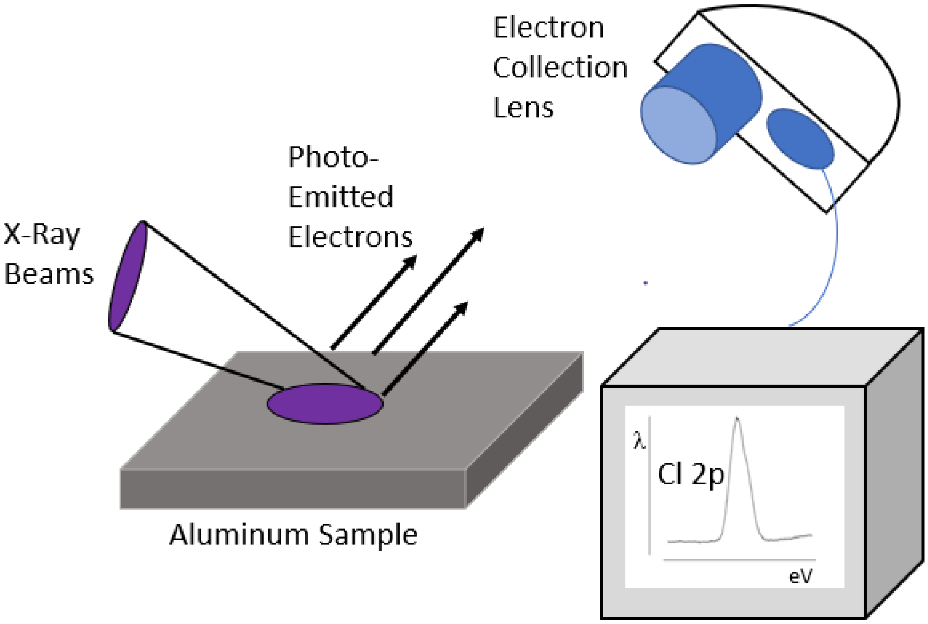

Figure 2.10: Schematic of XPS process. X-rays release photoelectrons from a solid sample and are collected by a spectrometer and read as a spectrum in the form of intensity vs. binding energy.

The surface of a sample is steadily reacting with the ambient atmosphere. This makes the composition of the surface hard to distinguish with consistency. For this reason, XPS is usually performed in a vacuum chamber. Ultra-high vacuum (UHV) is needed, which is defined as a pressure between 10^{-8} to 10^{-11} Torr [63]. An ion gun is used for surface cleaning and for sputter depth profiling.

The XPS apparatus used in this study was the PHI Versa 5000. It uses an argon ion gun that provides between 5 eV to 5 keV for high resolution sputter depth profiling. An Al K_{α} X-ray source is utilized that can be computer controlled from less than 10 μm diameter to 100 μm diameter for increased sensitivity. The vacuum system used provides a pressure under $3x10^{-10}$ Torr.

Figure 2.11 shows an example of the data collected using XPS in this test campaign. In this case, the results are from a sample of CCC aluminum that had been fully saturated with HCl. The primary element investigated by XPS in this work is chlorine, most likely from the formation of aluminum chloride by reaction of HCl with alumina. XPS detects atomic chlorine, usually in the Cl 2p electron configuration, with binding energy detected at around 200 eV [64, 65]. The location of the spike on the x-axis refers to a specific chemical; in this case, chlorine. The intensity on the y-axis is directly proportional to the amount of that element that is present. These spectra have been collected at various depths, shown on the z-axis. These data, along with spectra of other elements, (such as aluminum and oxygen) are used to give the elemental percent as a function of depth in the oxide layer.

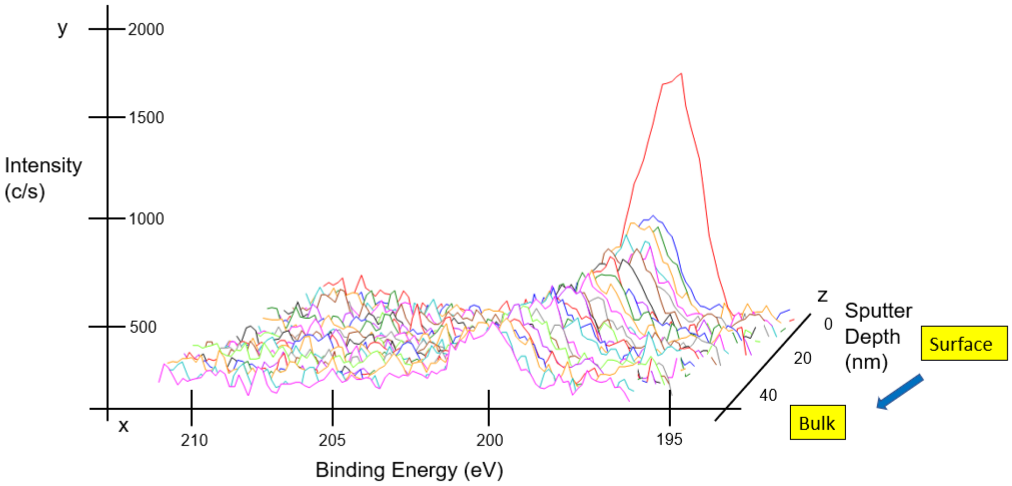

Figure 2.11: Representative data from XPS (CCC aluminum fully saturated with HCl).

2.4 Humidity Control Equipment

Since water vapor from the atmosphere was deemed to play a factor in HCl uptake [24, 30], the samples were kept in a controlled environment. While the laboratory was controlled for temperature (~20 °C), it was uncontrolled for humidity, often being similar to the outside atmosphere. Figure 2.12 shows a schematic of the sample storage container. A plexiglass container previously used to store desiccant was converted into a sample storage container. An Inkbird temperature and humidity Controller (ITC-608T) turned on a Satechi ultrasonic humidifier, which was placed in distilled water, when the RH fell below 49.0%. The Inkbird Controller then powers the Pro Breeze Dehumidifier (Model XROW 600A) when the RH gets above 51%. The Inkbird controller comes with a humidity sensor that has an accuracy of 0.1% RH. A mini fan is used to promote a well-mixed environment.

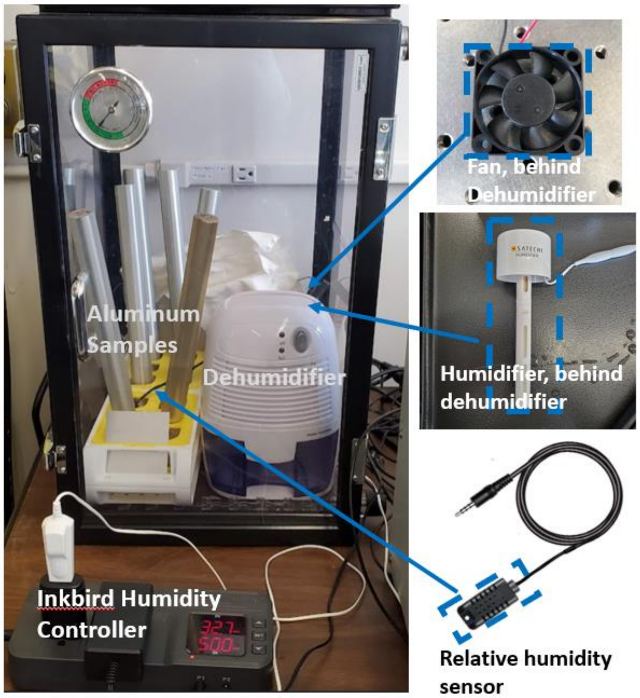

Figure 2.12: Sample storage container to control for humidity. An Inkbird controller triggered a humidifier or dehumidifier to keep the RH in the chamber ~ 50%. A fan was used to promote a well-mixed environment.

It is known that the oxide layer in the various samples retains the water vapor in the air [28-32]. A thermal vacuum system was used to determine how much water was in the oxide layer and potentially determine the impact of HCl uptake at different water saturation levels. Figure 2.13 presents a schematic of this apparatus. A General Electric Motor A-C Motor (1725 RPM, 1/3

Horsepower) powered vacuum for a VWR-I450 thermal chamber that can produce a temperature of 340 °C. The system was able to produce a vacuum with a gauge pressure of -755 mmHg gauge. Flat aluminum samples (7.6x7.6 cm area by .064 cm thick) were weighed before and after exposure to the thermal vacuum using a Mettler Toledo MS105 Semi-Micro Balance.

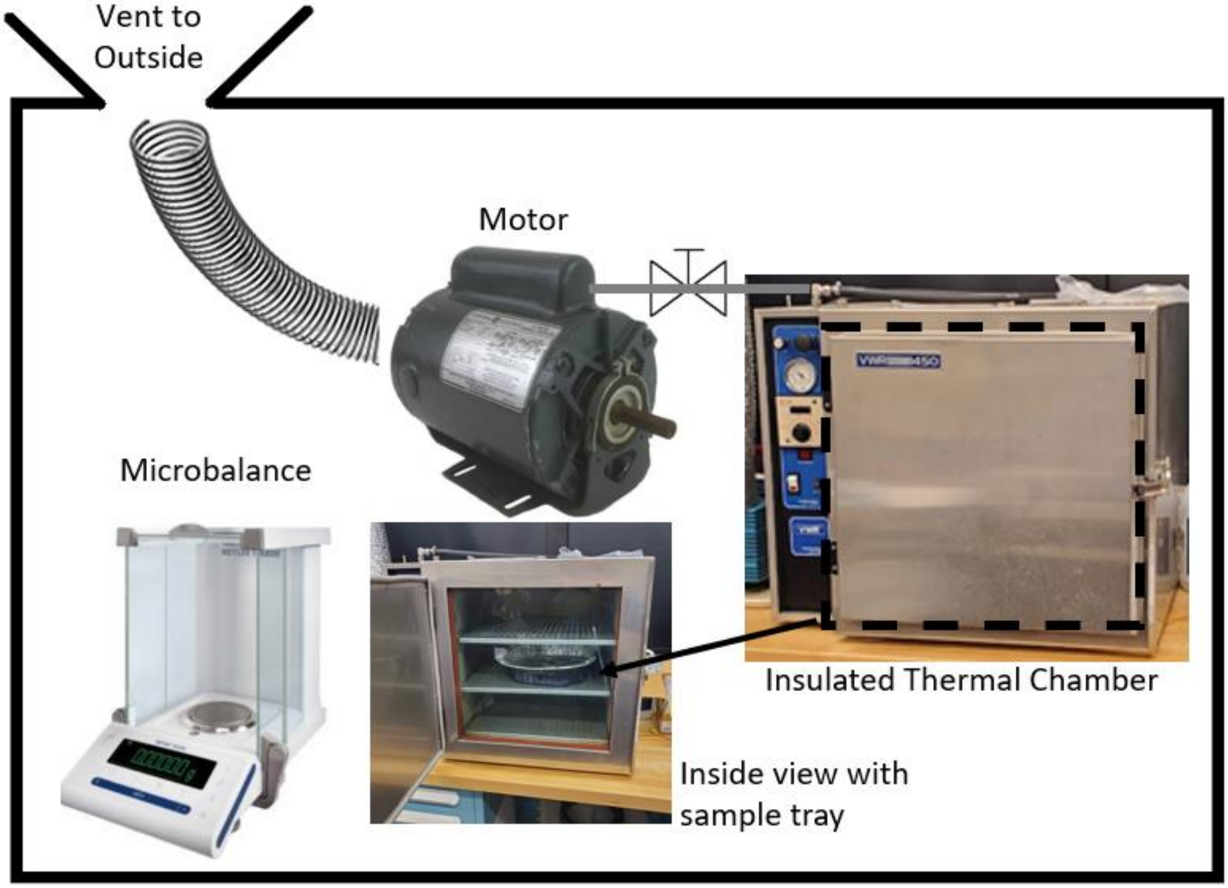

Figure 2.13: Schematic of thermal vacuum system. A motor decreases the pressure inside a thermally insulated chamber for the purposes of desorbing water vapor from aluminum samples.

2.5 Large-Scale Acid Gas Flow Facility

A facility was designed and constructed to mimic the environment that would be expected in a spacecraft. This provides a test bed to compare acid gas results performed in microgravity with

1-g results, aid in the design of future 0-g tests, and to investigate results provided in 0-g. The entire apparatus, besides the 1% HCl that was in its own containment, is encompassed in a 6.25 x 4.5-meter area plexiglass box. The flow conditions were chosen to align with what would be expected in a spacecraft. More specifically, they were chosen to align with the Cygnus vehicle size and flow, where the Saffire experiments take place.

In this study, a mixture of air and HCl moves through a test duct of 0.45 x 0.50 meters in area by 3.65 m in length where the walls are made of the sample material. Baseline volume flow rate for the air in the duct was 2,800 lpm, which produced an average speed of approximately 20 cm/s in the duct. A mass flow controller sent acid gas to a static mixer at a rate up to 20 lpm, which gives an acid gas concentration of 30 ppm. The walls of the test duct were first constructed out of the same untreated aluminum as the reactor model. The walls were then removed, and anodized aluminum was used for additional tests.

A centrifugal fan (Ebmpapst G1G146-BA07-52, 24V, 100 W, 2,200 min^{-1}) was used to suck in air from the room into the duct. A Biomax high-efficiency particulate air filter was used to keep the air clean. A Smart Fog humidifier (model 2016) was used to produce water vapor to control the humidity in the duct. The conditioned air then mixed with 1% HCl, balanced with air, through a static mixer. The flow is then straightened through four PTFE flow straighteners. The acid gas then interacts with the duct walls and is sampled through PTFE coated steel tubes powered by an ATI A21 gas sampler pump. The same HCl sensors used in the small-scale prototype reactor were used to capture HCl in the duct. Figure 2.14 shows a schematic of the flow facility while Fig. 2.15 illustrates the control panel with the sampling system. Three T-slotted motorized slides (placed near the inlet, outlet and middle of the duct) control the depth of gas sampling tubes, while a gas sampling pump draws air through the tube and gas sensor, and back into the duct near the outlet.

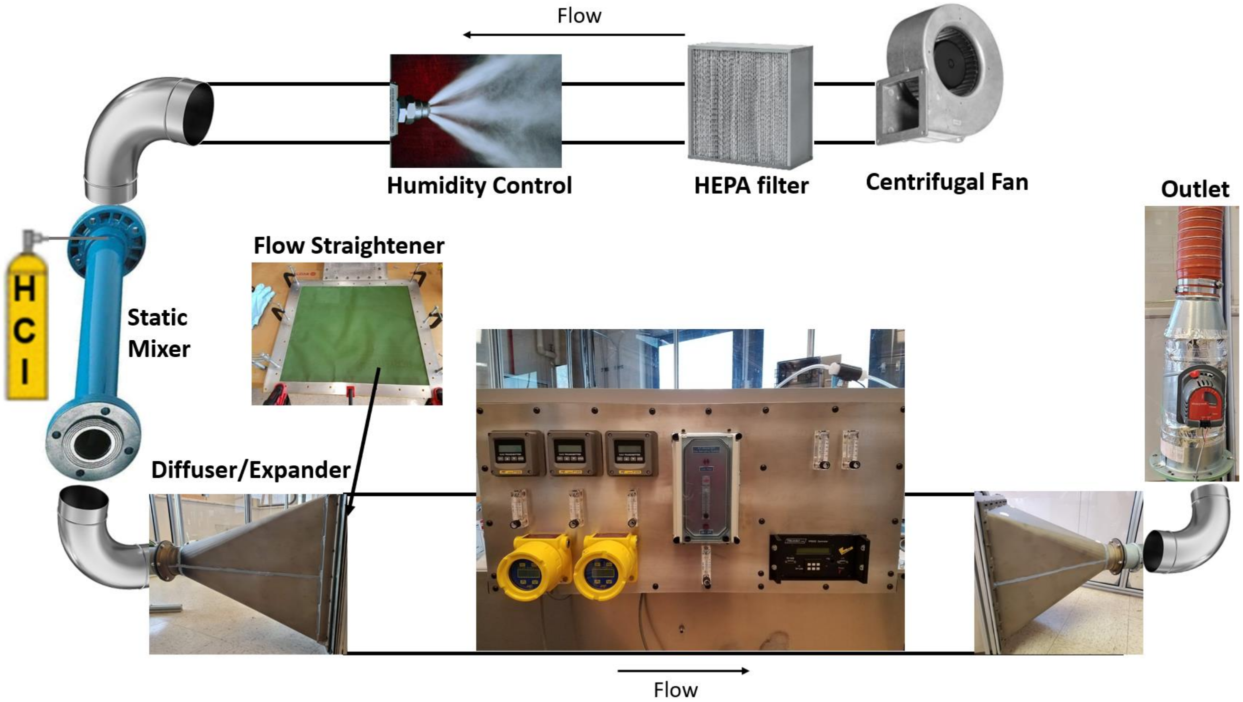

Figure 2.14: Large-scale acid gas flow facility.

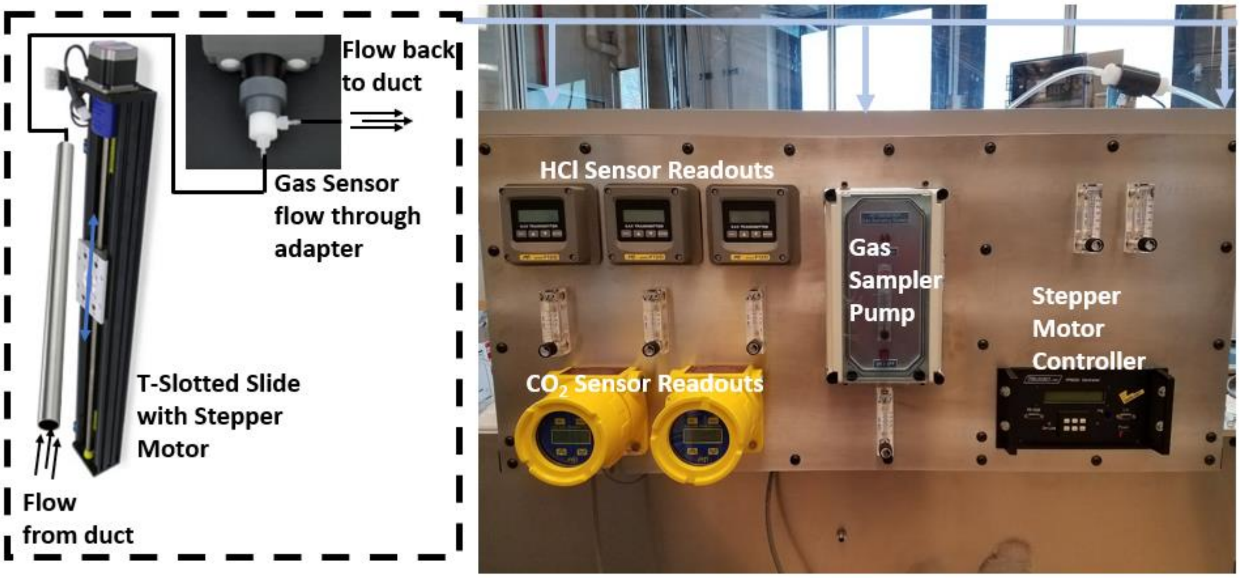

Figure 2.15: Large-scale duct control panel.

Chapter 3: REACTOR MODEL AND RESULTS

This chapter presents a model that was developed to predict HCl uptake in the same reactor that was used to measure HCl. The experimental setup and procedures have already been discussed in Chapter 2. Here, the data collected are used both for calibration of adjustable constants in the model, as well as for model validation. The experimental results show distinct differences in uptake characteristics between the different surfaces studied. As a starting point, a one-step global reaction with calibratable reaction rate constants was proposed to predict the experimental results. Following calibration, this model was validated against experiments for different flow speeds, concentrations, and sample surface area—conditions different from the dataset that was used for calibration. For the samples with no or small oxide layers (Nomex, stock and CCC), the model predicted the measured HCl uptake very well. For anodized aluminum, which has an order of magnitude thicker oxide layer, however, the model was found to be less accurate. The chapter concludes with a sensitivity study of the model.

3.1 Reactor Model

In the context of this study, a model of the test cell serves two purposes. First, as stated in Chapter 1, the experiments only measure inlet and outlet concentrations of HCl. Since concentrations of HCl at the aluminum surface are not directly measured, a model is necessary to connect the measured inlet and outlet concentrations of HCl to the rate of uptake (adsorption) of HCl by the aluminum surfaces. This step constitutes calibration of the reaction rate constants for the reaction occurring at the surface. Second, once the reaction rates have been determined (calibrated), the model can be used in a predictive capacity to explore scenarios beyond the regime in which the calibration was performed. A simple one-step kinetic model with unknown (calibratable) reaction rate constants is proposed and discussed next. This is followed by presentation of a computational fluid dynamics (CFD) model of combined mass transport and reaction of HCl that uses the reaction rate constants as inputs. The combination of these two models allows calibration of the reaction rate constants, as is discussed finally.

3.1.1 Surface Kinetics Model

The actual reactions occurring on the aluminum surface are quite complex, as has been mentioned in Chapter 1. There are many works that have studied the corrosion of aluminum and, hence, provide insight into the structure of the aluminum surface and the uptake of HCl. Alwitt [40] studied hydrous oxide film growth on aluminum and determined that in the presence of water vapor, the outer skin of the oxide film becomes highly porous. Volpe [33] studied the amount of moisture adsorbed onto an aluminum oxide surface and determined it varies with RH. The equivalent of approximately ten monolayers of water can be found at a RH level between 30 and 70% and 20°C, represented within the surface micropores. Doss and Condas [66] identified aluminum chloride as a specific product in the corrosion layer of aluminum exposed to indoor atmospheres. It has been proposed by Iannuzzi [67] that the aluminum chloride is formed by a stepwise chlorination of aluminum hydroxide. A detailed review of aluminum corrosion due to the atmosphere is given by Graedel [68].

Here, for engineering analysis purposes, we propose a simple one-step global reaction that models the uptake of HCl on the aluminum surface. This reaction is written as

$$\mathrm{HCl(g)} + \mathrm{s} \rightarrow \mathrm{HCl(s)} \tag{3.1}$$

where HCl(g) represents a gaseous HCl molecule arriving at the surface, s is an available (active) surface site, or dangling bond onto which an HCl molecule can adsorb, and HCl(s) is an adsorbed HCl molecule on the surface. The rate of disappearance of HCl is equal to the rate of aluminum surface site consumption, and may be written as

$$\frac{d[\mathrm{HCl}]}{dt} = \frac{d[\mathrm{s}]}{dt} = \dot{R} = k[\mathrm{HCl}]^{a}[\mathrm{s}]^{b} \tag{3.2}$$

where quantities within square brackets represent molar concentrations (kmol/m^3), and $\dot{R}$ is the molar reaction rate (in kmol/m^3/s). The last part of Eq. (3.2) utilizes the generalized law of mass action, where the concentrations have been raised to arbitrary exponents a and b rather than the stoichiometric coefficients. The reaction rate constant is denoted by k. It is commonly expressed by an Arrhenius rate expression. Here, following Coltrin et al. [54], an additional term that accounts for surface coverage is introduced to yield:

$$k = A_p T^{\beta} e^{-\frac{E_a}{RT}} \theta^{\mu} e^{-\frac{\varepsilon}{RT}} \tag{3.3}$$

where A_p is the pre-exponential factor, E_a is the activation energy, R is the universal gas constant, and T is the absolute temperature. β is the temperature exponent. The quantity, θ, denotes the surface coverage site fraction, or the ratio of the molar concentration of active sites to total sites. The total site concentration is sometimes referred to as the surface site density, ρ_{site}, and has units of µmol/m^2. The determination of this quantity for various types of aluminum surfaces from experiments has already been discussed in Ch. 2. Thus, $\theta = [\mathrm{s}]/\rho_{site}$. This site fraction starts at unity and decreases towards zero as active sites fill, which consequently brings k from a maximum value for a clean (unreacted) surface to zero for a filled (completely reacted) surface. The parameter, μ, is associated with the surface coverage. The parameter, ε, allows for the activation energy to also be a function of the surface coverage.

Since the experiments were conducted at near-room temperature, the temperature dependent terms may be treated as constants. Furthermore, it may be assumed that the reaction proposed in Eq. (3.1) is first order in HCl ($a = 1$) as evidenced in previous studies [51, 69]. Consequently, Eq. (3.3) simplifies to

$$\dot{R} = A[\mathrm{HCl}][s]\theta^{\mu} \tag{3.4}$$

where A is a new pre-exponential factor. Both A and μ are constants to be calibrated using experimental data, and the procedure for calibration will be discussed shortly. Since $\theta = [\mathrm{s}]/\rho_{site}$, the right-hand side of Eq. (3.4) suggests that the reaction rate is a nonlinear function of the site concentration, with the exponent being $1+\mu$. In principle, this exponent may be treated as a single calibratable parameter. However, in keeping with the literature, the site coverage dependence was kept separate, and μ itself was calibrated.

3.1.2 Computational Fluid Dynamics (CFD) Model of the Test Cell

As stated earlier in this chapter, the CFD model is necessary to establish the connection between the two aforementioned constants A and μ, and the measured concentration of HCl at the outlet. A model using ANSYS Fluent was developed for the reactor. Figure 3.1 shows a schematic of the reactor highlighting two inlets through which a mixture of HCl and dry air—of fixed mole fraction—is injected. The outlet vents to the ambient at a fixed atmospheric pressure. Using the inlet diameter, D, of $6.35\text{x}10^{-3}$ m, which produces a flow speed, u, of 0.53 m/s at 1000 ccm, and a kinematic viscosity, ν, of 1.5x10^{-5} m^2/s, gives a Reynolds number (as defined by Eq. 3.5) of 223. For this reason, a laminar flow model was used.

$$Re = \frac{uD}{\nu} \tag{3.5}$$

The aluminum sample serves as the reacting surface, while the outer walls of the test cell are assumed to be inert since the simulation begins after the walls are passivated. The simulations commenced ($t = 0$) at the instant when the test cell had been completely filled with the inlet mixture and the aluminum sample had just been placed in the test cell. With advancement of time, it is expected that the outlet concentration of HCl, [HCl], will drop since the HCl inside the test cell will be adsorbed by the aluminum sample. As the active sites on the aluminum sample get saturated (consumed), the adsorption rate is expected to decrease and ultimately go to zero (according to Eq. 3.4), at which point, the concentration of HCl is expected to increase back to the initial outlet concentration (at $t = 0$). Thus, if one were to plot the [HCl] versus time history at a point near the test cell outlet, it should depict a decrease followed by an increase back to the initial value of [HCl]. The CFD simulation was set up with the objective of mimicking the experiment. Depending on the rate constants (A and μ) chosen, the shape of the [HCl]-time curve is expected to be different, and the specific objective of the calibration process was to minimize the error between the predicted [HCl]-time curve and the experimentally measured [HCl]-time curve.

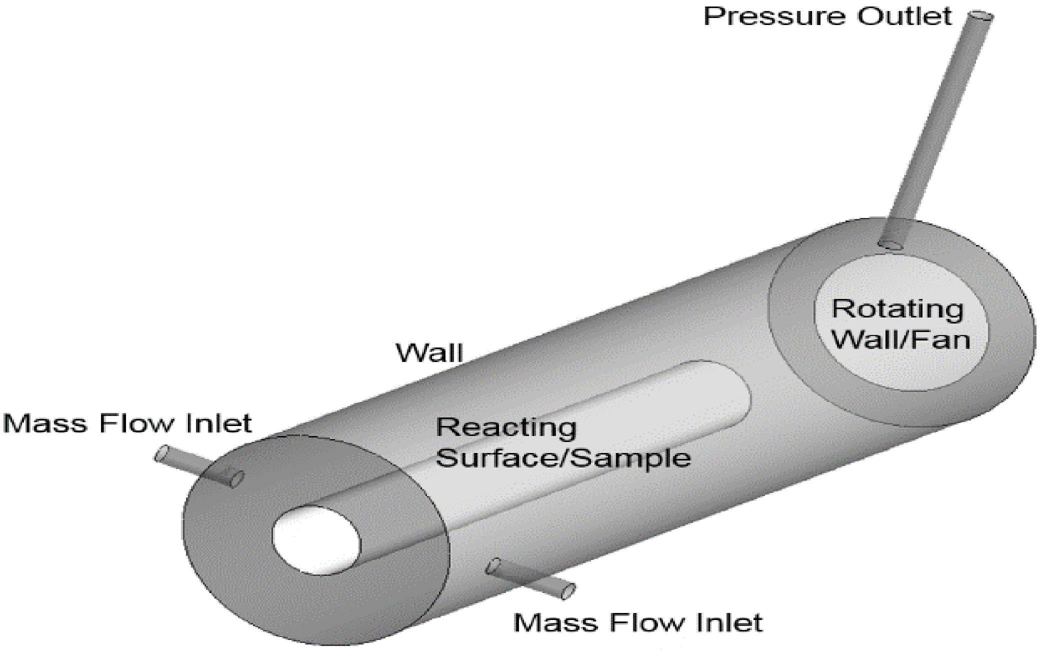

Figure 3.1: A three-dimensional schematic of the test cell.

In order to calibrate the rate constant more efficiently, an axisymmetric model was used since the calibration process requires several trials of the same calculation. Only 20,871 control volumes (cells) were needed for the axisymmetric model compared to the 366,337 cells needed for the 3-D model. A mesh independence study was conducted to determine the sufficient number of cells. This was achieved by increasing the mesh size by approximately 50% until the finest mesh and the second finest mesh only had a Sum Square Error (SSE), as defined by Eq. 3.6, of the [HCl]-time curve of below 0.1 ppm (0.23% of the inlet concentration). In Eq. 3.6, y is an experimental concentration measurement in ppm, $\bar{y}$ is the model concentration, and n is the number of data points. A time-step independence study determined that a time-step of 0.1 s was sufficiently small using the same requirement of the mesh independence study. The flow residence time, i.e., the time taken for a fluid particle to pass through the entire reactor, is on the order of 100 seconds. Since an axisymmetric model cannot fully mimic the real 3-D geometry, two different inlet flow

$$SSE = \sqrt{\frac{\sum\left(\frac{y-\bar{y}}{\bar{y}}\right)^2}{n}} \tag{3.6}$$

conditions were explored to assess geometric simplifications to the model: a front inlet and an annular inlet. These are shown in Fig. 3.2. The two models yielded almost identical results, due to similar residence times inside the reactor and contact between the surface and HCl. The annular inlet model was ultimately used for calibration.

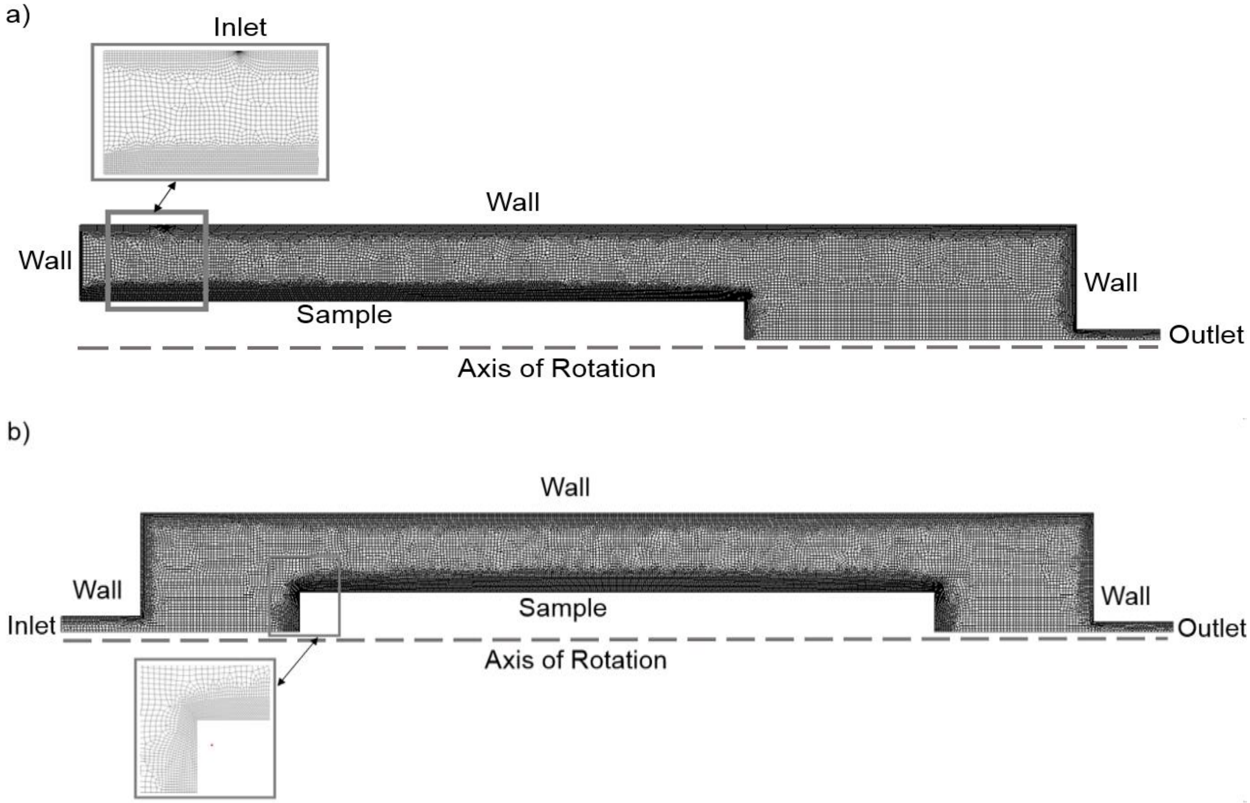

Figure 3.2: Axisymmetric models of a) Annular inlet model highlighting mesh at inlet and b) Front inlet model highlighting the mesh adjacent to the sample where the reaction takes place.

3.2 Model Calibration and Prediction

3.2.1 Calibration of Rate Constants

The kinetic constants *A* and *μ* were varied in an attempt to match the CCC experimental baseline test. The SSE between the experimental data and the model predictions was computed and monitored to obtain the best fit. Table 3.1 shows the SSE with different attempted values of *A* and *μ* as a percent of inlet concentration. It was observed that as *A* is increased, the minimum HCl concentration becomes lower. As *μ* becomes larger, the recovery happens faster. Figure 3.3 shows the comparison between experimental data and numerical results with the best fit: kinetic parameters of *A* = 30,000 and *μ* = 1.0. This produced a SSE of 2.92 % (shown in bold).

Table 3.1: SSE as a percent of inlet concentration (43.1 ppm) between measured [HCl] and computed [HCl] at the test cell outlet as a function of *A* and *μ*.

A	μ			
	0.5	0.75	**1**	1.25
25,000	5.22	3.62	3.60	5.10
27,500	5.63	3.51	3.22	4.34
30,000	6.37	4.72	**2.92**	3.76
32,500	6.58	4.428	3.01	3.83

As noted earlier, the kinetic constants were calibrated using an axisymmetric model with an annulus inlet condition. In order to test the validity of the calibrated kinetic constants for the real (three-dimensional) test geometry, the computations were repeated in 3D with the actual front inlet. Figure 3.4 shows the predicted results of both types of 2D inlet models, as well as the 3D model, along with the experimental data. It is evident that the location of the inlet in the two 2D models has little bearing on the predicted results, justifying the use of the annular inlet during the calibration phase. Further, Fig. 3.4 exhibits excellent agreement between predictions of the three models and the experimental data, lending credibility to the calibrated kinetic constants.

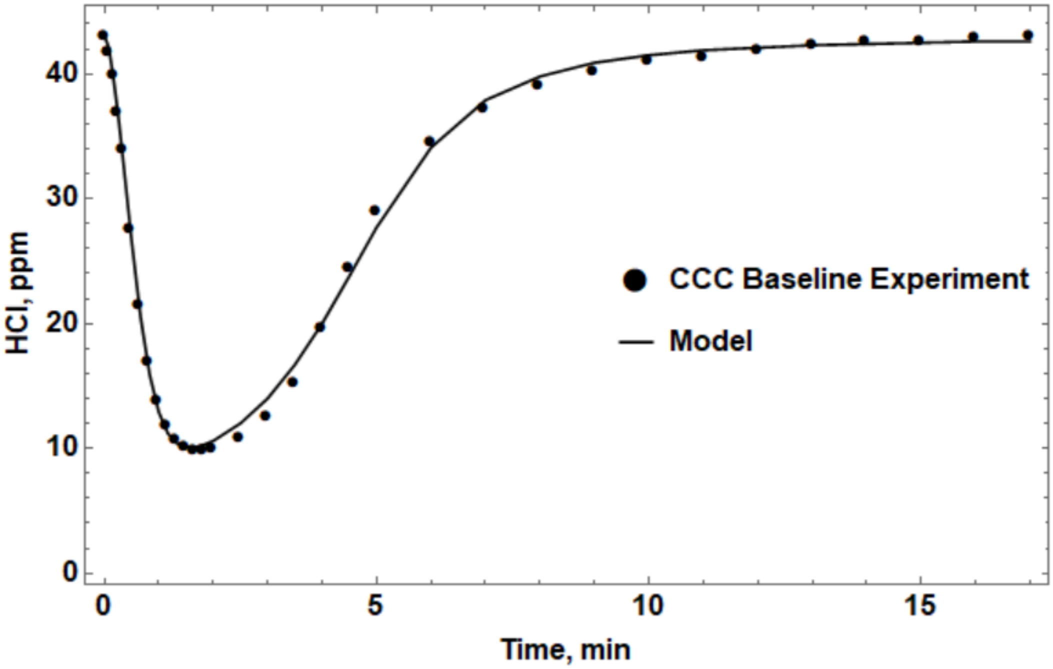

Figure 3.3: HCl concentration-time history using the best-fit calibrated model: *A =30,000 and μ = 1.0.*

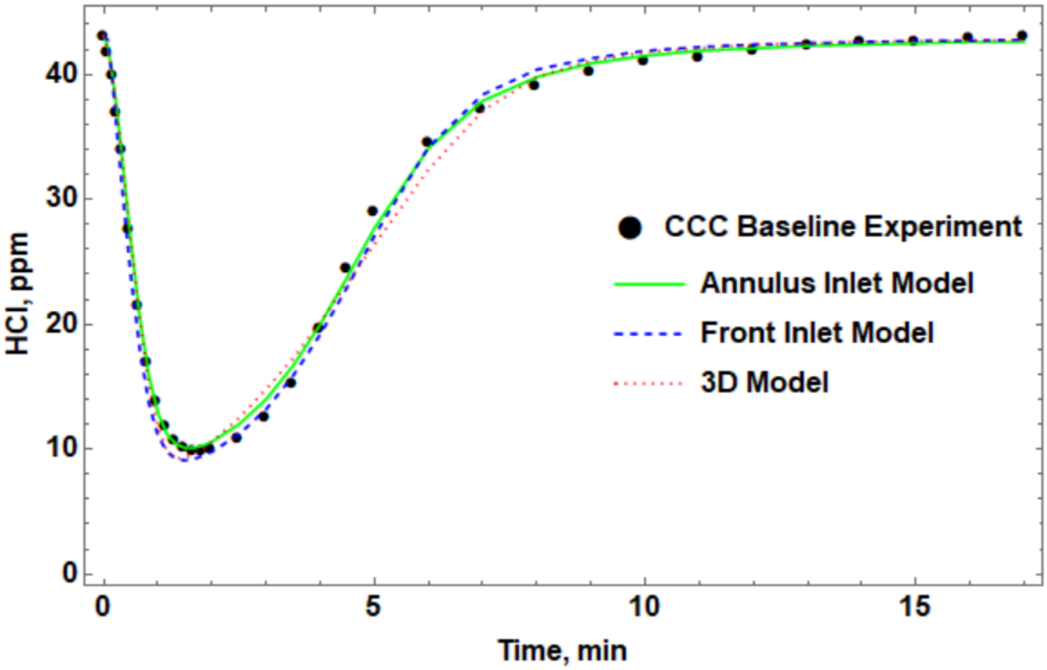

Figure 3.4: Comparison of HCl uptake predicted with 2D annulus inlet, 2D front inlet, and 3D models to experimental data for the baseline case.

3.2.2 Validation Studies

The calibrated kinetic parameters were next used to predict other experimental cases, i.e., datasets that are different from the one used to calibrate the model. Figure 3.5 shows the model prediction for a case where 2 lpm was used for the inlet flow rate. The model slightly overpredicts how much the concentration dips (the minimum point) and how fast it decreases, but there is excellent agreement on the recovery and how fast the sample becomes saturated. The CCC baseline experiment case is shown for comparison to illustrate that the time span of this experiment is significantly different than the baseline case. Figure 3.6 shows a comparison of model prediction with experimental data for a case where the sample length is 10.2 cm. As in the previous case, the model underpredicts the decrease in HCl slightly, but, once again, predicts the rise phase quite well. The next case considered for testing the predictive ability of the model uses approximately half the baseline inlet concentration (21 ppm) of HCl. Figure 3.7 shows the results of this case. The predicted results exhibit excellent match against experimental results in both the fall and rise phases.

The same model with the same kinetic constants were used to validate the computed results against experimental data collected for the stock and anodized aluminum samples under baseline conditions. The surface site density was changed to 76.2 and 2,900 μmol/m^2 for the stock and anodized samples, respectively, in keeping with the total uptake by the two samples, as described earlier. Figure 3.8 depicts the predicted and experimental results for the stock aluminum sample. The model shows good agreement overall. Figure 3.9 shows the results for the anodized sample. The model underpredicts the fall and, also, predicts a slower recovery. Overall, the stock aluminum

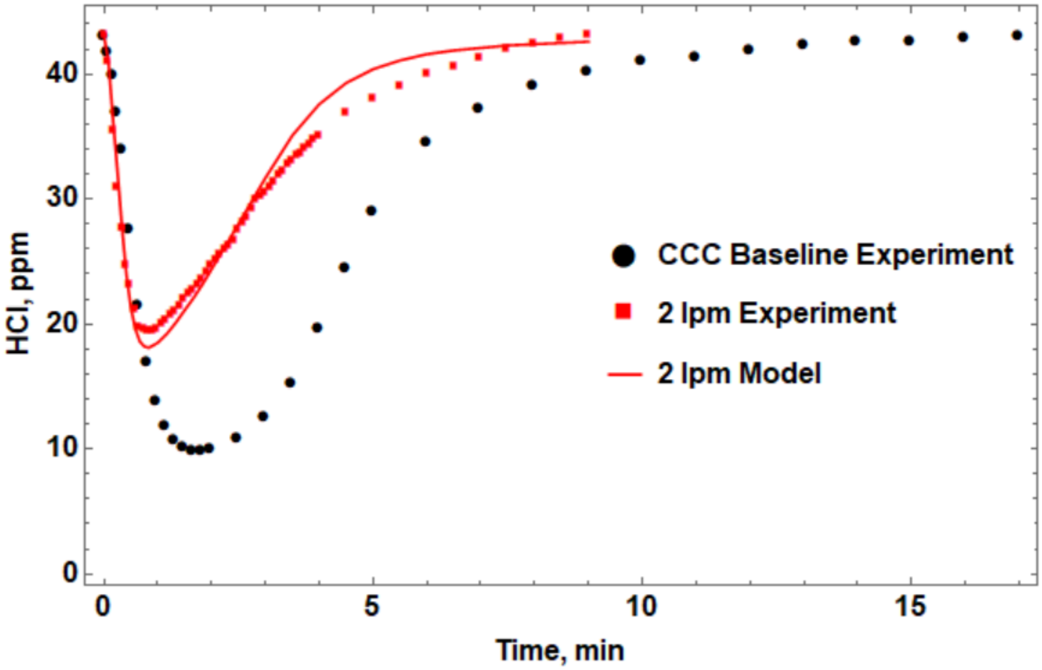

Figure 3.5: Comparison of model predictions and experimental data for a case with HCl flow rate of 2 lpm.

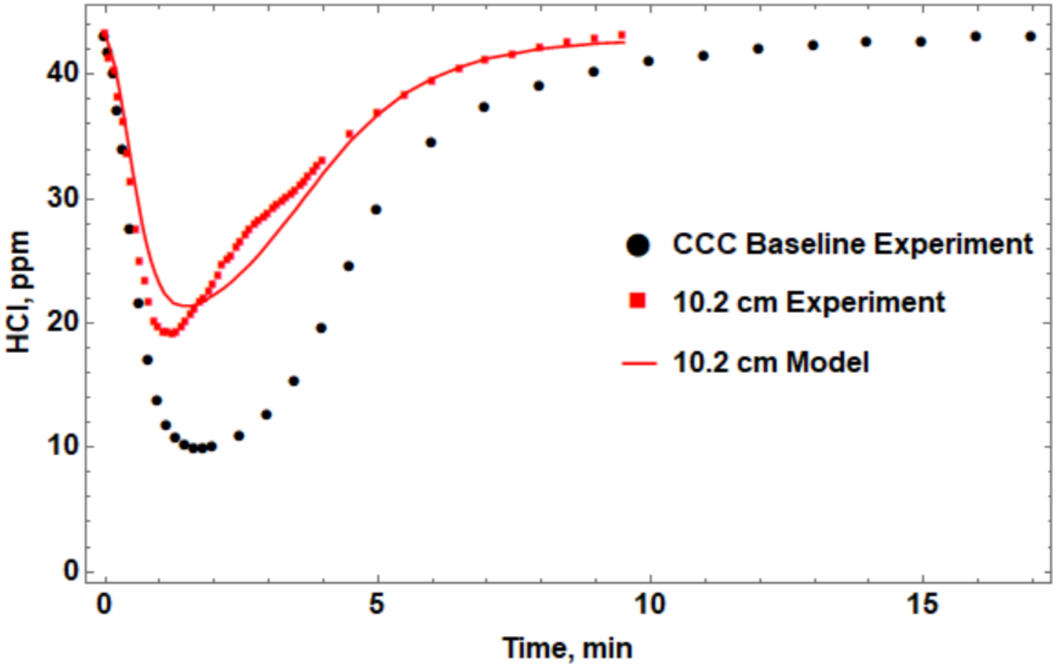

Figure 3.6: Comparison of model predictions and experimental data for a case with a sample length of 10.2 cm.

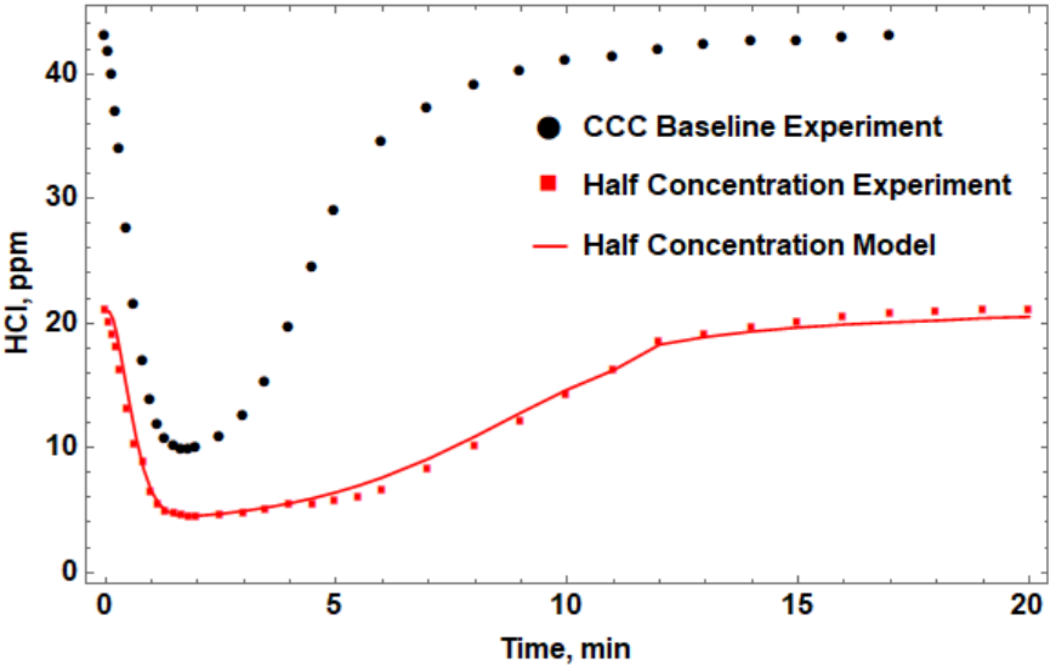

Figure 3.7: Prediction of half baseline inlet concentration case.

exhibits a better match, as compared to the anodized aluminum samples. Table 3.2 lists the SSE for all aluminum cases considered for this validation study. Based on the experience gained from the calibration of the kinetic constants for the CCC samples, a better match could be obtained for the stock sample by decreasing *A*. However, in the interest of keeping the calibrated kinetic rate constants more general, the decision was made to keep them unchanged, especially since the discrepancies between predicted and experimental results are small and the experiments have their own uncertainty (as shown in Fig. 2.8).

While Nomex is a different type of surface, the engineering model was able to predict its uptake of HCl as well. Figure 3.10 presents the experimental data for Nomex as well as its prediction. Integrating the experimental curve using Eq. 2.1 gives a ρ_{site} of 814 µmol/m^2. An *A* and μ value of 8,250 1/s and 2.0 presented the best match respectively.

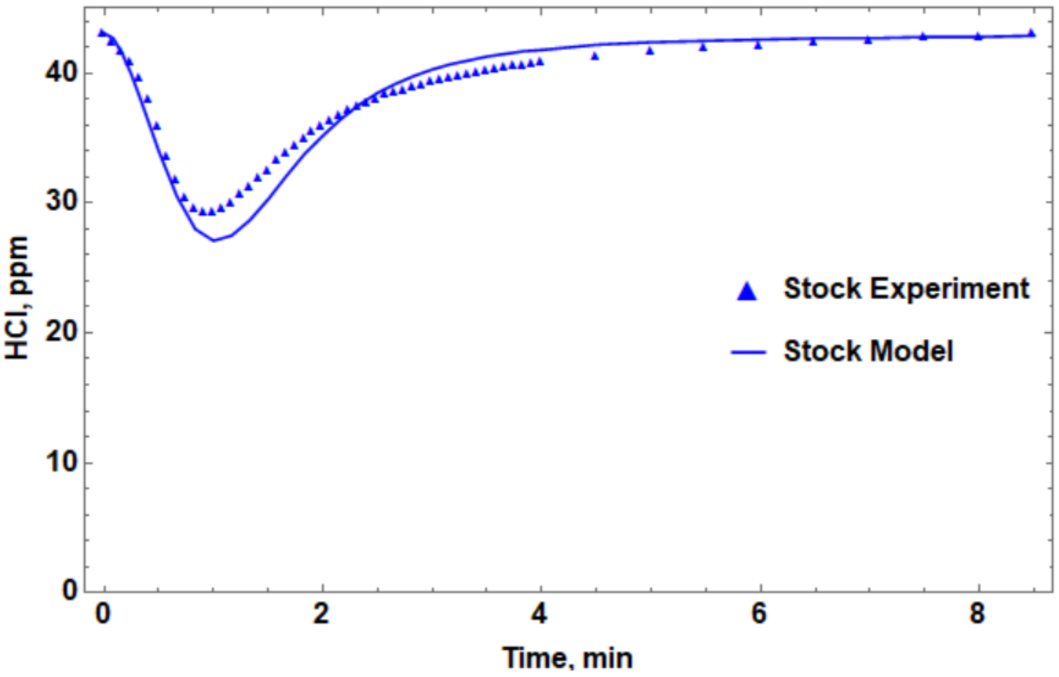

Figure 3.8: Comparison of model predictions and experimental data for the stock aluminum sample.

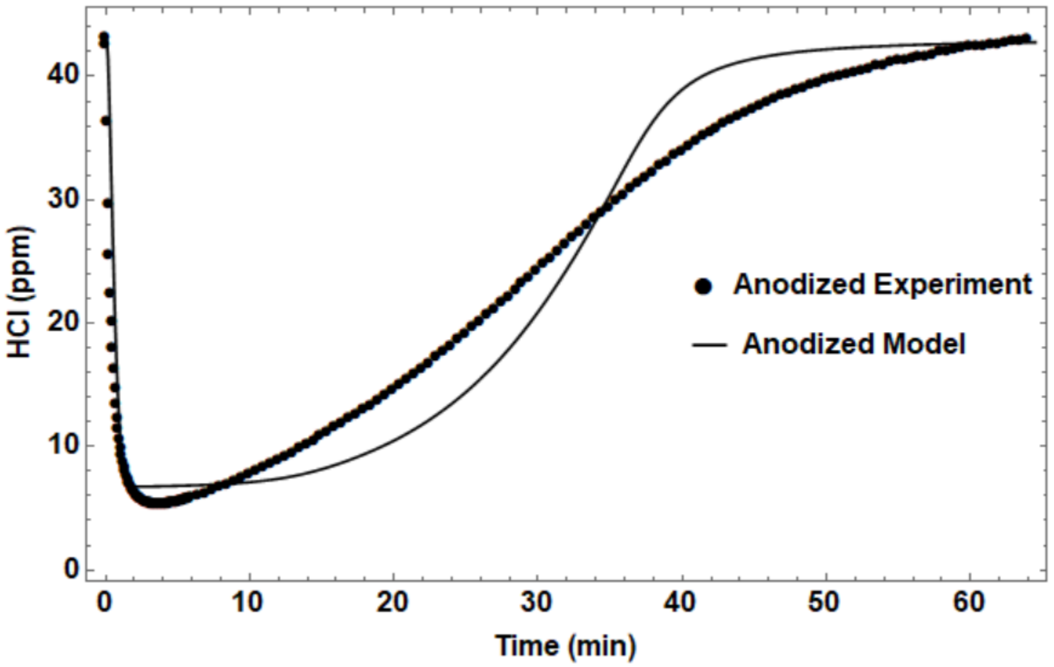

Figure 3.9: Comparison of model predictions and experimental data for the anodized aluminum sample.

Table 3.2: SSE between model and predictive cases.

Test	SSE (%)
2 lpm	5.15
10.2 cm Length	4.12
Half Baseline Inlet Concentration	6.69
Stock	4.63
Anodized	12.87

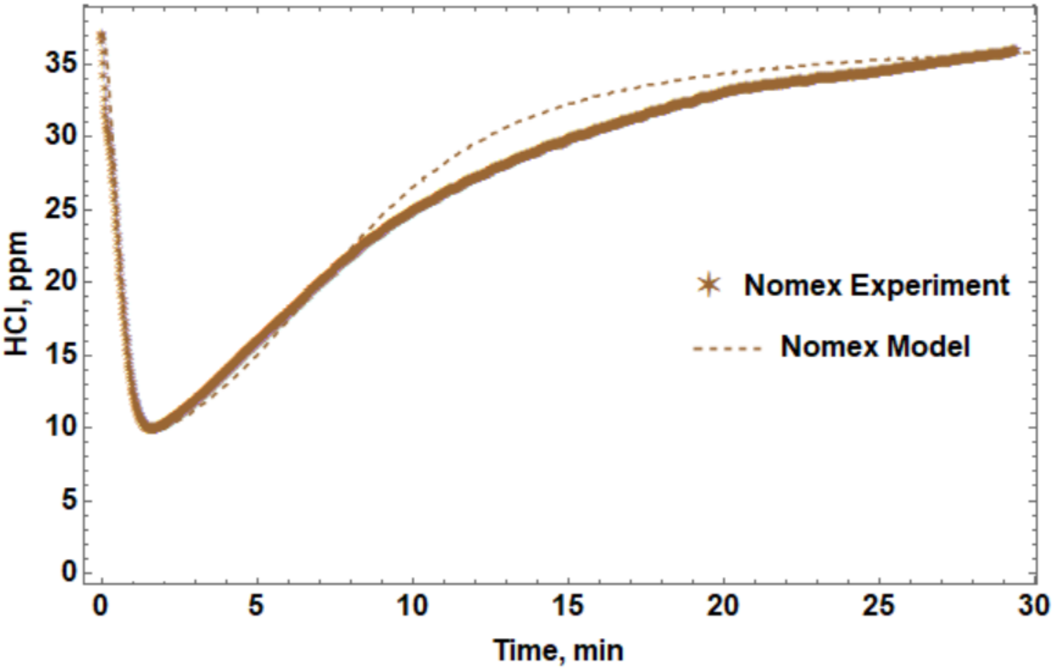

Figure 3.10: Comparison of model predictions and experimental data for the Nomex sample.

The proposed model hypothesizes that the mechanism which produces the shape of the experimental HCl concentration-time curves is HCl molecules filling active aluminum (or other) surface sites solely due to adsorption. The model results support this hypothesis. Various surface techniques were used to investigate this hypothesis further. It is well known that aluminum has a natural oxide layer, and surface treatments enhance this oxide layer to protect the surface from corrosion. X-Ray Photoelectron Spectroscopy (XPS) was used to measure the oxide layer thickness. It was found that the stock aluminum samples had an oxide layer thickness of 50 nm and the CCC samples had a thickness of 200 nm. The anodized aluminum samples were found to have too thick of an oxide layer to be measured by XPS, so Focused Ion Beam (FIB) was used to determine the oxide layer thickness, which was determined to be 5,500 nm. The positive correlation between oxide layer thickness and HCl uptake is evident in the results shown in the preceding section. This could imply that HCl is diffusing into the oxide layer of the sample. This could also explain why the model calibrated from the CCC sample matched the stock and Nomex samples better than the anodized since the oxide layer thicknesses are closer in magnitude.

Further XPS studies were conducted on aluminum exposed to HCl. Chlorine, in the form of aluminum chloride likely formed from the reaction of aluminum and HCl, was found in all cases. Chlorine was found as deep as 5 nm in the oxide layer for the stock aluminum samples, 50 nm in the CCC aluminum samples, and 2,300 nm in the anodized samples. For all three sample types, at the surface, ~2% chlorine was found. It is not surprising that chlorine was able to diffuse further into the treated alumina as the acid bath that these treatments subjected the surfaces to made them more porous.

3.2.3 Sensitivity Analysis

The discrepancies between model predictions and experiments could be attributed, in part, either to uncertainties in the experimental data that were used for calibration or as inputs (boundary and initial conditions) in the CFD model. In this section, we attempt to quantify the effect of these uncertainties on the predicted results. The measurement uncertainties of all instruments involved are shown in Table 3.3. The value in the left column is the raw uncertainty, whereas the value in the right column is the uncertainty normalized by the baseline condition and presented as a percentage. The largest normalized uncertainty is in the flow rate, which is 1.0% of the full range of the flow meter and is 5.0% of the baseline flow rate of 1000 ccm. The baseline model was simulated again with a flow rate of 950 ccm and 1050 ccm to determine the sensitivity of the model to flow rate uncertainty. This is shown in Fig. 3.11. The lower the flow rate, the lower the minimum HCl concentration and the slower it reaches that minimum. The SSE between the model predictions for the baseline flow rate (1000 ccm) and the 950 ccm flow rate is 2.45% and the SSE between the model predictions for the baseline flow rate and the 1050 ccm flow rate is 2.16 %. These values are comparable to the values shown in Table 3.3, indicating that the error (discrepancy with measured values) in the predicted results could be attributable to uncertainties in the boundary conditions in the model—flow rate, in this particular instance.

Table 3.3: Uncertainties of measured values.

	Raw Uncertainty	Normalized by baseline (%)
Flow rate	50 ccm	5
Sample length	0.08 cm	0.39
Sample Diameter	0.02 cm	0.79
HCl concentration	0.1 ppm	0.23
Pressure	600 Pa	1
Temperature	0.1 K	0.03

The model was exercised further by introducing uncertainties in the sample length, i.e., for sample lengths of 20.3 ± 0.08 cm. The SSE between baseline model prediction and the model prediction for the sample of length 20.3 + 0.08 cm and 20.3 - 0.08 cm was found to be 0.21%. This is an insignificant difference as shown in Fig. 3.11 and highlights the fact that the results are less sensitive to uncertainties in the measured length of the sample.

The site density is a value that is calculated by integrating the experimental HCl concentration-time curve, as explained earlier and provided by Eq. 2.1. The uncertainty of this

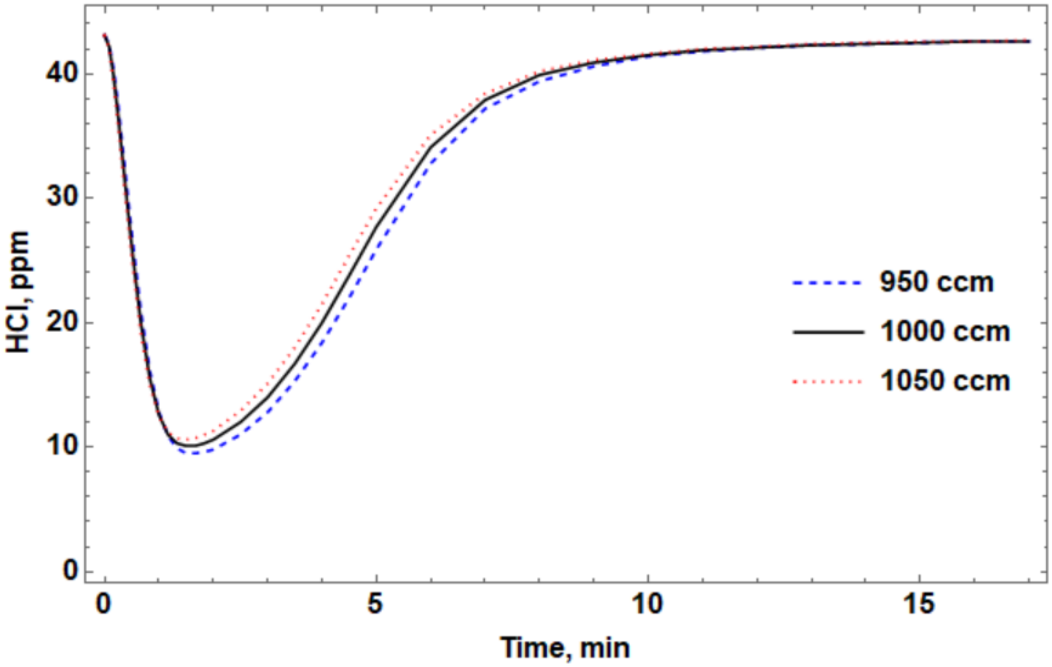

Figure 3.11: Sensitivity of model predictions to changes in flow rate.

value can be deduced from the general uncertainty equation and knowing the uncertainty of each part of the equation. The mass flow rate and its uncertainty are defined by Eqs. 3.7 and 3.8 respectively. Mass flowrate is simply the volume flow rate times the density, which can be found from the known pressure and temperature using the ideal gas law. At baseline, the mass flow rate is 2x10^{-5} kg/s and its uncertainty is 1x10^{-6} kg/s. The surface area of the sample is defined by Eq. 3.9, and its uncertainty by Eq. 3.10, which is 1.62x10^{-2} m^2 and 3.65x10^{-4} m^2 respectively. The uncertainty of adding the HCl mass fractions is shown in Eq. 3.11. Using the definitions provided by Eq. 3.7 through 3.11 in Eq. 3.12 gives the uncertainty of the site density, which for the baseline case is 22 µmole/m^2, or 5.83% of baseline uptake.

$$\dot{m} = \dot{V}\frac{P}{RT} \tag{3.7}$$

$$U_{\dot{m}} = \dot{m}\sqrt{\left(\frac{U_{\dot{V}}}{\dot{V}}\right)^2 + \left(\frac{U_P}{P}\right)^2 + \left(\frac{U_T}{T}\right)^2} \tag{3.8}$$

$$A = \pi D L \tag{3.9}$$

$$U_A = A\sqrt{\left(\frac{U_D}{D}\right)^2 + \left(\frac{U_L}{L}\right)^2} \tag{3.10}$$

$$U_{Y_{HCl,1}+Y_{HCl,2}} = \sqrt{\left(Y_{HCl,1}\right)^2 + \left(Y_{HCl,2}\right)^2} \tag{311}$$

$$U_{\rho_{site}} = \rho_{site}\sqrt{\left(\frac{U_{\dot{m}}}{\dot{m}}\right)^2 + \left(\frac{U_A}{A}\right)^2 + \left(\frac{U_{Y_{HCl,1}+Y_{HCl,2}}}{Y_{HCl,1}+Y_{HCl,2}}\right)} \tag{3.12}$$

Figure 3.12 shows the model's sensitivity to the change in site density. The SSE between the baseline model and the predictive model with the large site density is 1.84%, while the SSE between the baseline model and the predictive model with less sites is 2.97%. It is noticed that the SSE between the baseline and smaller site density models is significantly larger than between the baseline and larger site density models. The value 22 µmole/m^2 represents 5.83% of baseline, which is on the order of uncertainty as the flow rate. Since the uncertainty of the flowrate is used in the definition of the uncertainty for site fraction, it is expected that the uncertainty is higher. The fact that the two uncertainties are so close in value indicates that the uncertainty in site density is caused primarily because of the uncertainty in flow rate. The sensitivity of the model to both these values is comparable to the errors between experimental and modeled results.

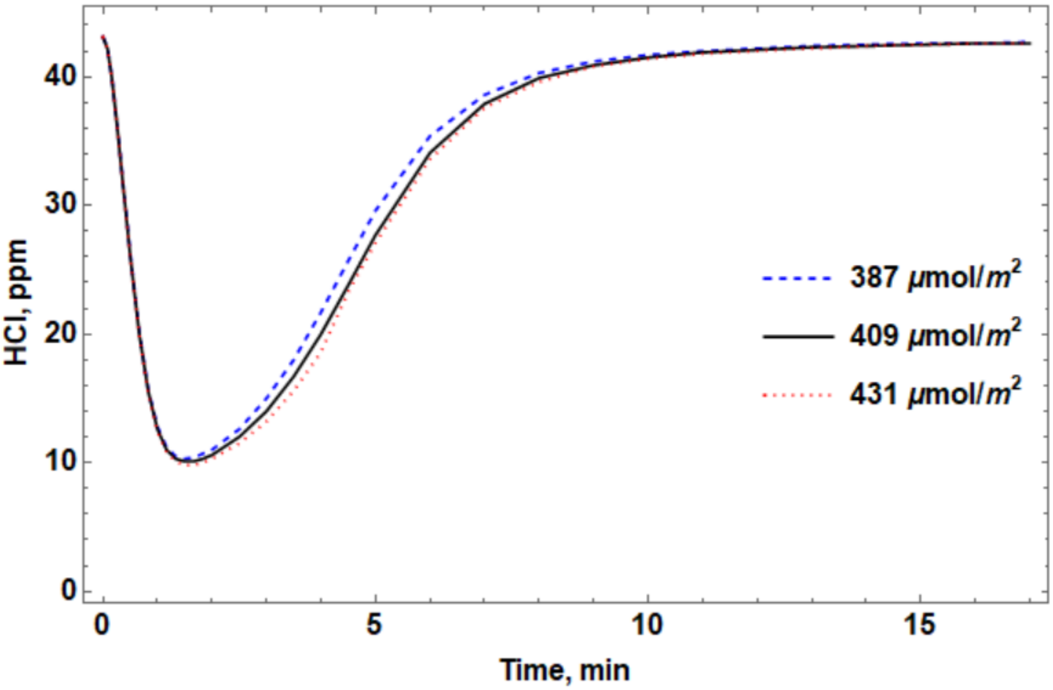

Figure 3.12: Sensitivity of predicted outlet HCl concentration-time histories to change in site density.

3.3 Summary

Experimental results from the reactor gave the HCl uptake capacity for three different types of aluminum (stock, CCC and anodized), as well as Nomex. Kinetic parameters for the reaction of HCl with aluminum surfaces were determined by calibrating rate constants used as inputs in an axisymmetric CFD model against an experimental dataset. A single reaction step for HCl adsorption with a first-order Arrhenius surface kinetics expression that accounted for active surface sites gave excellent agreement with experimental data. The model was calibrated using experimental data for the CCC surface treatment, but the same kinetic parameters were also successful in predicting the experimentally observed behavior of CCC under different flow rates, concentrations, and surface areas, as well as stock aluminum. The experiments showed that the anodized aluminum samples had the most HCl uptake, followed by the CCC aluminum samples.

This study uncovered a positive correlation of HCl uptake to the oxide layer thickness resulting from different types of aluminum surface treatment. Data generated by this work suggests that, in a real spacecraft fire, HCl and other acid gasses will not stay in the atmosphere long, making them hard to track and difficult to monitor for fire detection. The fact that atomic chlorine was found on the surface and within the oxide layer has implications for postfire cleanup as well. The model predicts the uptake of HCl best with lower-capacity surfaces but certainly with acceptable accuracy for all surfaces at shorter scales, making it an excellent predictive tool if the smoldering fire is detected and extinguished within approximately 5 min.

XPS found chlorine at the surface and within the oxide layer, which is likely in the form of aluminum chloride. A likely reason that the model was not able to predict the anodized aluminum uptake as well as the other surfaces is due to this aluminum chloride that was produced by the transport of HCl deep into the oxide layer. The aluminum chloride adds additional mass transport resistance that needs to be accounted for in order to yield a more accurate prediction. In the next chapter, a multiscale model is explored—one that also accounts for the transport of HCl into the oxide layer, and its reaction with the pore walls of the oxide layer.

Chapter 4: MULTISCALE MODEL AND RESULTS

The previous chapter presented the results of a reactor model with a single global reaction rate that predicted the HCl uptake of stock and CCC aluminum well. The same model was not able to predict the uptake of HCl by anodized aluminum as well as other surface types. In this chapter, a multiscale model is developed to predict HCl uptake by anodized aluminum, which has a thick oxide layer covering its surface compared to other treatments. X-ray photoelectron spectroscopy (XPS) revealed that aluminum chloride is found deep in the oxide layer of anodized aluminum, implying that the pore-scale transport and reaction of HCl within the oxide layer covering the aluminum surface must be considered. Hence, a multiscale approach is warranted. A pore-scale model is first developed wherein the HCl reacts with the aluminum oxide pore walls to create an aluminum chloride layer. The HCl then diffuses through that layer for further reaction, until the layer (diffusion resistance) grows too large, and uptake of HCl stops. This pore-scale model is coupled with a reactor-scale model, resulting in the *multiscale* model, to predict overall HCl uptake.

4.1 Pore-Scale Model Development

The experimental work shown in Chapter 3 measured the uptake of HCl by treated and untreated aluminum within a prototype reactor. A single (reactor)-scale numerical model of the reactor was developed wherein a one-step global reaction that accounted for active surface reaction sites was used for modeling HCl uptake. For stock (or untreated) and CCC aluminum samples, the model yielded results that matched experimental HCl uptake curves quite well, as seen in Ch. 3.

When used for anodized aluminum, however, the predictions by the same model did not agree as well with experimental data. The stock aluminum and the CCC aluminum were inspected using XPS and was found to have oxide layer thicknesses of 50 and 200 nm, respectively, while the anodized aluminum was found to have an oxide layer thickness of 5,500 nm. XPS also revealed the existence of chlorine deep within the oxide layer indicating formation of aluminum chloride due to reaction of alumina with HCl. With an oxide/chloride layer that is an order of magnitude thicker, it is hypothesized that the mass transport (diffusion) resistance of the layer to HCl becomes critical and the effect of diffusion and reaction within the pores of the layer must be accounted for. Table 4.1 shows the XPS findings, as well as the uptake determined in Ch. 3 by each type of aluminum.

Table 4.1: Oxide layer thickness, depth at which chlorine is found within the oxide layer after a test, and site density of aluminum used in the study.

Aluminum Treatment	Depth of Oxide Layer (nm)	Depth Chlorine Found by XPS (nm)	Site Density μmol/m^2
Stock	50	5	76.2
CCC	200	50	409
Anodized	5,500	2,200	2,900

Modeling the diffusion of HCl through the pores of the oxide/chloride layer and its subsequent reaction within the framework of a reactor-scale model poses certain challenges. On account of the huge disparity in length scales, it is not feasible to model the diffusion through the pores of the layer within the reactor-scale model. In other words, the same mesh that resolves the inside of the reactor cannot be also used to resolve the pores within the layer covering the aluminum surface. It is with this difficulty in mind, a separate pore-scale model was first developed and used to compute the growth of the aluminum chloride layer and its effect on HCl uptake. This pore-scale model is at the subgrid-scale of the reactor model, i.e., the pore-scale model operates at a length scale that is smaller than the size of a typical control volume of the reactor-scale model. This pore-scale model assumes the pores to be cylindrical (see Fig. 1.4) and the reaction of HCl with aluminum oxide (alumina) pore walls to create aluminum chloride is considered. The HCl then diffuses through the thickening aluminum chloride layer to react with alumina. The reaction stops when the diffusion resistance due to the growing aluminum chloride layer becomes too large for more HCl to make it to the available alumina. The output of this pore model was ultimately used within the reactor-scale model to result in what is referred to here as a *multiscale* model (conceptualized in Fig. 4.1). This is accomplished by calibrating the diffusion resistance to be used within the reactor-scale model to the data for HCl uptake obtained from the pore-scale computations. Starting from a time-dependent decrease in diffusion coefficient, an expression for the diffusion coefficient as a function of HCl wall concentration was developed to make the expression more general and applicable to other operating conditions.

To account for the mass transport and reaction (formation of aluminum chloride) within the oxide layer, a pore-scale model was developed for a single pore in the oxide layer. Since the actual pore structure is very complex, a single cylindrical pore is modeled to capture the aforementioned phenomenon. Furthermore, a 2D axisymmetric model was used for the pore, with the top boundary condition being of constant concentration and a boundary condition set at the pore walls representing the reaction of HCl with alumina. In this model, the reaction at the pore wall creates a solid aluminum chloride layer that the HCl must diffuse through to further react (see subfigure C of Fig. 4.1). Once the layer grows too thick, the reaction slows to a stop. HCl transport through the pore is described by the 2D transient diffusion equation [70]:

$$\frac{\partial c}{\partial t}=\frac{1}{r}\frac{\partial}{\partial r}\left(rD_{eff}\frac{\partial c}{\partial r}\right)+\frac{\partial}{\partial z}\left(D_{eff}\frac{\partial c}{\partial z}\right) \tag{4.1}$$

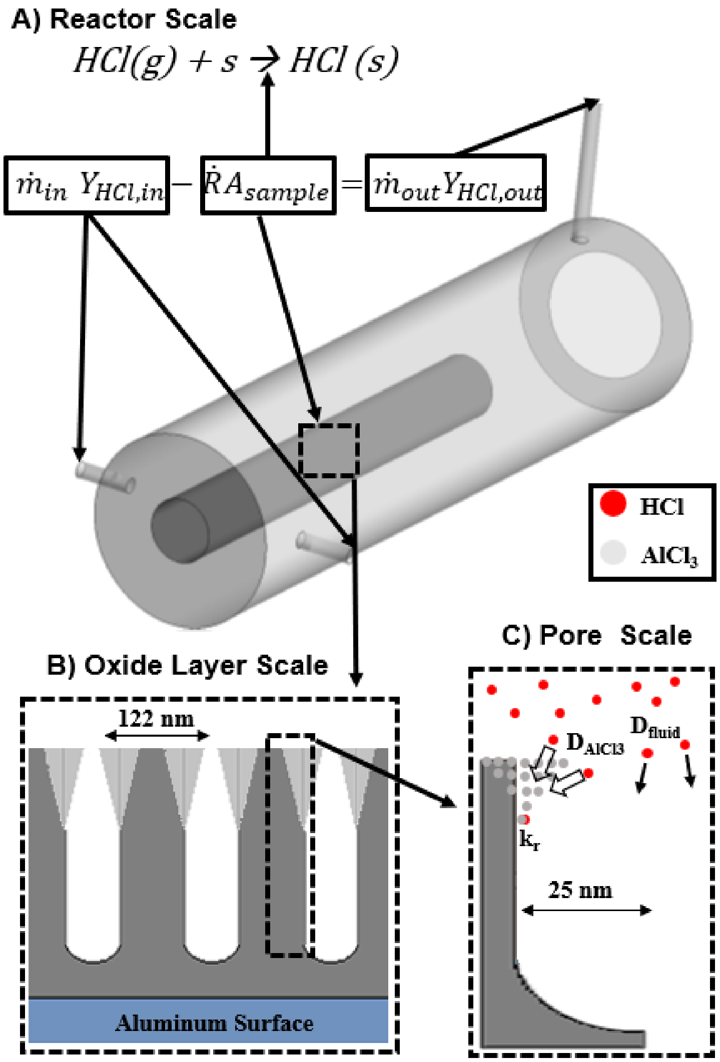

Figure 4.1: Multiscale modeling framework: the reactor-scale model is shown in (A). Additional scales, namely the oxide layer scale (B) and a single pore within the oxide layer, i.e., the pore-scale model (C) is also schematically illustrated.

The molar concentration of HCl(g) is denoted by c (= [HCl(g)]), while its effective diffusion coefficient is denoted by D_{eff}. t denotes time, while z and r denote the axial and radial spatial locations, respectively. The boundary condition at the pore-alumina interface (Fig. 2C), where the reaction between HCl and alumina occurs, is written as [71]:

$$-D_{eff} \left.\frac{\partial c}{\partial r}\right|_{r=r_w} = \dot{R} = -k_{pore}c_w \tag{4.2}$$

where r_w is the radial location of the surface on which reaction occurs, i.e., the pre wall. $k_{pore}c_w$ is the molar reaction rate at the pore wall— k_{pore} being the reaction rate constant for reaction between aluminum oxide and HCl, and c_w being the concentration of HCl at the pore wall. Here, due to lack of better information, it is assumed that the reaction between HCl and aluminum oxide is first order in HCl. To solve Eq. (4.1), subject to the boundary condition provided by Eq. (4.2), the pore is discretized into a set of control volumes, as shown in Fig. 4.2. Eq. (4.1) is then discretized using the finite volume method [72]. The concentration of HCl at every control volume (cell) center is determined by solving the resulting set of algebraic equations. Time advancement is implemented using the implicit backward Euler method [72]. The mass of aluminum chloride formed due to chemical reaction during a time interval *Δt* is given by:

$$m_{AlCl3} = M\ k_{pore}\ c_w\ A_w\ \ \Delta t \tag{4.3}$$

where $k_{pore}c_w$ is the molar reaction rate. When multiplied with the molar mass of aluminum chloride, *M*, the area over which the reaction occurs, A_w, and the time interval over which the reaction occurs, *Δt*, the mass of $AlCl_3$ can be calculated. Using stoichiometry and the density of each material, the volume of aluminum oxide consumed, and aluminum chloride produced, can also be computed. In the cells adjacent to the original pore wall that are originally occupied by aluminum oxide, the volume of the aluminum oxide is replaced with aluminum chloride. The boundary condition for the pore wall is then moved to the next face of the cell. Since the density of $AlCl_3$ is smaller than that of Al_2O_3, more volume of $AlCl_3$ is created than Al_2O_3 is destroyed. Hence, the excess volume is used to fill the cells on the open pore side. The process of filling the cells on the open pore side is similar to the process of filling the pore wall side, with the volume of $AlCl_3$ replacing the open pore (fluid) volume. The entire process of cells filling with new material, calculation of the volume fractions of each material, and movement of the face at which the boundary condition applied is executed dynamically at each time step. When a cell is more than half full, the face at which the boundary condition is applied is moved suddenly from the receding face to the approaching face of the cell. Although this is somewhat unrealistic, it is a

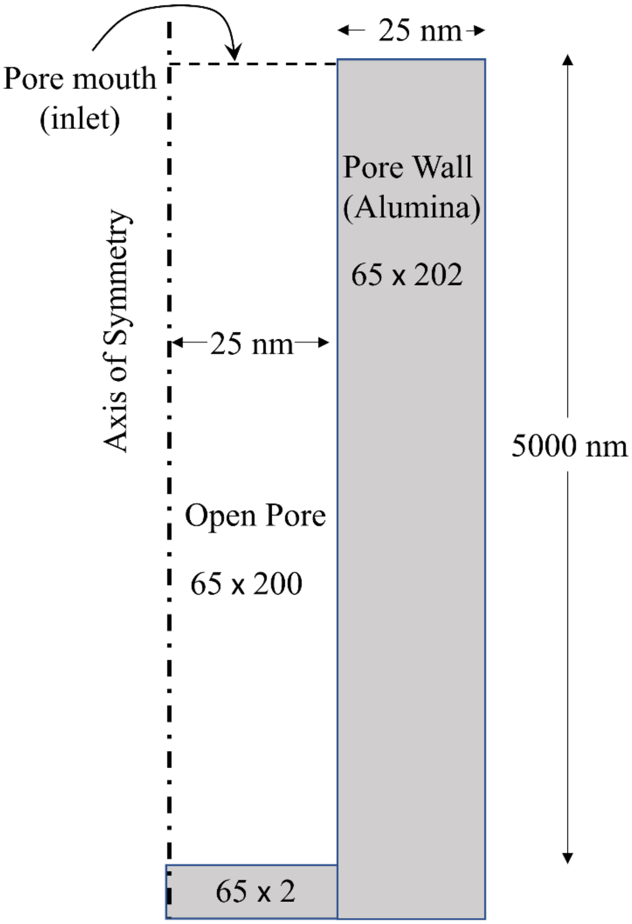

Figure 4.2: Schematic of the pore-scale model showing an axisymmetric view of a single pore. The number of control volumes (cells) used in each region is also shown.

limitation that is inherent to using a fixed grid for tracking the front. This process is demonstrated in Fig. 4.3. The effective diffusion coefficient of each cell is also calculated dynamically. The process starts with cells filled completely either with fluid or alumina. Hence, the effective diffusion coefficient, D_{eff}, is either equal to D_{fluid} or D_{Al2O3}, where D_{fluid} and D_{Al2O3} are diffusion coefficients of HCl in the open pore (fluid) and solid alumina, respectively. As the reaction proceeds, some cells within the original pore get partially filled with aluminum chloride. In such a scenario, the diffusion coefficient of the mixed cell is calculated as:

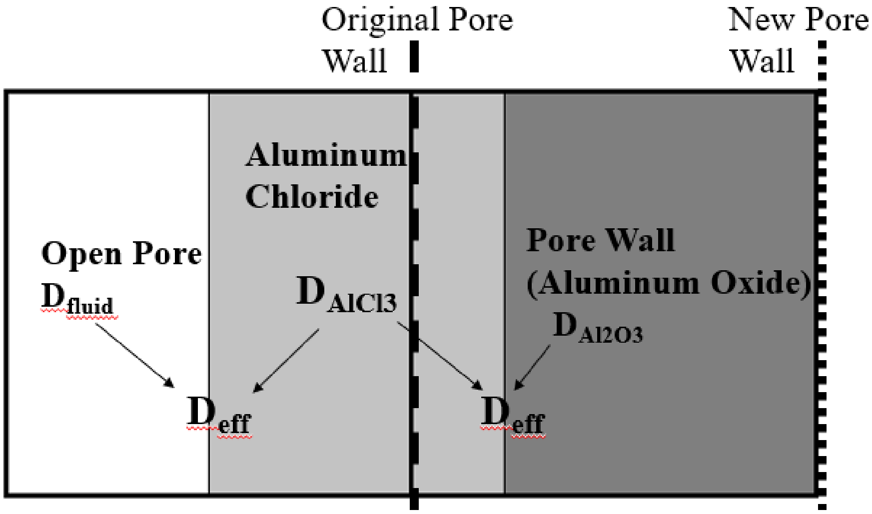

Figure 4.3: Schematic of the dynamic filling of cells from open pore (fluid) to $AlCl_3$ and pore wall to $AlCl_3$.

$$\frac{1}{D_{eff}} = \frac{\varepsilon_{fluid}}{D_{fluid}} + \frac{\varepsilon_{AlCl3}}{D_{AlCl3}} \tag{4.4}$$

where D_{AlCl3} is the diffusion coefficient of HCl in solid aluminum chloride. ε_{fluid} and ε_{AlCl3} denote volume fractions of fluid and solid aluminum chloride in the cell, respectively. Likewise, in the region originally occupied by alumina, as aluminum chloride replaces alumina, the effective diffusion coefficient of mixed cells may be calculated using:

$$\frac{1}{D_{eff}} = \frac{\varepsilon_{Al2O3}}{D_{Al2O3}} + \frac{\varepsilon_{AlCl3}}{D_{AlCl3}} \qquad (4.5)$$

where ε_{Al2O3} is the volume fraction of alumina. Equations (4.4) and (4.5) are formulated by assuming that diffusion resistances act in series.

The inputs to the pore model are the three diffusion coefficients, namely D_{fluid}, D_{Al2O3}, and D_{AlCl3}, as well as the reaction rate constant, k_{pore}. Although it is logical to use a value of D_{fluid} that is equal to the diffusion coefficient of HCl in air, experimental evidence has shown that these pores are often filled (partially or fully) with liquid water resulting from capillary condensation of the moisture in the ambient air. Studies using anodized nanochannels and other nanochannels have observed capillary condensation in pores between 10 and 60 nm [73, 74]. Thus, a value of $D_{fluid} = 3.3 \times 10^{-9}$ m^2/s is chosen, which is considerably smaller than the diffusion coefficient of HCl in air. Values for chlorine diffusion in water reported in the literature are consistent with this value [75]. Experiments to determine D_{Al2O3} are practically difficult since HCl invariably reacts with alumina as it transports through it. In the end, what one ends up measuring is a diffusion coefficient that represents HCl diffusion through a mixture of alumina and aluminum chloride. In view of this difficulty, a decision was made to calibrate D_{AlCl3} (assumed equal to D_{Al2O3}) and k_{pore} simultaneously against experimentally measured HCl uptake data.

4.2 Pore-Scale Model and Results

There are numerous studies that produce anodized oxide pores for various purposes (humidity sensors, pressure sensitive paint, nanoscale research) [44 - 47]. To help determine the average pore radius and porosity of the oxide layer, the acid bath preparation parameters used to create the anodized samples in this study were compared to the preparation in these studies, shown in Table 4.2. It can be estimated that the pore radius is between 15 and 30 nm. A radius of 25 nm gave the best fit to the experimental data. These studies also give a porosity between 0.05 and 0.15, with 0.13 giving the best fit.

Table 4.2: Acid bath preparation for anodized samples.

Acid	Sulfuric Acid (15-18% by weight)
Voltage	14-18 volts
Current Density	10-16 amps per square foot
Time in Acid Bath	30 minutes

Figure 4.4 shows the effect of changing the pore radius on the model results, while Fig. 4.5 shows the effect of changing the porosity, effectively the number of pores, in the oxide layer. Decreasing the pore radius increases the uptake rate at first, due to there being more pores and, hence, more surface area at constant porosity. However, the pore closes up faster due to less area to clog and hence the uptake levels off at a lower level. Increased porosity increases uptake proportionally since porosity is directly proportional to the number of pores at constant pore radius.

The diffusion of gaseous HCl through air is well known. Gaseous diffusion coefficients, in general, are on the order of 10^{-5} m^2/s, or in the case of HCl through air at room temperature, 1.55×10^{-5} m^2/s [76, 77]. Using an open pore diffusion coefficient (D_{fluid}) value did not produce accurate results. As discussed earlier, it is possible that due to the humidity in the air, capillary condensation could create liquid water in the oxide layer. Furthermore, an average pore radius of 25 nm (diameter of 50 nm) is close to the mean free path of air at room temperature (68 nm), meaning that the molecules begin to hit the walls of the pore more than themselves. Continuum assumption begins to break down when the characteristic length is below the mean free path. Added friction of the particles hitting the wall is often accounted for by a decrease in the diffusion

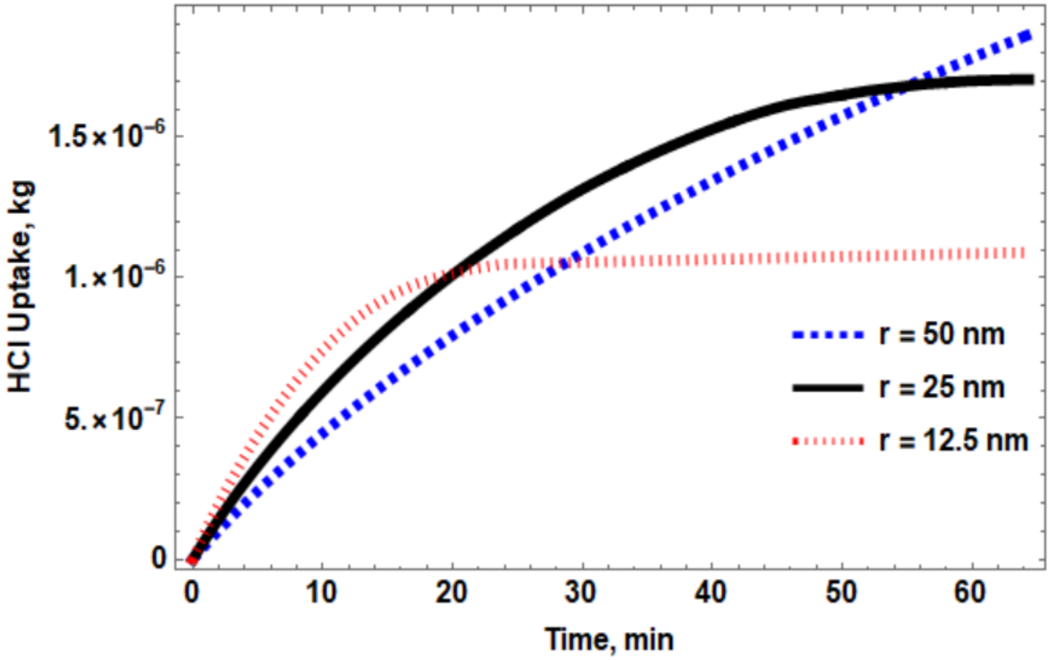

Figure 4.4: The effect of pore radius on HCl uptake.

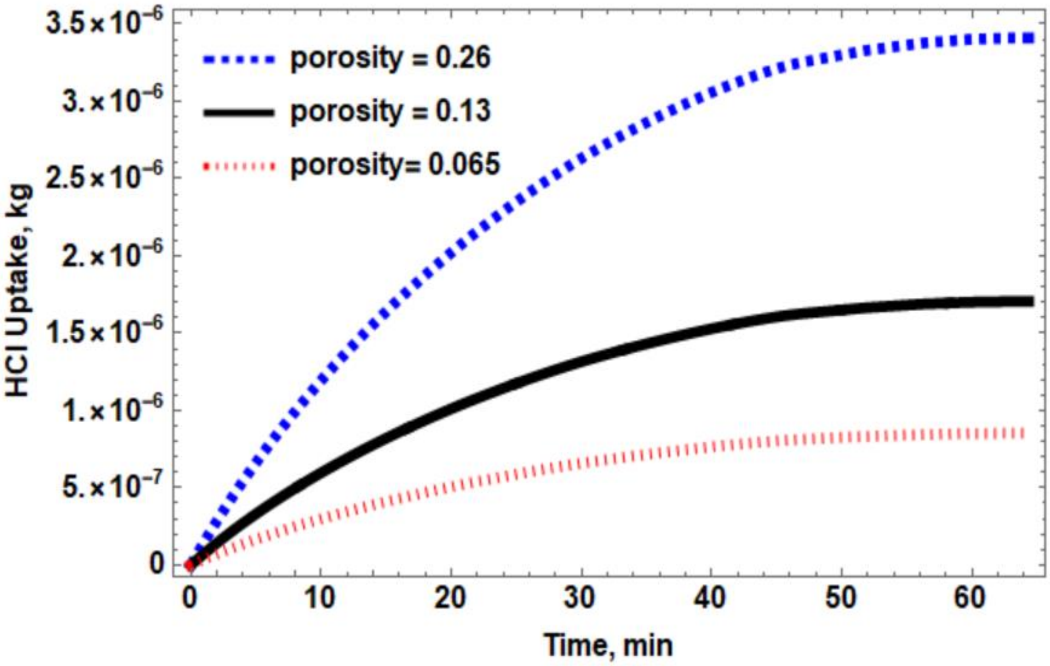

Figure 4.5: The effect of oxide layer porosity on HCl uptake.

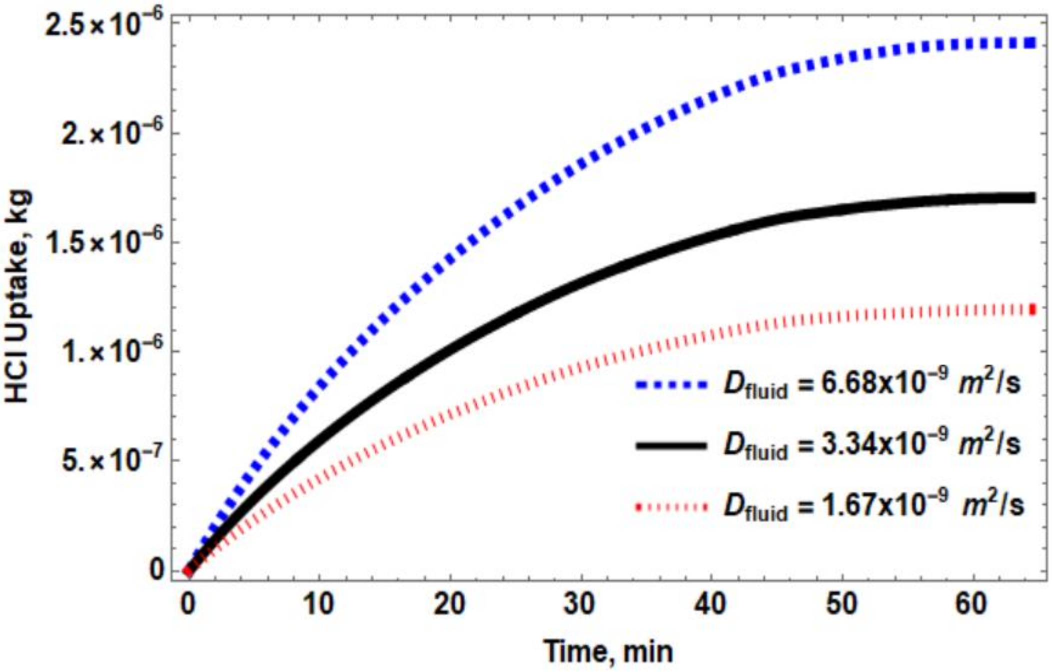

Figure 4.6: The effect of the diffusion through the fluid of the pore on HCl uptake.

coefficient [70]. Hence, a value of 3.3 x10^{-9} m^2/s was chosen for D_{fluid}. This provides a better prediction for both the transient uptake curve and the depth at which chlorine is found. Figure 4.6 shows the effect of changing D_{fluid} on the model. The result is similar to that of adjusting the porosity, where increase in D_{fluid} proportionally resulted in more HCl uptake. Calibrating the model against the experimental data yielded a k_{pore} of 4x10^{-4} m/s and a D_{AlCl3} of 3x10^{-12} m^2/s. To put these values in context, the diffusion coefficient of chlorine through concrete, a porous solid, has been found to be between 10^{-12} and 10^{-14} m^2/s, depending on conditions such as humidity [78]. Figure 4.7 shows the best fit obtained, while Table 4.3 reports the full set of inputs used to obtain this fit. Overall, the model predicts uptake quite well in both time to saturation and total uptake. There are some slight differences in curvature between the model and the experimental case. The uptake for the experimental case increases more linearly and then rounds off fast as it saturates, where the model has a more rounded curve throughout. This can be seen in other cases: Fig. 4.8 and Fig. 4.9 show the effect of changing k_{pore} and D_{AlCl3}, respectively.

Table 4.3: Optimal parameters used in the pore-scale model.

Diffusion coefficient of HCl in aluminum chloride, D_{AlCl3} (= D_{Al2O3}) (calibrated)	3x10^{-12} m^2/s
Diffusion coefficient of HCl in open pore, D_{fluid}	3.3x10^{-9} m^2/s
Reaction rate constant at pore wall, k_{pore} (calibrated)	4x10^{-4} m/s
Pore radius	25 nm
Global porosity of oxide layer	0.13
HCl concentration at the inlet	43.1 ppm

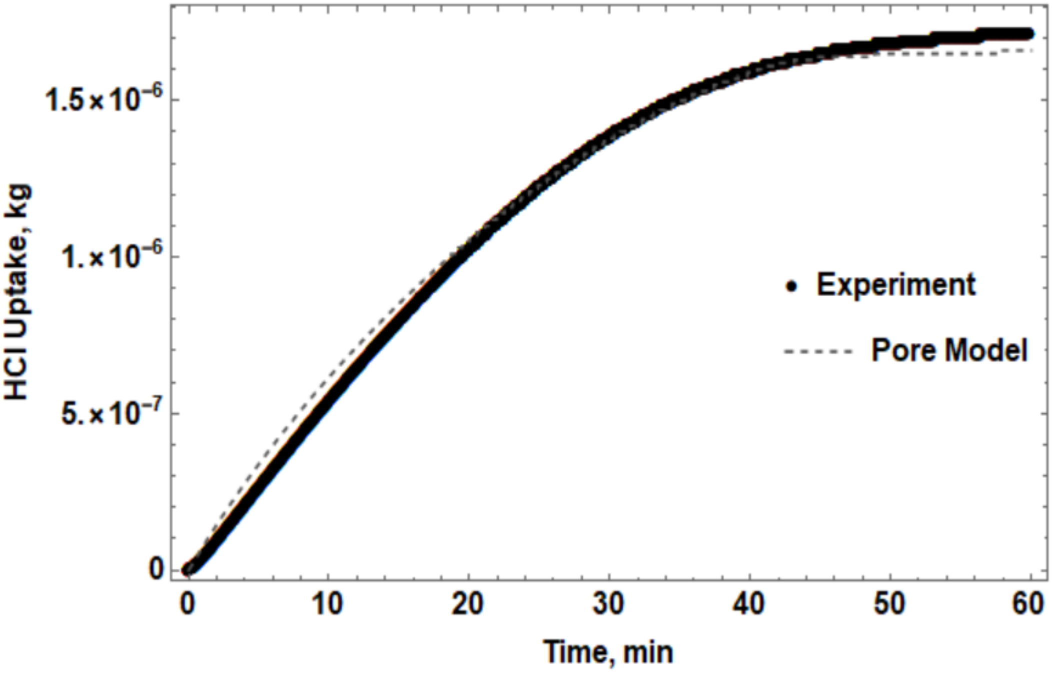

Figure 4.7: Optimal fit of the pore-scale model to measured HCl uptake in an anodize aluminum sample with an inlet HCl concentration of 43.1 ppm.

Figure 4.10 shows the temporal evolution of the material interfaces due to build-up on both sides of the original pore wall. While significant change in the interface positions is noted between 15 and 30 minutes, hardly any change is noted between 45 and 60 minutes. This corresponds to a sharp decrease in uptake rate which can be seen in Fig. 4.7. This indicates that the mass transport resistance through the aluminum chloride layer is so large that the HCl cannot diffuse through it to the back interface and react with the remaining aluminum oxide. It is also to be noted that the interfaces on the two sides of the original pore wall are not symmetric. This is because on the side facing the open pore, when cells are partially filled with aluminum chloride, the HCl must diffuse partly through the fluid and partly through the solid aluminum chloride. In contrast, at the back end, it diffuses through either alumina or aluminum chloride—both of which are solid and have

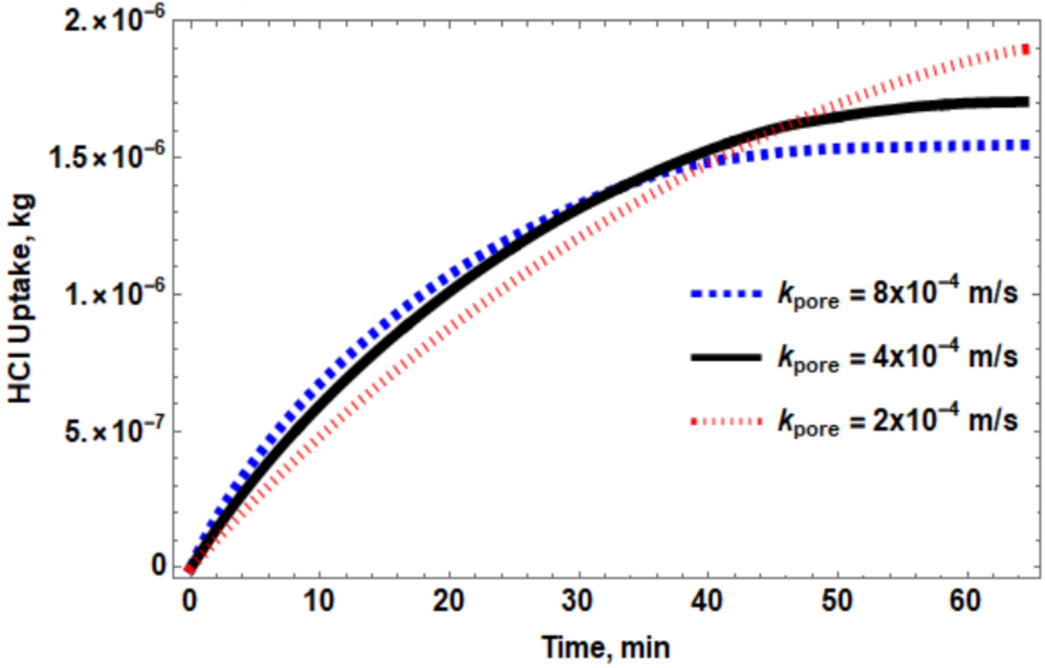

Figure 4.8: The effect of the reaction rate on HCl uptake.

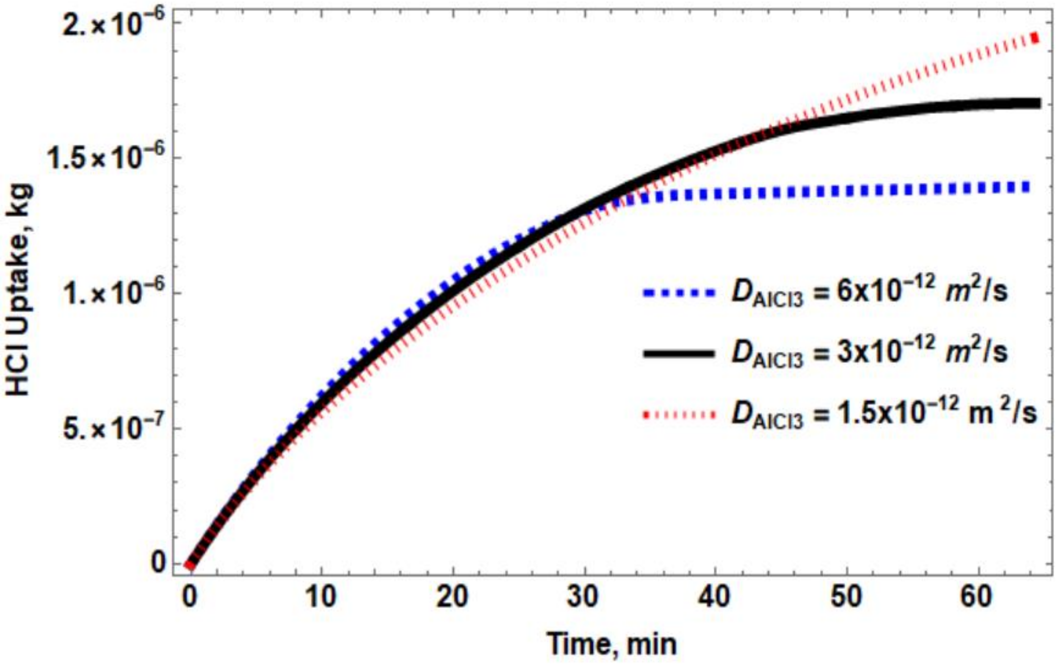

Figure 4.9: The effect of diffusion coefficient through aluminum chloride on HCl uptake.

low diffusivity, as reported in Table 4.3. Finally, the depth at which $AlCl_3$ deposition is predicted is approximately 2,000 nm from the top, which agrees quite well with the depth of 2,200 nm at which chlorine was found in XPS measurements (Table 4.1). It is difficult to compare quantitatively the results from XPS and the model, but qualitative comparisons can be made. XPS collects electron population spectra of every element in the mixture. The data analysis for chlorine is relative to other elements, with aluminum and oxygen being the most prevalent. Figure 4.11 shows the XPS results for chlorine on an anodized aluminum surface after saturation in HCl. A sharp decrease from 0 to 100 nm from the surface is observed followed by no detection after 2,200 nm. Figure 4.10 shows a similar trend in the model at the saturation point, where a sharp drop is noticed nearly immediately, and little to no chlorine deposit is observed past 2,000 nm.

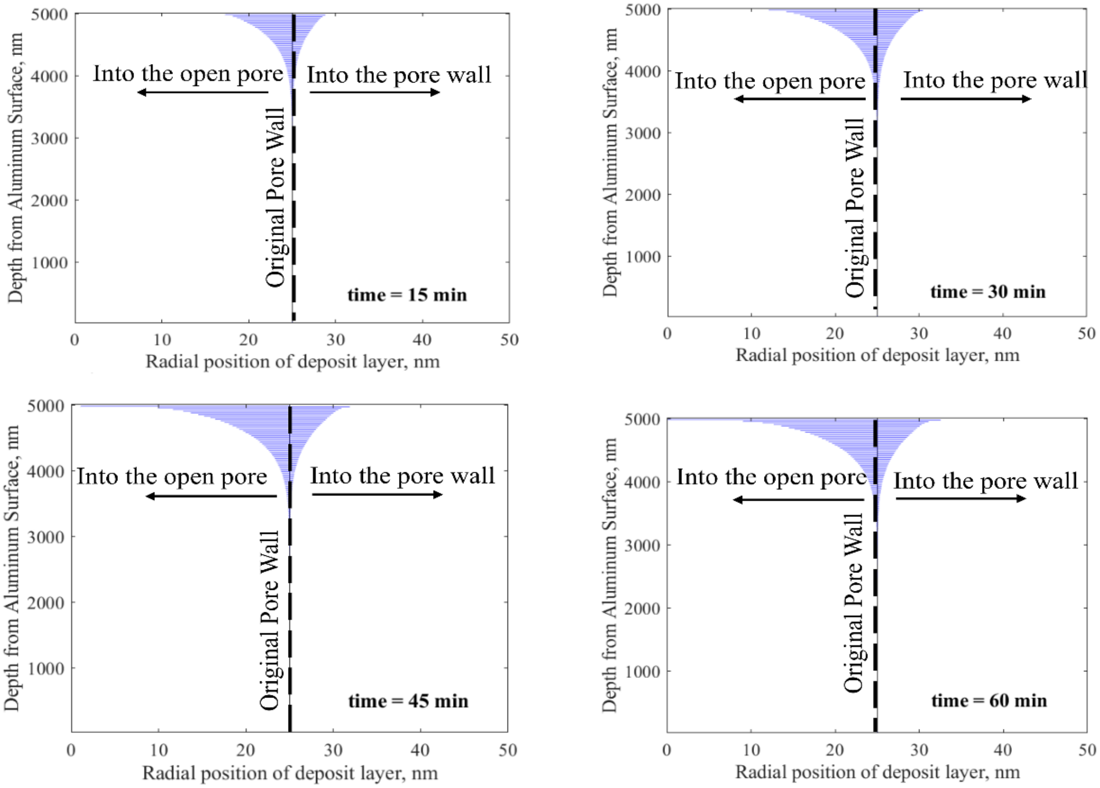

Figure 4.10: Temporal evolution of material interfaces (fluid/alumina/aluminum chloride) predicted by the pore-scale model. Note that the radial direction has been amplified significantly for visual clarity.

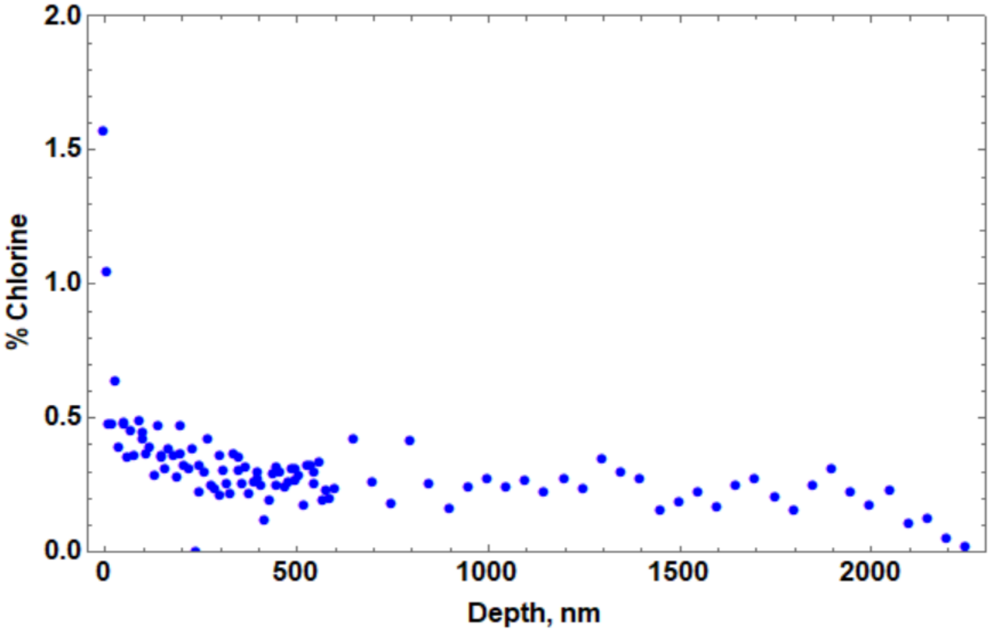

Figure 4.11: XPS data on a saturated anodized aluminum sampling providing the elemental percent that chlorine is found as a function of depth into the oxide layer.

The model just presented simplifies many complex physiochemical processes involved in HCl transport and reaction with an aluminum surface. It is highly likely that the radius of each pore differs slightly, which could place some pores below the radius for continuum transport, or above the radius where there is capillary condensation. This would mean treating a subset of pores in a different manner. Imaging techniques such as SEM could provide an estimate of the pore radius distribution. If there is water in the pore, dissolution of HCl, ion transport, and other solution mechanisms would play a role in transport. Water could just be adsorbed as a gas, creating hydroxyl groups with different adsorption and reaction properties. These, and other ideas, could be explored in future revisions of the model. Overall, the pore model in its current form gives a good engineering estimate of HCl uptake despite the simplifications.

4.3 Multiscale Model Development

As discussed earlier, the single (reactor)-scale model does not account for the build-up of the aluminum chloride layer within the pores of the oxide layer and the additional mass transport resistance caused by this build-up. The pore model, on the other hand, captures this effect. In order to couple the pore-scale to the reactor-scale, the average (over the area where build-up occurs) mass transport resistance was extracted from the pore-scale calculations as a function of time. This was done for an inlet (pore mouth) concentration of 43.1 ppm HCl, and the results are shown in Fig. 4.12. The diffusion resistance shown in Fig. 4.12 is equal to A_{eff}/D_{eff}, where A_{eff} is the surface area of each pore over which buildup occurs times the number of pores per unit area of the sample surface. The number of pores is easily estimated from the global porosity, reported in Table 4.3, and the dimensions of each pore. The diffusion resistance is not smooth because the reaction front jumps from one cell face to another cell face (since a fixed grid is used) with time, rather than moving smoothly across cells. To incorporate this diffusion resistance into the reactor-scale model, it was first curve-fitted, as also shown in Fig. 4.12, and the resulting equation was used. As to exactly how the fitting was performed, is described shortly.

Once the curve-fit expression is obtained, a reactor-scale diffusion coefficient, D_{rs}, can be computed by dividing the curve-fitted resistance by the local area of the sample. The reactor-scale diffusion coefficient, which essentially captures the effect of additional mass transport resistance posed by pore-scale diffusion, is used only within control volumes (or cells) in the reactor model that are adjacent to the sample surface (or surface reaction boundary conditions), shown in Fig. 4.13. Figure 4.13 is the same as Fig. 3.4 a but shows the boundary conditions instead of the mesh.

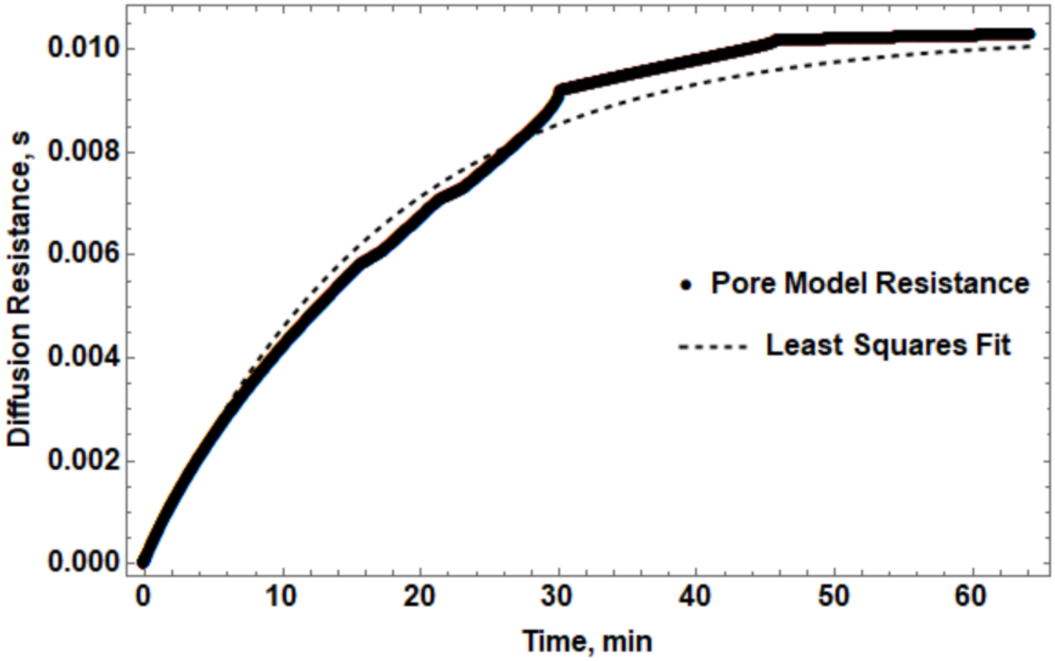

Figure 4.12: Average diffusion resistance computed from the pore-scale model as a function of time, along with a least-squares fit of the data.

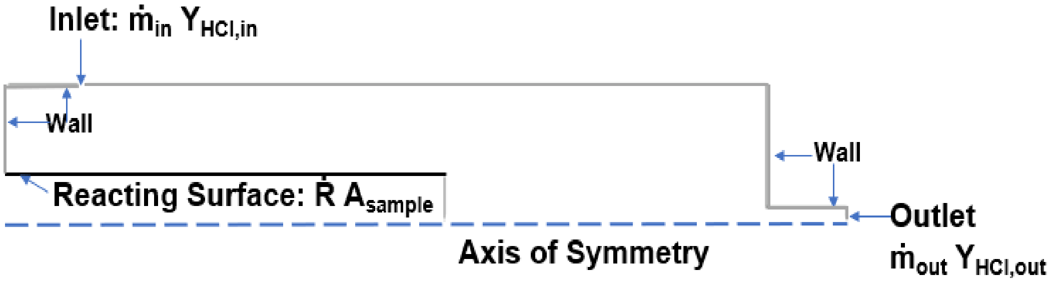

Figure 4.13: Schematic of reactor-scale model.

The curve-fit shown in Fig. 4.12 yielded a reactor-scale diffusion coefficient that decreased exponentially with time:

$$D_{rs} = 1.55\times10^{-5}\exp(-0.0015t)\ \mathrm{m^2/s} \tag{4.6}$$

Although this fit is good, it is not applicable universally. This is because the time scale will change if the reactor is operated under a different set of conditions (e.g., inlet HCl concentration is changed, or the flow speed is changed) and/or if the reactor size/shape is changed. Since the growth of the aluminum chloride layer is related to the reaction rate, and the reaction rate, in turn, is related to the local wall concentration of HCl [Eq. (3.2) or (4.2)], an alternative approach to fitting the diffusion resistance is to use wall concentration rather than time as the independent variable. Such a curve-fit, being dependent on wall concentration, will be applicable to any reactor condition since the local wall concentration will be the only variable. Such a concentration-dependent curve-fit was obtained, and is written as:

$$D_{rs} = 1.55\times10^{-5}\exp\left[-14\left(\int_0^t c_w\,dt'\right)^{0.45}\right]\ \mathrm{m^2/s} \tag{4.7}$$

A comparison of the curve-fits obtained using Eq. (4.6) and Eq. (4.7) is shown in Fig. 4.14. Both fits start and end at the same diffusion coefficient values, with some differences at intermediate times. In the section to follow, the multiscale reactor model is exercised for a few different operating conditions and sample types and the findings are reported.

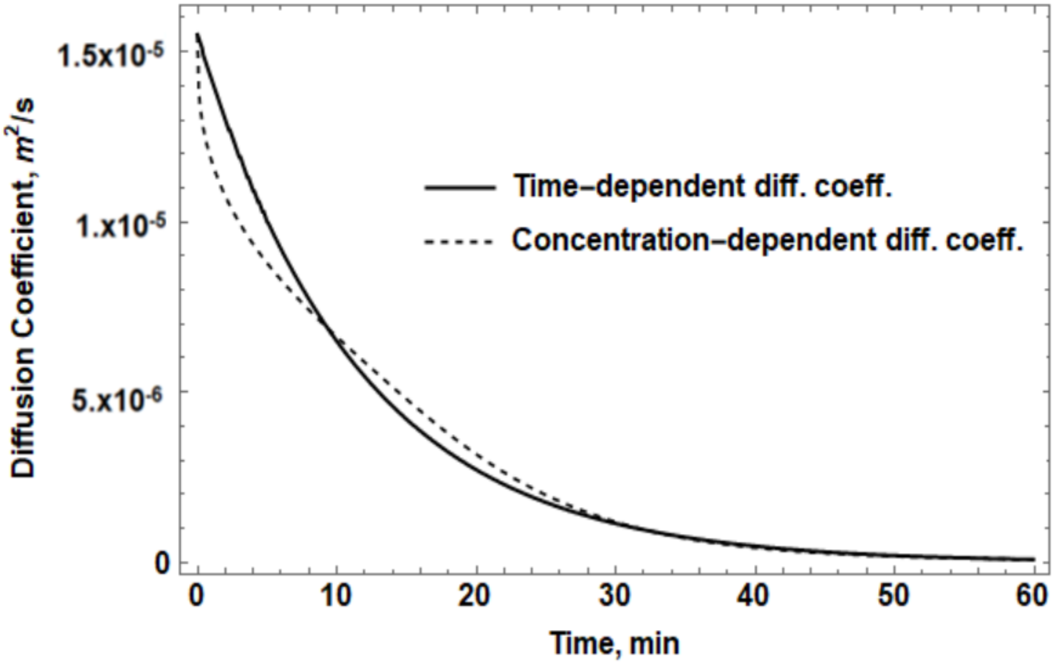

Figure 4.14: Reactor-scale diffusion coefficient, D_{rs}, obtained by curve fitting the diffusion resistance obtained from pore-scale calculations.

.

4.4 Results from Multiscale Model

The first case considered for testing of the new multiscale reactor model is the same one that motivated this study and is shown in Fig. 3.9. As evident in Fig. 3.9, the single (reactor)-scale model yields poor agreement for anodized aluminum. To quantify the match with experimental data, SSE were computed, and were found to be 4.63, 2.92, and 12.87 percent for stock, CCC, and anodized aluminum samples, respectively. The physical conditions for this study are described in Section 2.1 and Section 3.1, and a schematic of the reactor that was modeled is shown in Fig. 4.13.

The inlet HCl concentration is 43.1 ppm. The computations were repeated with the new multiscale model. Both time-dependent [Eq. (4.6)] and concentration-dependent [Eq. (4.7)] were tested. Figure 4.15 shows a comparison between results obtained using the original single (reactor)-scale model and the two multiscale models. The SSE were again computed, and found to be 12.87, 6.64, and 6.77 percent for the single (reactor)-scale model, for the multiscale model with time-dependent diffusion coefficient, and the multiscale model with concentration-dependent diffusion coefficient, respectively. Clearly, the multiscale model yields superior results compared to the original single (reactor)-scale model, indicating that capturing transport and reaction within the pores of the oxide layer is critical to predicting HCl uptake by anodized aluminum. The fact that the two diffusion coefficient models yield similar accuracy is not surprising considering the closeness of the two fits shown in Fig. 4.14.

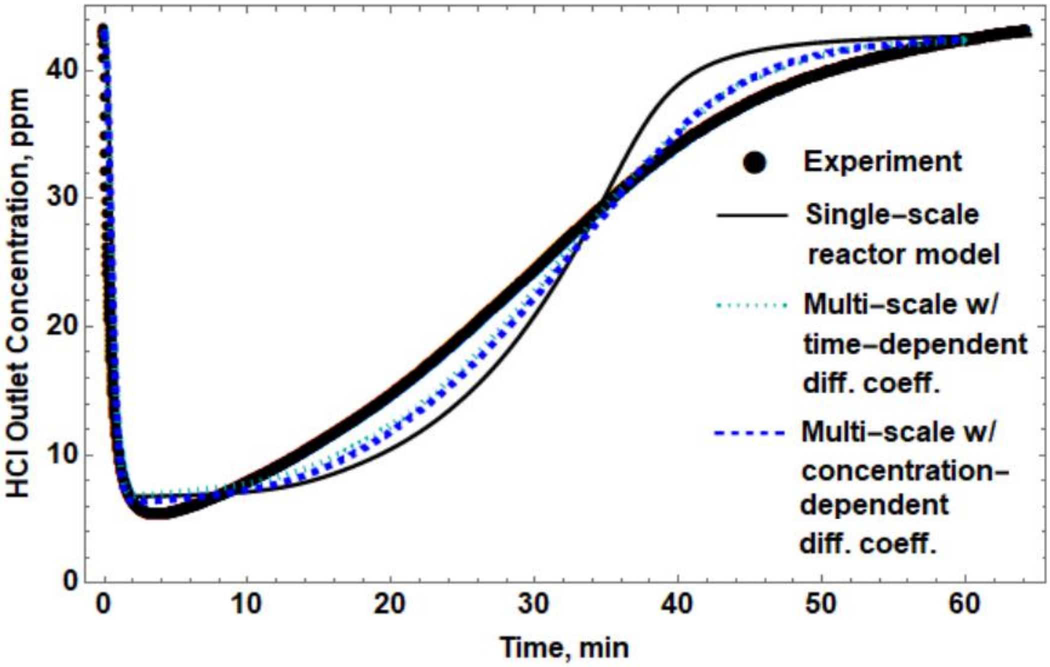

Figure 4.15: Comparison of results obtained using the single (reactor)-scale model and the two multiscale reactor models for inlet HCl concentration of 43.1 ppm.

As stated earlier, the perceived advantage of using the concentration-dependent diffusion coefficient fit is that it is applicable to any reactor operating condition. To test this hypothesis, the multiscale model was exercised for a different reactor condition in which the inlet concentration of HCl is 16.8 ppm. In other words, the model was exercised for a condition that had no relationship to the dataset used for calibration of the model. Figure 4.16 shows the results obtained with the single (reactor)-scale and multiscale (with concentration-dependent diffusion coefficient) reactor models. Since the inlet concentration is much lower in this case, it takes more time (compared to the 43.1-ppm inlet case) for the sample to saturate and reactions to stop. In this case, the time-dependent diffusion coefficient expression is not even valid since it is fitted to the time interval of a different experiment. However, as evident from Fig. 4.16, the concentration-dependent diffusion coefficient model yields reasonably accurate results. Once again, the results yielded by the multiscale model is superior to the results yielded by the single (reactor)-scale model: the SSE being 7.01 and 15.96 percent with the multiscale and single (reactor)-scale models, respectively. In other words, regardless of operating conditions, the multiscale model reduced the SSE from experiments from 13-16% to 6-7%.

As a final step, the new multiscale model was exercised for stock and CCC aluminum sample types. As shown in Table 4.1, the oxide (alumina) layer thicknesses in stock and CCC sample types are 50 and 200 nm, respectively. Furthermore, micrographs revealed that the pore diameters in these samples are much smaller than anodized aluminum and the pores are more disordered. Hence, a pore radius of 5 nm was used for these samples. Based on the new pore dimensions, the global porosity values were estimated to be 0.03 and 0.05, respectively. The new multiscale model was then used without any other additional adjustments. Figure 4.17 shows a comparison of the

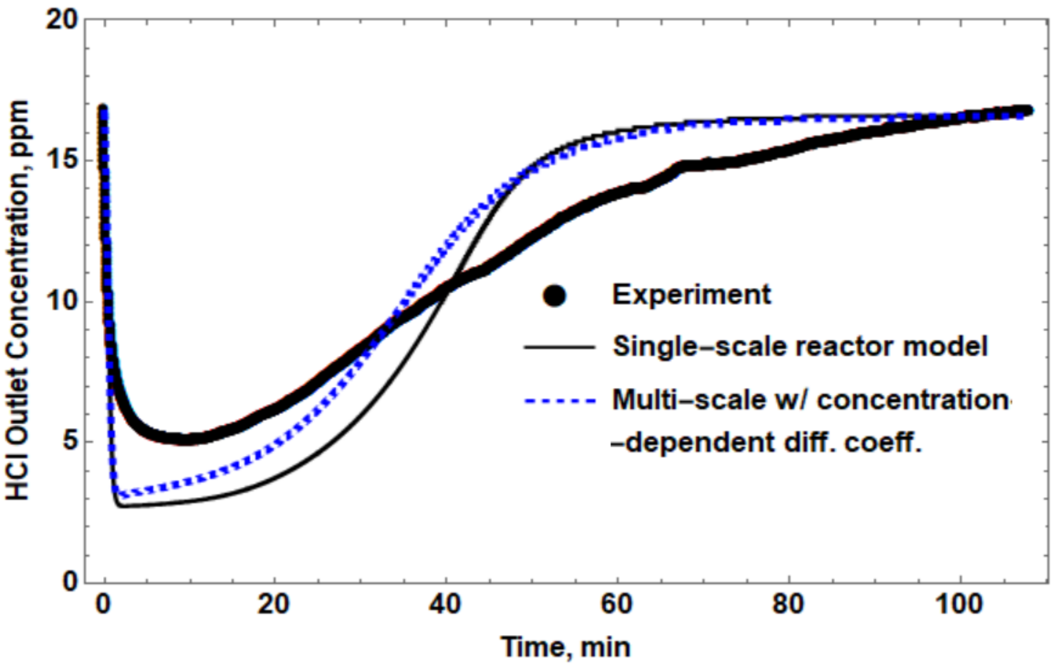

Figure 4.16: Comparison of results obtained using the single (reactor)-scale model and the concentration-dependent diffusion coefficient based multiscale reactor model for inlet HCl concentration of 16.8 ppm.

modeling results against experimental data. Clearly, the agreement is quite good, indicative of the fact that the same multiscale model can be used effectively for all aluminum sample types. Figure 4.18 found that accounting for the pore-scale produced marginal change in the results, which corroborates previous findings discussed in Ch. 3 that a single (reactor)-scale reactor model is adequate for predicting uptake in stock and CCC samples.

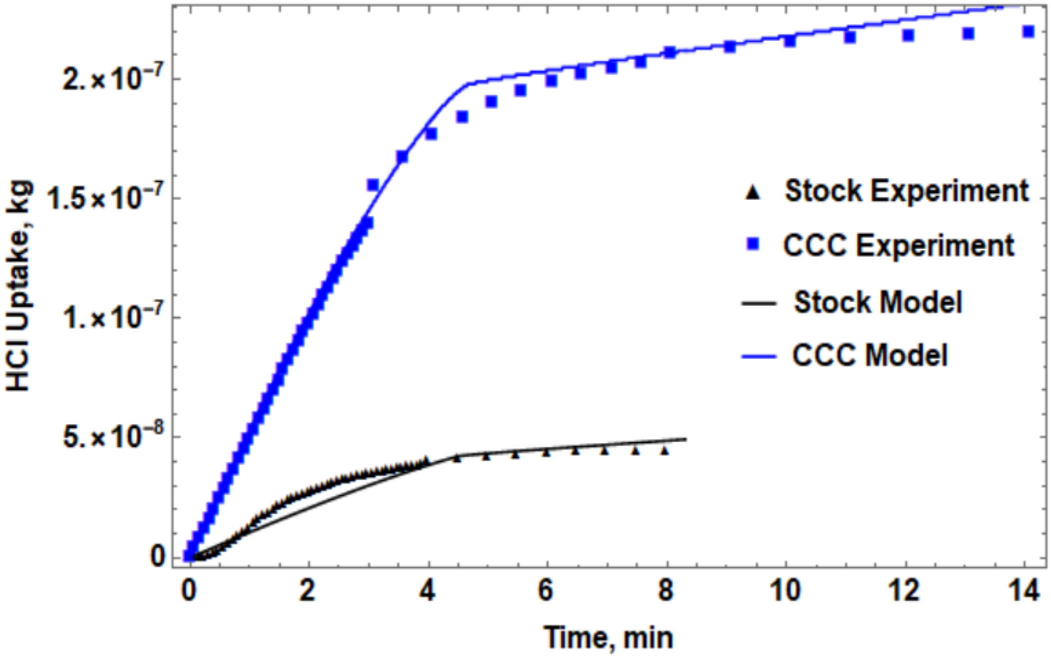

Figure 4.17: Validation of the pore scale model for stock and CCC aluminum sample types for HCl inlet concentration of 43.1 ppm.

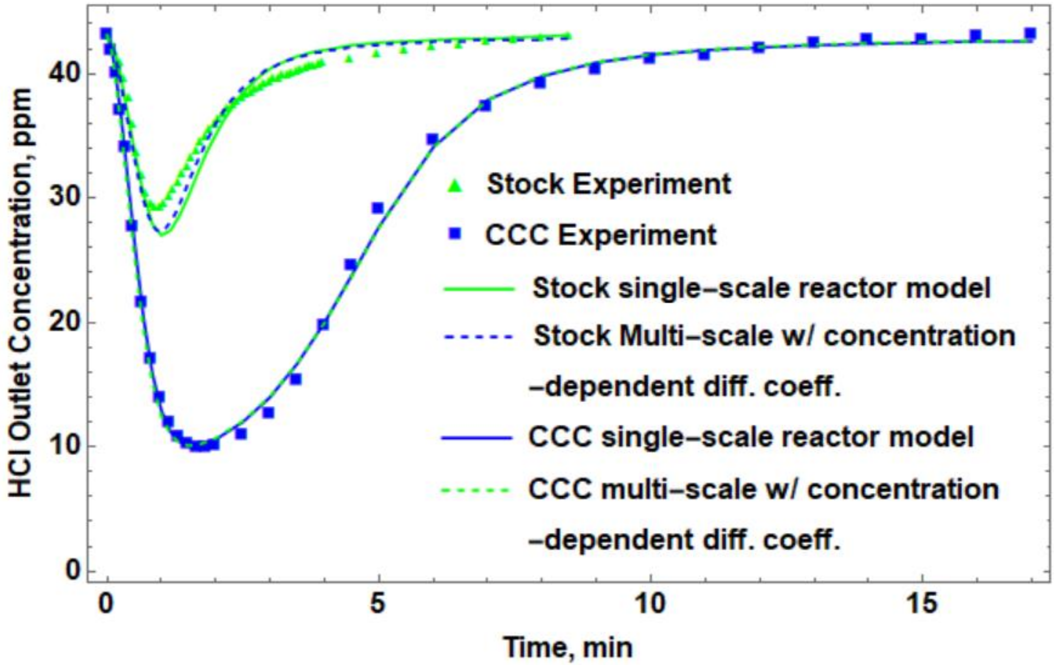

Figure 4.18: Validation of the new multiscale model for stock and CCC aluminum sample types for HCl inlet concentration of 43.1 ppm.

4.5 Summary

Modeling studies described in Ch. 3 revealed that a single (reactor)-scale model, in which HCl reacts on a flat aluminum surface, is incapable of predicting the HCl uptake accurately when anodized aluminum surfaces are considered. Anodized aluminum differs from stock (untreated) or chromate conversion coated (CCC) aluminum in that the oxide (alumina or Al_2O_3) layer is an order of magnitude thicker: ~5,000 nm as opposed to a few hundred nm. In order to capture the effect of this thick alumina layer on the overall uptake of HCl, the oxide layer cannot be neglected, as done in single (reactor)-scale models.

In this chapter, a multiscale model was proposed and tested. First, a single pore within the oxide layer was modeled. The HCl diffused through this pore and reacted with the alumina pore walls to form a layer of aluminum chloride, which clogged the pore and increased the mass transport resistance significantly. Ultimately, this increased mass transport resistance resulted in a shut-down of the reaction between HCl and alumina. The pore-scale model was then coupled to a reactor-scale model using a concentration-dependent reactor-scale diffusion coefficient, and the resulting multiscale model was exercised to predict the uptake in a reactor under various operating conditions. It was found that when compared to the single (reactor)-scale model, the multiscale model reduced the error between model predictions and experiments by approximately a factor of two regardless of the operating conditions used. The same multiscale model was also tested for stock and CCC samples (where the oxide layer thickness is insignificant), and yielded good agreement with experimental data, as well, indicating that the same multiscale model is accurate for the prediction of uptake of HCl across all aluminum sample types.

Chapter 5: EFFECT OF WATER VAPOR ON THE UPTAKE OF HCl

Previous experiments in this work showed HCl uptake by aluminum and other surfaces without the presence of water vapor. Although the samples were exposed to moisture prior to inserting them in the reactor, the HCl flow stream was completely dry. The atmosphere of a spacecraft, similar to most terrestrial habitats have a relative humidity (RH) between 40 and 60% at room temperature (20 °C). In this chapter, experiments that were performed to determine the interaction of gaseous HCl with various aluminum surfaces in the presence of water vapor are reported, i. e., the samples are now exposed to a mixture of HCl, water vapor and air, as opposed to just HCl and air. The repeatability of such experiments is discussed, as well as practical water-based cleanup techniques. A model is then proposed to predict the uptake of HCl in the presence of water vapor.

5.1 Experiments to Study Effect of Humidity on Anodized Aluminum

As discussed in Ch. 3, aluminum has been found to uptake HCl in dry air flow. The environment of a typical spacecraft will have RH levels between 40 to 60% [7 - 10], similar to many terrestrial habitats. Given the presence of humidity in all spacecraft, it is imperative to understand how water vapor in the flow stream affects the uptake of HCl with aluminum surfaces.

Water vapor from the atmosphere can affect the structure and, hence, reactivity of alumina. Schuttlefield et al. [31] have shown that alumina can uptake a monolayer of water at 50% RH, and about 2.5 monolayers at 80% RH within the oxide layer. Peri and Hannan [35] described water adsorption on alumina as non-dissociative chemisorption through very strong hydrogen bonds between surface oxide groups and water. Bailey [60] performed a study with alpha and gamma alumina where he found that increased outgas temperature of the alumina (decrease in pre-adsorbed water) increased hydrogen chloride adsorption. This trend seems to indicate that water vapor and HCl compete for adsorption sites on the alumina. Water vapor has also been noted to increase the capacity to uptake HCl by other materials, such as PMMA, gypsum, cement, and nylon filters [22 - 24].

This study used the reactor shown in Fig. 2.6 with the bubbler to add water vapor to the flow. The first series of tests presented in this chapter add humidity in the flow to observe the effect it has on the uptake of HCl. Additional tests subjected saturated aluminum samples to water (both vapor and liquid) and subsequent HCl flow tests were performed. This was to guide both post-fire cleanup techniques, as well as to determine if water could be used to regenerate sites or uptake capacity in order to reuse the same sample. Table 5.1 gives a summary of the experiments performed in this chapter with anodized aluminum. All tests reported in this chapter are done at room temperature 20 ℃.

5.1.1 Humidity Variation

Outlet HCl concentration measurements, normalized by the initial outlet concentration of the test, as a function of time are plotted for various levels of water vapor (RH) in the inlet gas stream in Figure 5.1. As a reminder, the uptake is the area bounded by the horizontal line of the inlet concentration and the curve presented. There is a positive correlation between HCl uptake and the RH of the gas stream. This implies the water vapor enhances either the reaction rate of the adsorbed

Table 5.1: Summary of tests conducted to study the effect of humidity on anodized aluminum.

Test Description	First Round Test	In-between Tests	Second Round Test	Result
Humidity Variation	HCl + Humid air	-	-	HCl uptake increased with humidity in the flow
Dry Air Repeats	Dry HCl	Left in test cell for 24 hours under quiescent conditions	Dry HCl	Second sample HCl uptake was on average 26.3% of the original test
Humid Recovery	Dry HCl	Flowed 1000 ccm of 90% humid air over sample for 24 hours and dried for 48 hours	Dry HCl	Second sample HCl uptake was on average 35.6% of the original test HCl uptake
Water Recovery	Dry HCl	Placed in distilled water for 24 hours, taken out and dried for 48 hours	Dry HCl	Second sample HCl uptake was on average 82.2% of the original test HCl uptake
Humid Test after Dry Saturation	Dry air	Left in test cell for 24 hours under quiescent conditions	50% humid air	Repeated sample never saturated
Humid Test following a Humid Test	50% humid air	Left in test cell for 24 hours under quiescent conditions	50% humid air	Original and repeated sample never saturated, and gave identical outputs
Dry Test following a Humid Test	50% humid air	Left in test cell for 24 hours under quiescent conditions	Dry air	Second sample HCl uptake was 2.4% of the original test HCl uptake

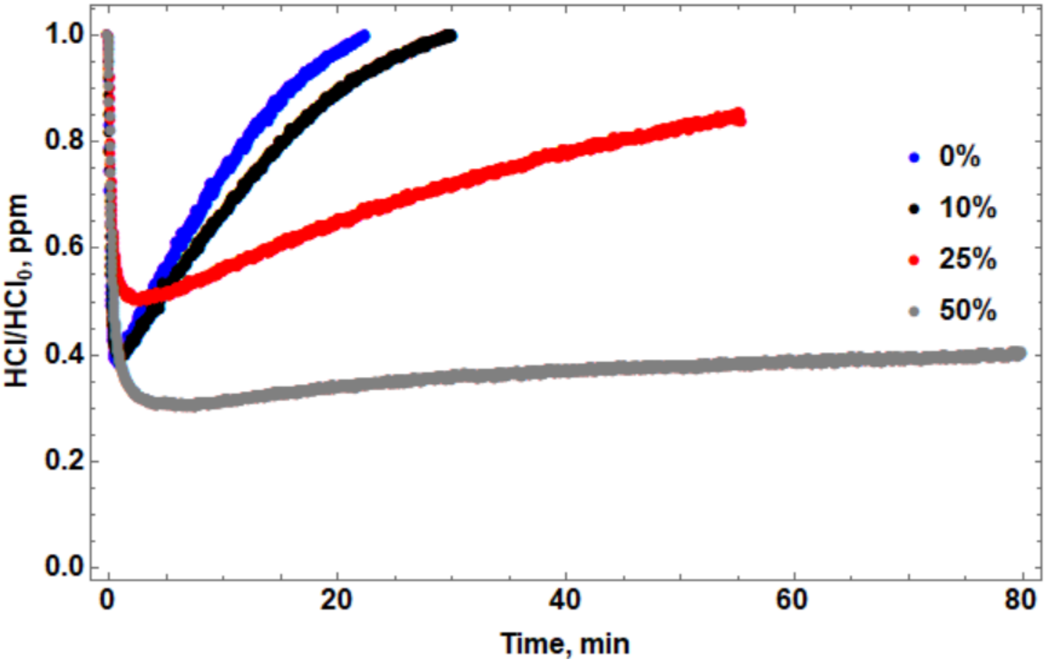

Figure 5.1: Time histories of normalized HCl outlet sensor for HCl-anodized aluminum interaction as a function different RHs in the flow. All saturate except the 50% RH case.

HCl with the oxide layer, or the transport of HCl into the oxide layer. Starting with the 50% RH case, the sample does not saturate within a reasonable time frame. Given the slight upward trend, it is possible the 50% RH case does eventually saturate, but the bottle of HCl runs out before this can be confirmed. The 0% RH (dry air) had a saturation of 2,671 μmol/m^2, while the 10% had a saturation of 2702 μmol/m^2. These values are nearly identical and almost within the uncertainty of 22 μmole/m^2 calculated in Ch. 3. A much larger difference in the behavior is realized once the RH reaches 25%, which uptakes 3,840 μmole/m^2 of HCl. The physical implications of these trends are discussed in Section 5.3 after the entire set of data have been presented.

5.1.2 Dry Tests with No Intervention In Between

Subsequent tests were performed on the same anodized aluminum sample to examine the recovery of the uptake capacity. Figure 5.2 shows a case where the first sample was tested with dry HCl flow and repeated the next day under the same conditions. The only treatment of the sample between tests was the approximately 20 minutes of 1,000 ccm dry air flow into the test cell after the first test to purge out the test cell and the lines of HCl. After the HCl was cleared out of the apparatus, the flow was shut off and the sample stayed in the quiescent test cell until next day's tests. The sample could now only uptake 26.3% of the HCl of the original test (3,105 μmol/m^2 vs 816 μmol/m^2). A test that flowed 500 ccm of dry air over the sample in between the pair of tests was attempted with no noticeable difference.

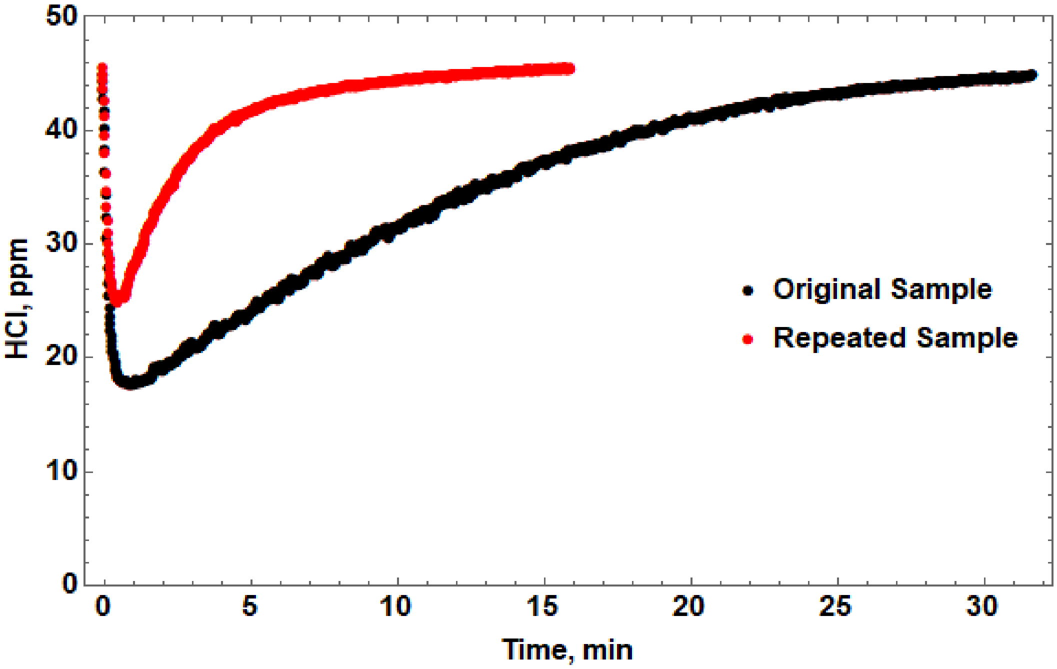

Figure 5.2: Effect of repeating dry air flow over sample on HCl uptake.

5.1.3 Dry Tests with Humid Flow In Between

A series of tests focused on flowing humid air over the aluminum sample after it had been saturated to determine if it had a cleaning effect (return of uptake capacity to the aluminum sample). This has applicability to large-scale tests and more generally, post-fire clean up. In between these tests, after dry air flow was used to clear the lines of HCl, air at 1,000 ccm and 90% RH was flowed over the sample for 12 hours. An example of this test series is shown in Fig. 5.3. This set of three repeat tests produced (35.6 +/- 1.7) % of the HCl uptake of the original sample. This is more than simply what the dry air can clean, but still does not clean the aluminum surface significantly. A test was also completed with stagnant humid air in-between the two tests. This produced no significant difference.

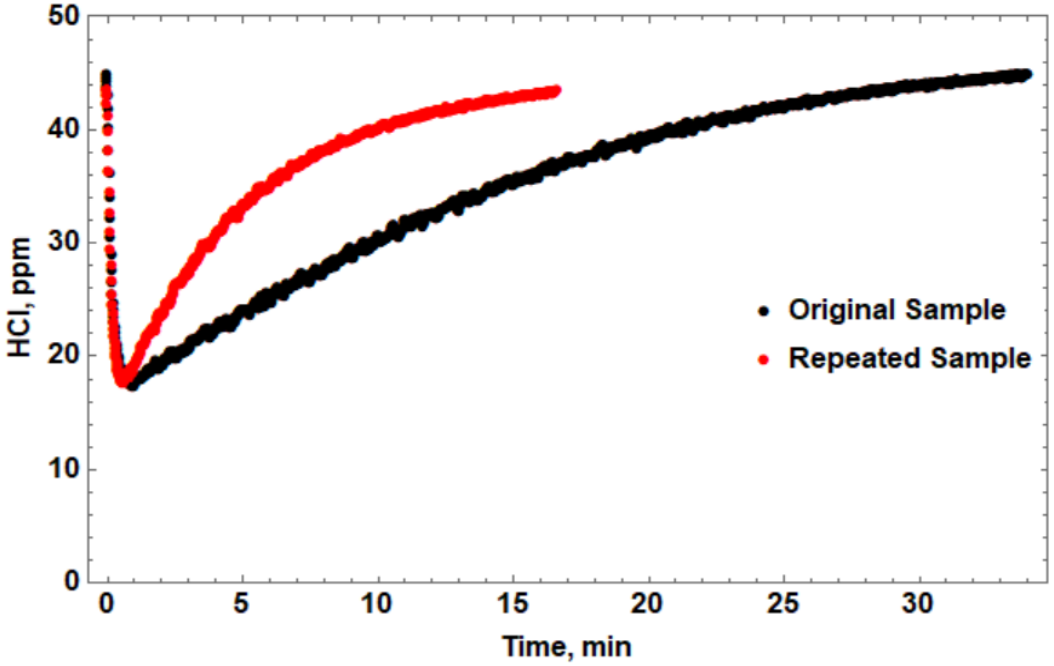

Figure 5.3: Effect of humid flow in between tests on HCl uptake.

5.1.4 Dry Tests with Water Bath In Between

The next set of tests used a distilled water bath to attempt to clean the aluminum sample. After the first saturation test in dry air, the sample was submerged in distilled water for 24 hours. It was then washed off with 500 mL of water and dried with forced air for 1 minute. It was placed back in controlled storage at 50% RH for two days. Figure 5.4 shows an example result from this set. The saturation of this series of tests relative to the original test was (82.2 +/- 4.8) %. This restored the aluminum significantly more than humid air, but still not completely. The test was repeated with the sample submerged in water for five days, but no significant difference in results was achieved. A test was done without the storage step, in which the sample was tested the same day it was taken out of the water. This produced an uptake that was greater than the original (2,780 $\mu mol/m^2$ vs. 3,312 $\mu mol/m^2$ for a 19% increase). This reinforces the role of water in enhancing HCl uptake on aluminum surfaces.

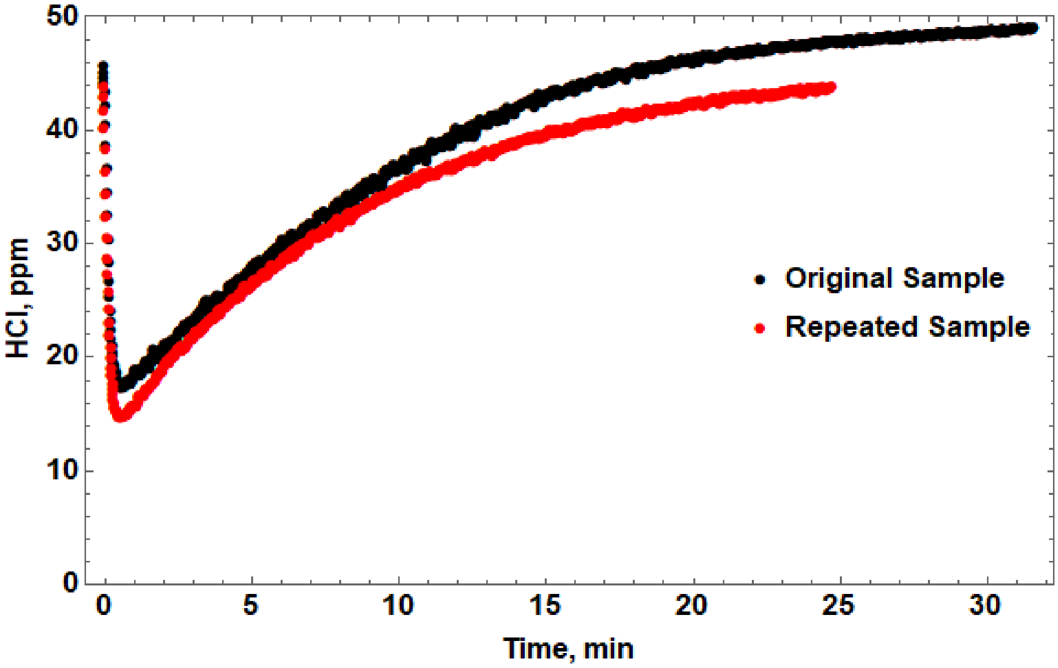

Figure 5.4: Effect of a water bath in between tests on HCl uptake.

Any test that flowed dry air promotes the drying of the aluminum oxide layer without even considering the effect of HCl. In the previous series of tests where a sample was tested after it had been saturated, it is important to know how long it takes for the sample to re-adsorb the lost water from the test, (or in the case of the distilled water bath treatment tests, how long until the sample dries to a level corresponding to 50% RH) so that the effect from HCl can be isolated. Six flat sheets of anodized aluminum with surface area equal to the sample rods (0.0162 m^2) were subjected to a thermal vacuum (120 °C, -755 mmHg gauge) until their weight reached steady state, which was approximately 24 hours. Three of the six samples were then placed in distilled water bath for 24 hours, dried with forced air for 1 minute, and then placed in a controlled 50% RH container while the other three were placed directly in the controlled 50% RH container. No significant changes in weight happened in an hour for either set of samples. After two days, all the samples reached a steady state. The results are shown in Table 5.2. Two conclusions are taken from these results. First, it has been determined that it takes approximately two days to saturate the sample again from vacuum conditions. Due to this result all tests that used a water treatment in an attempt to clean the sample were placed in a 50% RH environment for at least two days before they were used again for testing, in order to return the sample to baseline water saturation. Second, the amount of water within the oxide layer can be estimated. Using the average weight of the water after three days of the six samples and the volume of the oxide layer with the parameters calibrated in Ch. 4 (0.011 mL), the pores can be assumed to be 44.7% filled with water at 50% RH.

Table 5.2: Uptake of water from anodized aluminum. Weight gain is relative to the weight after vacuum.

Sample	Weight after vacuum (μg/cm^2)	Weight gain after submerged in water for 24 hours (μg/cm^2)	Weight gain after 1 hour in 50% RH (μg/cm^2)	Weight gain after 1 day in 50% RH (μg/cm^2)	Weight gain after 2 days in 50% RH (μg/cm^2)	Weight gain after 3 days in 50% RH (μg/cm^2)
1	85,324	65.2		42.1	25.4	25.1
2	84,776	57.4		40.8	22.9	23.4
3	86,160	61.6		48.8	22.1	22.3
4	84,736		1.2	18.6	32.1	31.9
5	84,740		3.9	19.2	33.2	33.2
6	84,966		2.8	15.5	38.7	38.5

5.1.5 Humid Test after Dry Saturation

A humid test (50% RH flow) was performed on a sample that was saturated during a dry air test (0% RH). The same results can be seen for the samples subjected to 50% RH flow and HCl on a fresh sample. Figure 5.5 highlights the response. This suggests that the initial state of the aluminum sample does not have a significant effect relative to the conditions of the environment that the sample is subjected to during interaction with HCl.

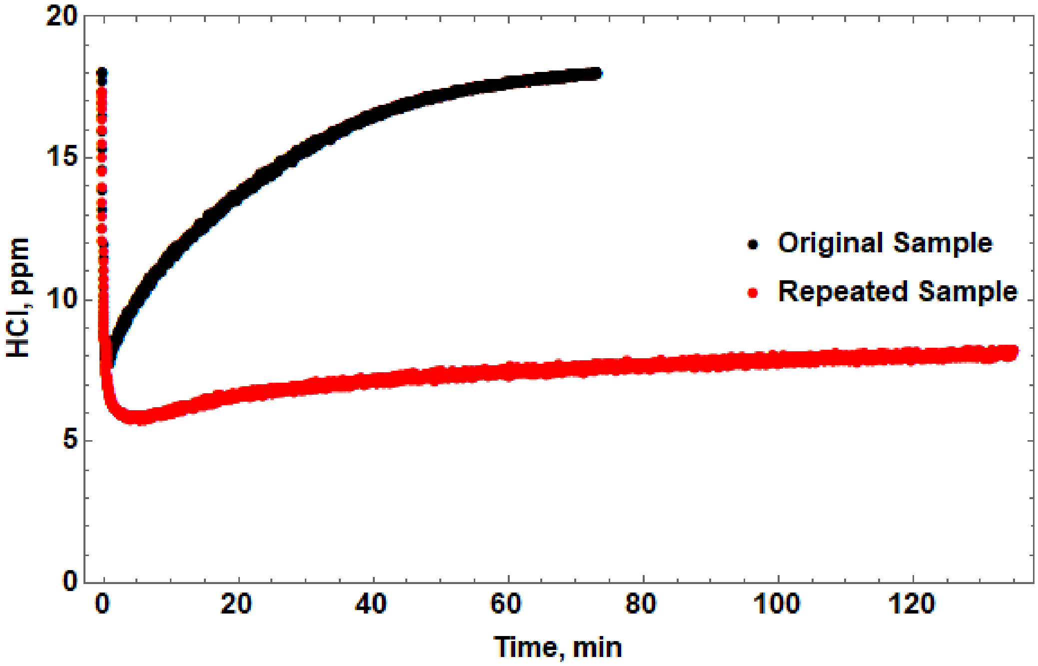

Figure 5.5: Sample subjected to 50% RH flow after it was saturated in a dry air environment.

5.1.6 Humid Test following a Humid Test

Next, tests were repeated on the same sample that was subjected to humid air. No treatment was performed in between tests. The second test of each pair was similar to the first test, as can be seen in Fig. 5.6. The tests were similar even after testing it a third time. This is promising for the large-scale tests since it is more difficult to change out the samples (duct walls), hence any sample that can be reused decreases the difficulty of the test campaign. By the fourth repeat of the sample, the rate of recovery was noticeably higher, yet still a long way away from saturating. The sample was now placed in distilled water bath to attempt to return the sample to its original cleanliness. This ultimately worked for the next two as they mimicked the response as shown in the first series of tests in Fig. 5.6. This can be seen in Fig. 5.7. The last test (2^{nd} repeat after the water bath) has a higher slope at the end, indicating that it is starting to saturate and uptake less HCl.

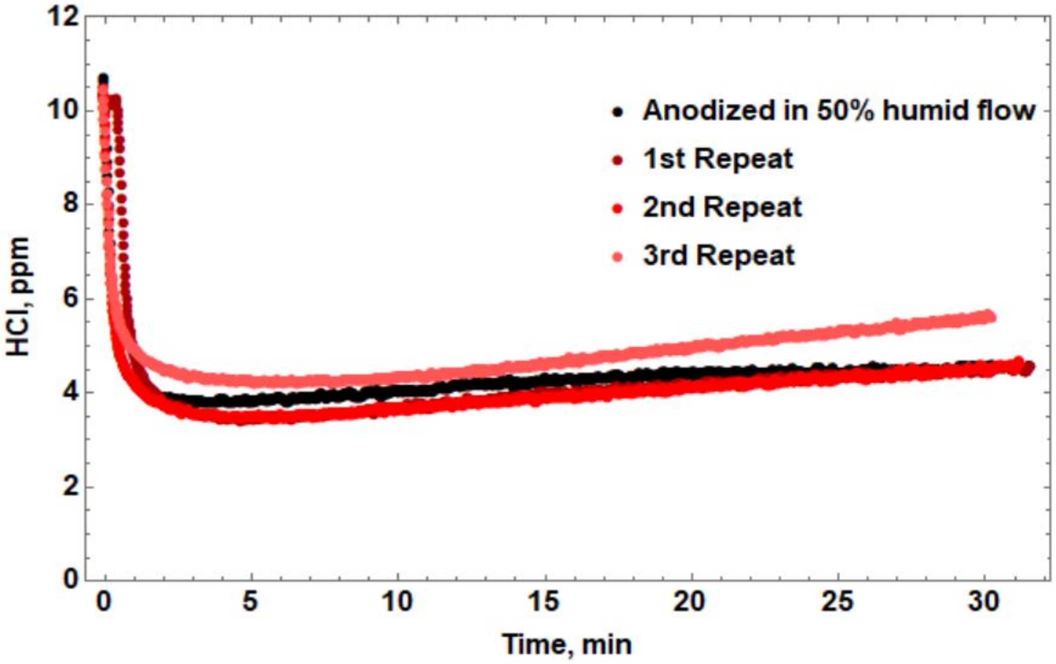

Figure 5.6: Repeated tests at 50% RH.

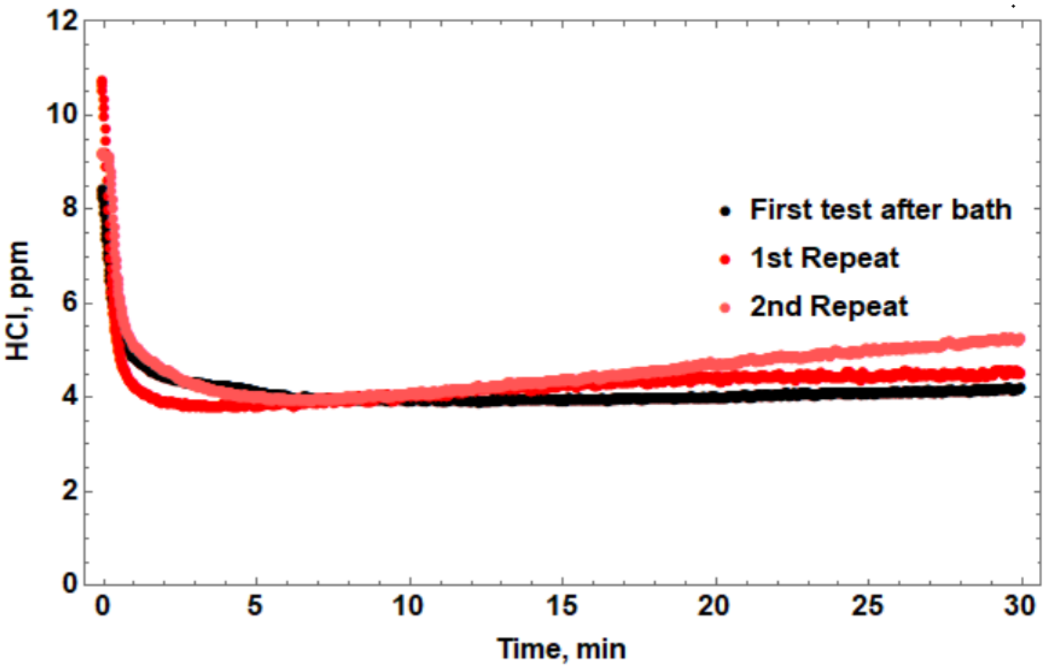

Figure 5.7: Repeated tests at 50% RH after a water bath.

5.1.7 Dry Test following a Humid Test

Lastly, a sample was subjected to HCl flow with dry air after a 50% RH flow test, as shown in Figure 5.8. This change in saturation is significantly more than the change in saturation after the repeat of the sample in dry conditions from a previously saturated sample in dry conditions (Fig. 5.2). Comparing Figs. 5.2 and 5.8, it can be seen that water vapor influences how much capacity anodized aluminum has to uptake HCl even in a dry environment. This indicates that with the aid of water vapor, HCl can create even more aluminum chloride, whether further down in the oxide layer, or packing it in further near the surface. It also implies that the adsorption of HCl onto alumina with the aid of water vapor is more stable, and uptake capacity will not return to pre-saturation levels with just air flow alone.

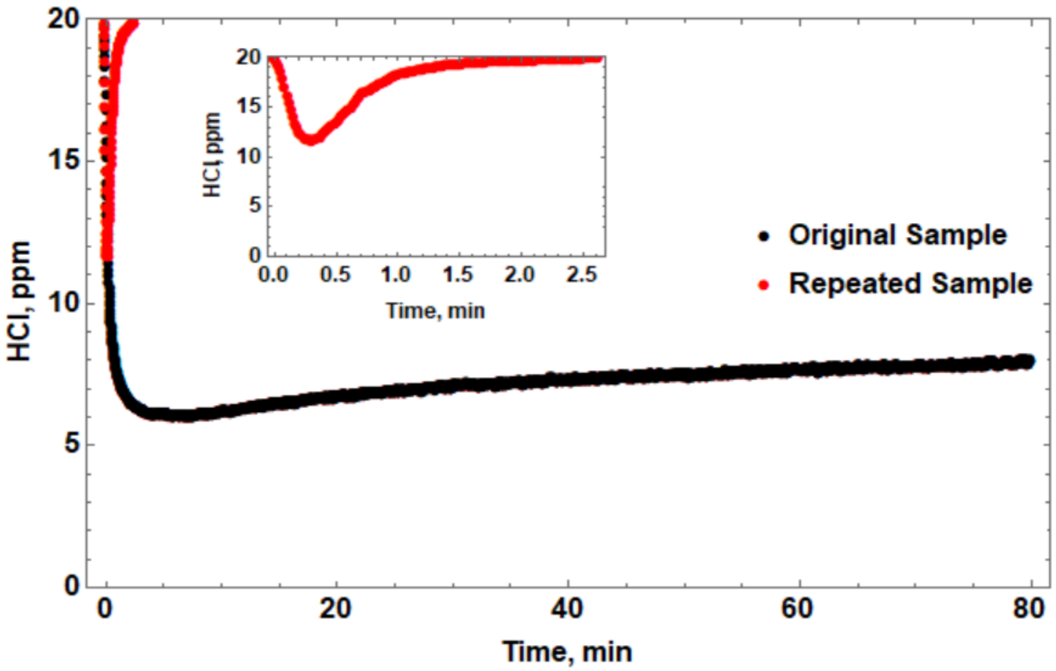

Figure 5.8: Sample subjected to HCl in dry air after it was placed under HCl flow with 50% RH for 80 minutes. Insert highlights the repeated sample at smaller time range.

5.1.8 XPS Analysis

XPS was performed on a sample that had been subjected to HCl and 50% RH flow for an hour. Figure 5.9 shows that chlorine is found much deeper in this oxide layer than in the sample that had saturated in HCl and dry air, as highlighted in Fig. 4.11 (2,200 nm vs. 5,500 nm). This suggests that the mass transfer of the HCl into the oxide layer is enhanced by the water vapor. One theory is that at high enough humidity, water vapor fills the void space in the aluminum chloride produce layer, giving a path for chlorine to mobilize further down into the oxide layer. A model that can predict this phenomenon is discussed later in this chapter.

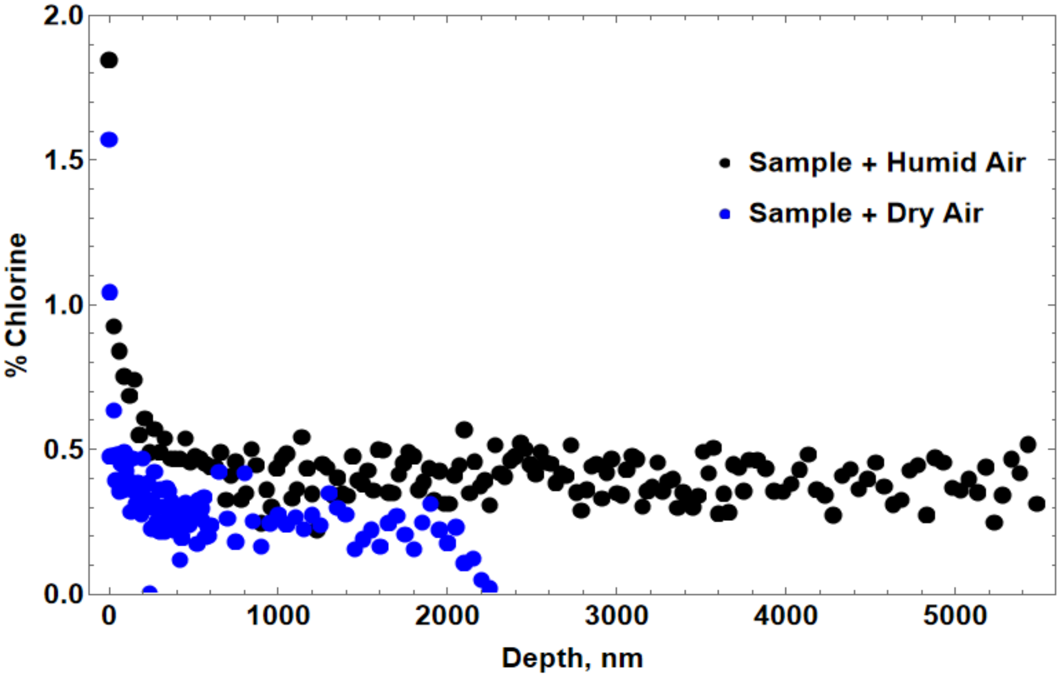

Figure 5.9: XPS of anodized aluminum sample that had been subjected to HCl and 50% RH air flow.

5.2 Other Surface Experiments with Humidity

The same test outlined in Section 5.1.6 was performed on a Chromate Conversion Coated (CCC) aluminum sample (repeated 50% RH gas stream on same sample). These results are shown in Fig. 5.10. The experimental response curve started the same as other aluminum samples in dry air, with the outlet sensor reaching a minimum and then recovering to the initial value. However, on the way back up to the initial value, the response stalled and then began decreasing, indicating an increase in HCl uptake. This sample was repeated twice more under the same conditions. In both repeated tests, there was no recovery and the curve continued downward. Since the presence of chlorine was observed from XPS at 5,000 nm depth into the anodized layer, it can be inferred that HCl or chlorine can penetrate past the 250 nm oxide layer in the CCC aluminum, reaching the bare aluminum where the reaction is more intense [37, 68]. A plausible explanation is that this "corrosion" likely causes an increase in surface area, allowing additional uptake, as observed in the experiments.

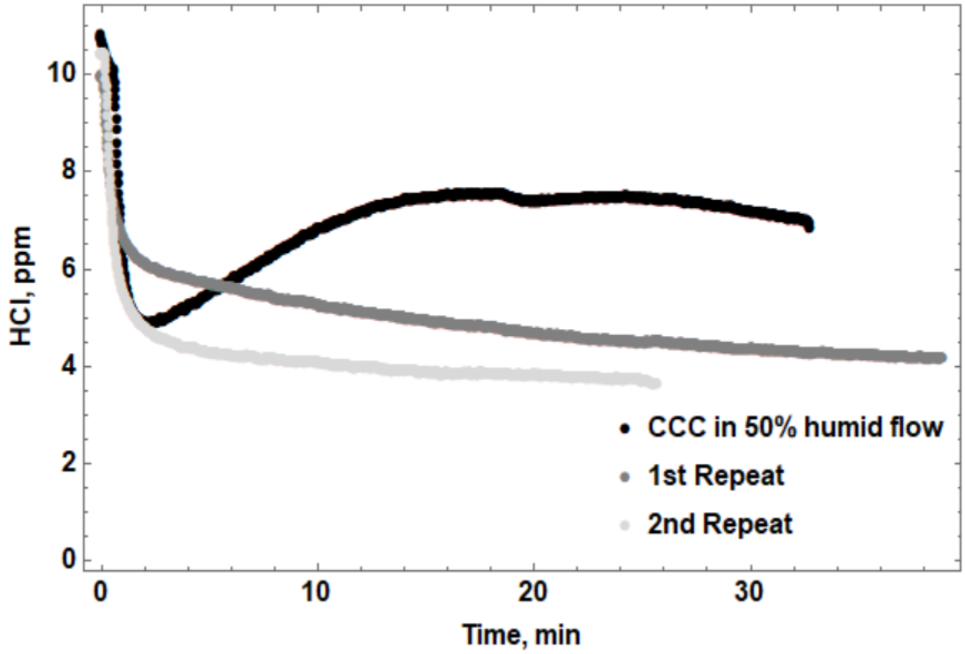

Figure 5.10: Repeated tests at 50% RH for CCC aluminum.

Repeated tests of Nomex were also performed under both dry and humid conditions. Figure 5.11 shows results of the Nomex test repeated under dry conditions after saturation. As expected, less uptake is realized on the second test with the same Nomex sample. Figure 5.12 shows the same test sequence but under 50% RH flow. The repeated test provided more HCl uptake (351 vs. 506 µmol/m^2). This is unusual behavior, as every other repeated test sequence under the same conditions presented in this chapter has less uptake during the second test. It is possible the acid frayed the fabric, which provides more surface area for HCl uptake. Another difference with the Nomex fabric compared to aluminum is that less uptake is realized in the presence of water vapor compared to the dry air case (814 vs. 351 µmol/m^2). It is likely that water and HCl compete for sites on the Nomex fabric.

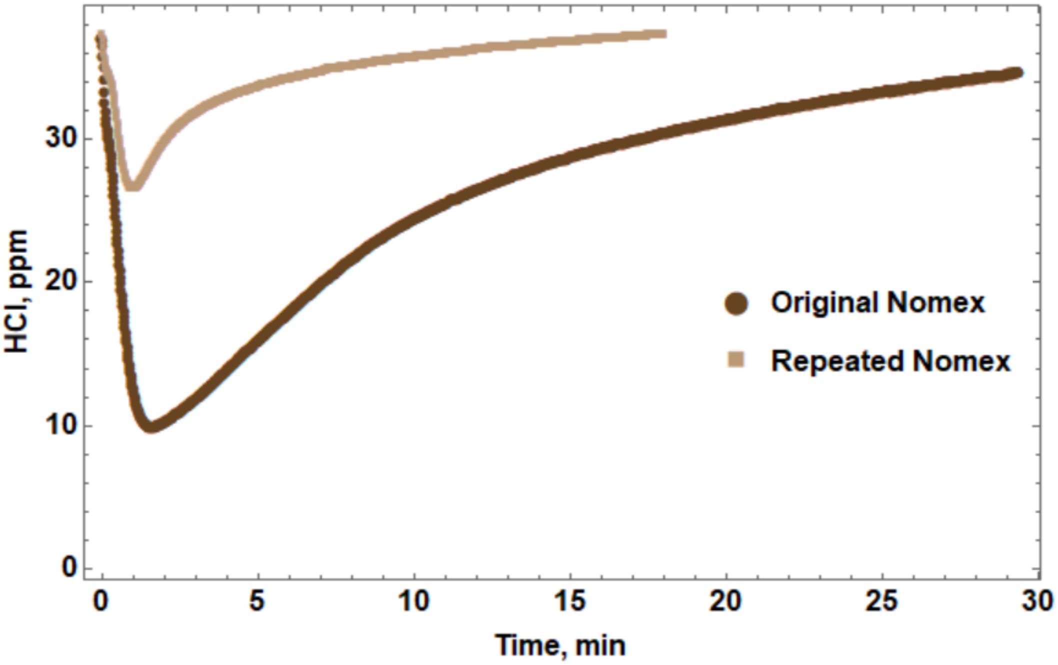

Figure 5.11: Repeated Nomex tests in dry air.

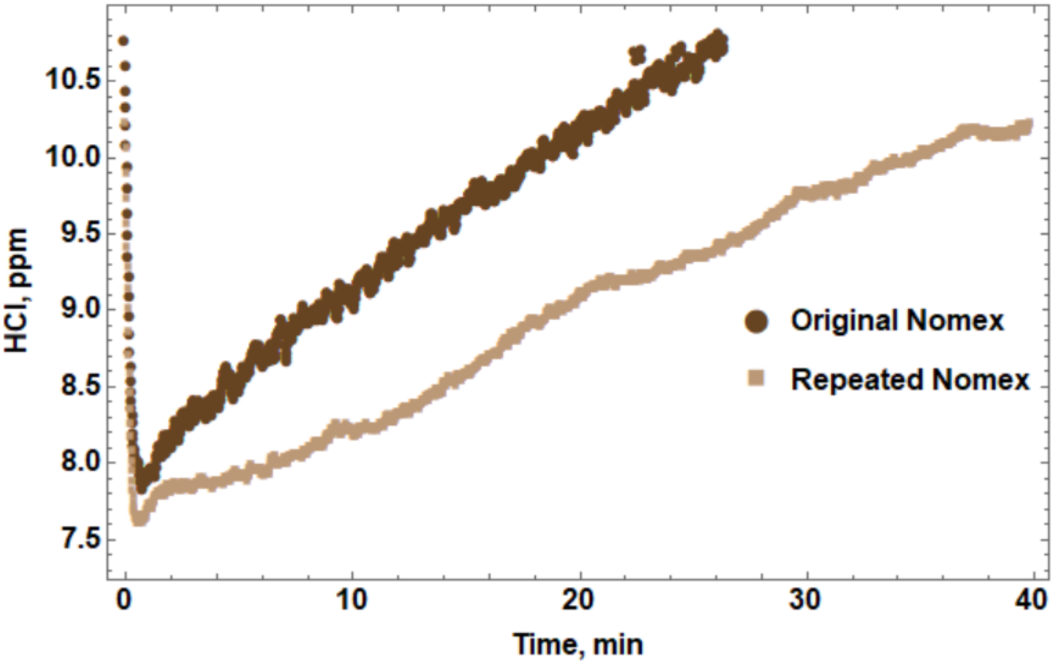

Figure 5.12: Repeated Nomex tests in 50% RH air.

5.3 Discussion of Experimental Results

The cumulation of these experiments show the profound effect water vapor has on the uptake of HCl by aluminum, from the water vapor that is in the oxide layer, to the water vapor in the gas stream during testing, which likely influences the water vapor in the oxide layer. While the primary reaction involving HCl and alumina is the creation of aluminum chloride, water appears to add additional pathways for transport and reaction.

For the repeated dry tests with no intervention in between them (Fig. 5.2), the aluminum chloride is the primary reason the sample saturates and the interaction with HCl and alumina stops the first time. If, after the first test, the second test was immediately performed, there would be significantly less uptake, possibly none at all. The 24-hour period between tests allows some more water vapor to adsorb on to the sample, giving HCl an additional point of uptake and to dilute into hydrochloric acid. For the humid air and water bath intervention tests, these simply add more water to the oxide layer, diluting any acid that is already in the sample, and creating more water for HCl uptake.

For the humid test following a dry test that was saturated (Fig. 5.5), the water vapor from the gas stream likely condenses on the aluminum chloride layer and creates a liquid network within the aluminum chloride layer where HCl dissolves and chlorine ions can transport further into the oxide layer due to capillary action. This is why more chlorine is found in the XPS results of the sample subjected to HCl and a humid gas stream, as compared to a sample saturated in just dry HCl. A likely explanation of what happens after multiple humid tests is that slightly more aluminum chloride is formed each time, leaving less room for water, and less ability to dilute the solution. This is why there was significantly less uptake for the dry test that followed a humid test, as more aluminum chloride was formed in the humid test as compared to the dry test.

In order to predict this phenomenon, the enhanced mass transport due to capillary condensation and diffusion that water provides can be represented as an “effective” diffusion coefficient for the aluminum chloride layer that changes as a function of RH of the gas stream. This effective diffusion coefficient is postulated to encompass any additional mechanisms that enhance the mass transfer of the HCl.

5.4 Modeling HCl-Anodized Aluminum Interactions in the Presence of Water Vapor

The experiments presented in the preceding sections have demonstrated the increased uptake of HCl by anodized aluminum in the presence of water vapor (RH in the air flow). XPS results also show that chlorine is found deeper in the oxide layer compared to anodized samples exposed to HCl in dry air. This indicates an increase in mass transfer of HCl into the pores of the oxide layer. One potential explanation is that the water vapor reacts with the aluminum chloride layer, allowing HCl to diffuse further down into the pore, assuming that the diffusivity of HCl is higher in the product of the reaction compared to in the aluminum chloride itself. However, there is little evidence that water vapor and $AlCl_3$ form a chemical reaction at room temperature. XPS of the 50% RH test shows more chlorine overall, and just as much at the surface, than in the corresponding dry tests, implying more aluminum chloride is formed. To further demonstrate this point, two more samples of HCl saturated anodized aluminum were observed under XPS. One sample was subjected to 30 minutes of dry air at 1,000 ccm, while the other was subjected to 30 minutes of 50% RH air flow. The chlorine content was nearly identical, as shown in Figure 5.13. This implies no reaction takes place between $AlCl_3$ and water vapor.

Another theory is that the inclusion of water vapor helps increase mass transfer into the oxide layer. It might sound counter intuitive that water filling in the void space of the aluminum chloride

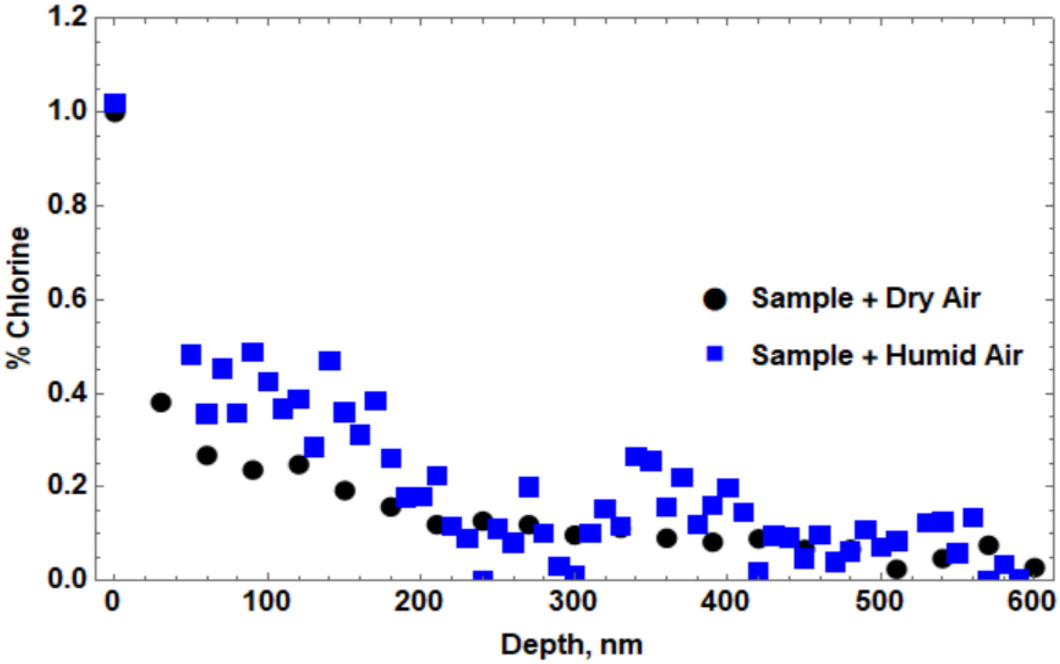

Figure 5.13: XPS results showing chlorine content of HCl saturated samples where one was subjected to dry air after saturation, and one to humid air after saturation.

previously occupied by air would help decrease mass transfer resistance (with air's mass diffusion coefficient being much larger than water's). However, water vapor in the atmosphere increases the chance that capillary condensation occurs, and a liquid network develops throughout the alumina/aluminum chloride layer, dissolving HCl in it and generating chloride ions that can mobilize their way further down into the oxide layer. This mobilization of chlorine was demonstrated in concrete, a similar porous solid [78, 79]. In these works, concrete was subjected to HCl, created by the combustion of PVC which produces mainly HCl. Chlorine content was then measured as function of depth into the concrete and humidity, providing an expression for the diffusion coefficient of HCl in concrete as a function of humidity A similar approach to predict the increased mass transfer of HCl in aluminum in the presence of water vapor is explored here.

As was alluded to in Section 5.3, an expression for the increased diffusion coefficient as a function of RH is determined. First, the pore model was used to calibrate D_{AlCl3} for each experiment where humidity was varied. Two examples of this calibration are provided in Fig. 5.14. This was done to obtain a curve of diffusion through the aluminum chloride layer as a function of humidity, which is provided in Fig. 5.15. For the examples provided in Fig. 5.14, the model gave the best prediction at D_{AlCl3} = 9x10^{-12} m^2/s and 1x10^{-10} m^2/s for the 37.5% RH and 50% RH cases, respectively. The dry air data shown in Ch.4 resulted in 3x10^{-12} m^2/s as the best fit. deVere et al. [79] measured the diffusion coefficient in concrete and found that the diffusion coefficient decreases about two orders of magnitude when the RH of the atmosphere in equilibrium with concrete is lowered from 95% to 54%. A similar two order of magnitude drop in diffusion coefficient is realized from 50% to 0% RH.

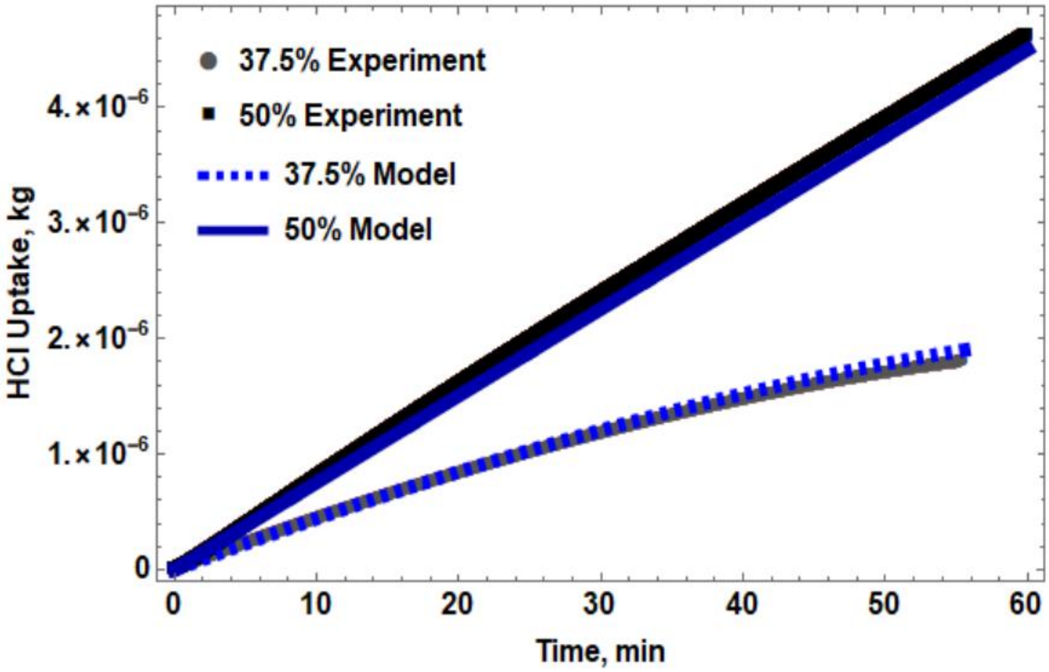

Figure 5.14: Calibration of pore model to obtain D_{AlCl3} for different RH levels.

Saetta et al. [80] modeled chloride diffusion through partially saturated concrete by proposing the following power-law based equation:

$$D_{RH} = \frac{D_{100\%}}{1+\left(\frac{1-RH}{1-RH_C}\right)^4} \tag{5.1}$$

In Eq. 5.1, $D_{100\%}$ is the chlorine diffusion coefficient at 100% RH and RH_c is the critical RH at which the value of D is half the corresponding value of 100% RH. For this work, 45% seemed to be this value, which agrees with the observation that the uptake characteristics seemed to change more drastically in terms of not saturating. While Eq. 5.1 did mimic the S-shaped behavior of the diffusion coefficient, the curve was too shallow and did not provide a good fit to the data (the only fitting parameter is RH_c). It was not until the power (= 4 in Eq. 5.1) was increased to 25 that the equation began to fit the data reasonably well. Eq. 5.1 is plotted in Fig 5.11 for a power of both 4 and 25. Another possible way to fit S-shaped data is to use an exponential function, as proposed in Eq. 5.2. Here, the slope, *Sl*, may be adjusted to fit the data using the least square method. Trial and error yielded a value of 2.9 as the one that gave the best fit. This exponential model fitted the data better, especially near the jump at the critical RH, as is seen in Fig 5.16.

$$D_{RH} = \frac{D_{100\%}}{1+exp\left(\frac{RH_C-RH}{Sl}\right)} \tag{5.2}$$

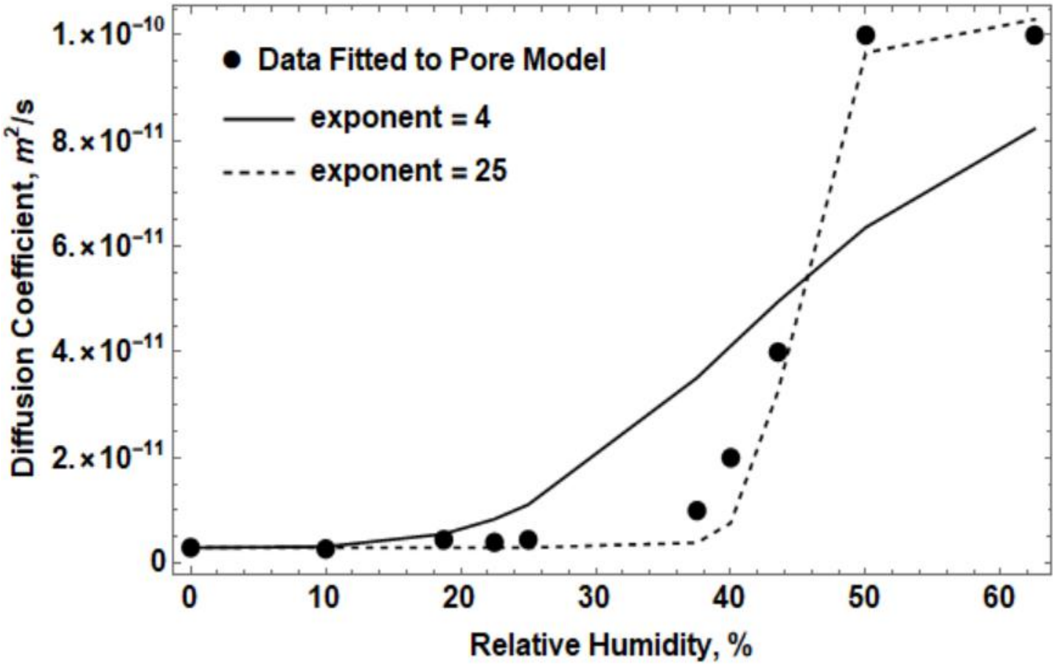

Figure 5.15: Power-law fit (Eq. 5.1), with an exponent of both 4 and 25, to the D_{AlCl3} obtained from the pore model as a function of RH.

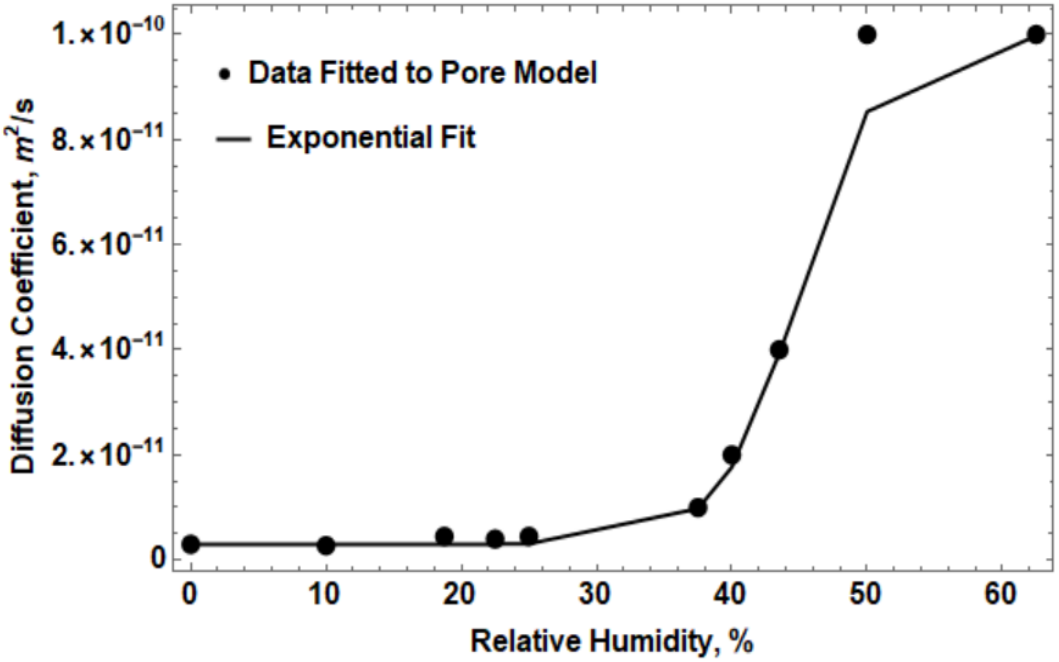

Figure 5.16: Exponential fit (Eq. 5.2), with a slope of 2.9 and critical RH of 45%, to the D_{AlCl3} obtained from the pore model as a function of RH.

5.5 Summary

Water vapor in the form of humidity in the atmosphere proved to increase the uptake of HCl by aluminum. A RH of at least 25% was needed to notice an appreciable difference in the uptake characteristics, and 45% proved to be the critical RH where a significant difference in uptake is realized and an anodized aluminum sample did not saturate. Repeated tests with the same sample under dry conditions produced less uptake each subsequent test. When the sample was placed under 90% RH air flow between tests, more uptake capacity was recovered, but the sample was not nearly returned to pre-test conditions. After placing the sample in a distilled water bath between tests, most of the capacity was recovered for the next test. These tests show that water can be used to clean surfaces after a fire event on a spacecraft, but there is likely irreversible damage.

XPS showed that chlorine was found deeper in the oxide layer of anodized aluminum tested with humid air as opposed to dry air. This suggests that water vapor enhances the mass transfer through the aluminum chloride product layer giving a path for chlorine to mobilize farther down into the oxide layer. A model was proposed that developed a relationship between RH in the air flow and diffusion coefficient in the aluminum chloride product layer.

Nomex and CCC aluminum were also tested under humid conditions. Nomex was notable for having less uptake in the presence of water vapor. It is likely water and HCl compete for similar sites on Nomex. The CCC aluminum response to HCl under humid condition started the same as the dry response, but before it could reach saturation, the outlet sensor curve reversed course back down, signifying more HCl uptake. This indicates that corrosion of the sample is likely, which would increase the surface area, allowing more uptake of HCl.

Chapter 6: LARGE-SCALE TESTS AND MODELING

The Saffire project provided a chance to test acid gas release in a real spacecraft in a microgravity environment. Two bottles of HCl were released during the campaign: a standalone release and a release during the burning of a cotton fiberglass blend. However, the largest response in HCl came during a burn of polymethyl methacrylate (PMMA) that produced no HCl. A ground-based apparatus was constructed to flow acid gas at the concentration and length scales seen in a spacecraft, such as the Cygnus vehicle within which the Saffire project takes place. HCl was flowed through a duct where the walls are made of the sample material. Tests were performed in the duct with walls made of both stock aluminum and anodized aluminum. A CFD model of the duct using the reaction rates developed in the previous chapters was used to mimic the experiments and test the validity of the reaction rates in a larger-scale environment and a different configuration. The model of the duct was then used to simulate conditions seen in the Saffire experiments.

6.1 Large-scale Microgravity Experiments

A series of microgravity experiments, known as Saffire, have been developed by NASA to test realistic fire scenarios in a full-scale spacecraft. Opportunities to test novel gas species sensor technology in a realistic flight configuration have been provided by these experiments. Events in the Saffire experiments produce HCl in the vehicle by flowing gas straight from a cylinder as a standalone event, or concurrently during a solid fuel burn. These data give a great opportunity to test the predictive methods developed in this work. As a reminder, Table 1.3 provides the test events in the Saffire IV campaign that will be discussed as they relate to HCl in a spacecraft environment. Event 2 was a standalone HCl bottle release while Event 4 was an HCl bottle release during the burning of SIBAL cloth.

Figure 6.1 shows the HCl concentration recorded by the FFD for Event 2 and 4. Event 2 did not respond to the HCl release, while Event 4 produced a noticeable increase followed by a slow return to baseline over 4,000 seconds. One possibility for the lack of response is that HCl is sucked into the ECLSS system before reaching the FFD. Any HCl that goes into the ECLSS system will likely not come out the other end due to the high surface area of the filters in there.

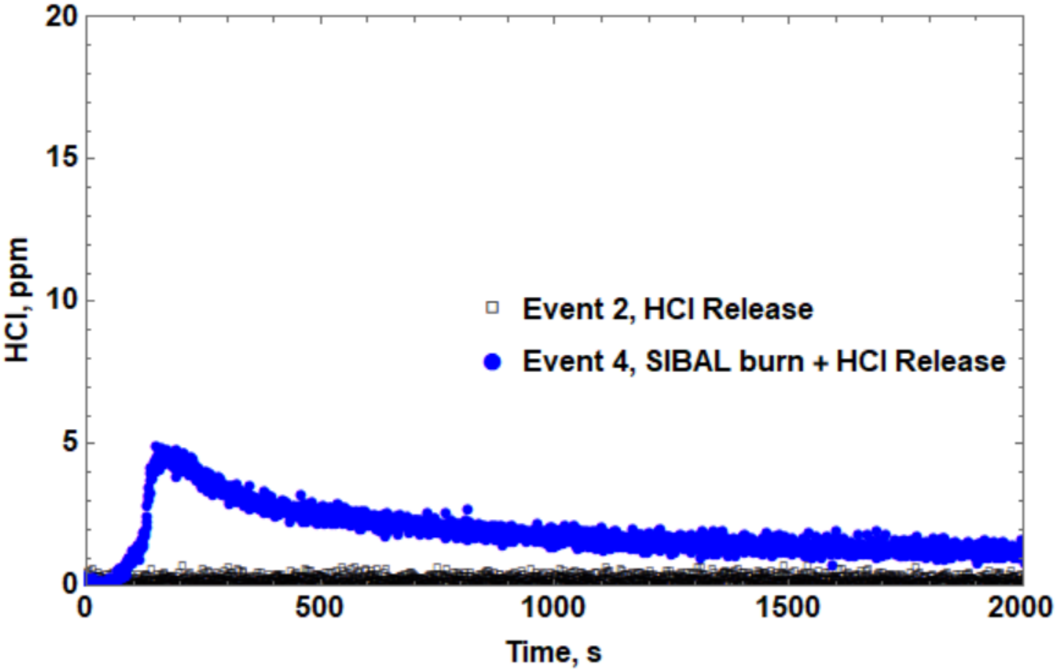

Figure 6.1: HCl concentration for Event 2 (HCl release) and Event 4 (HCl release with SIBAL burn).

However, the results from RS6 in the zenith end cone and the FFD (shown in Fig. 1.3) present a sharp increase in CO_2 response, showing that released gases and combustion products do make it to the sensors before entering the ECLSS system for recirculation. Figure 6.2 shows this CO_2 data. A more likely explanation for the small HCl response is that all of the HCl interacted with

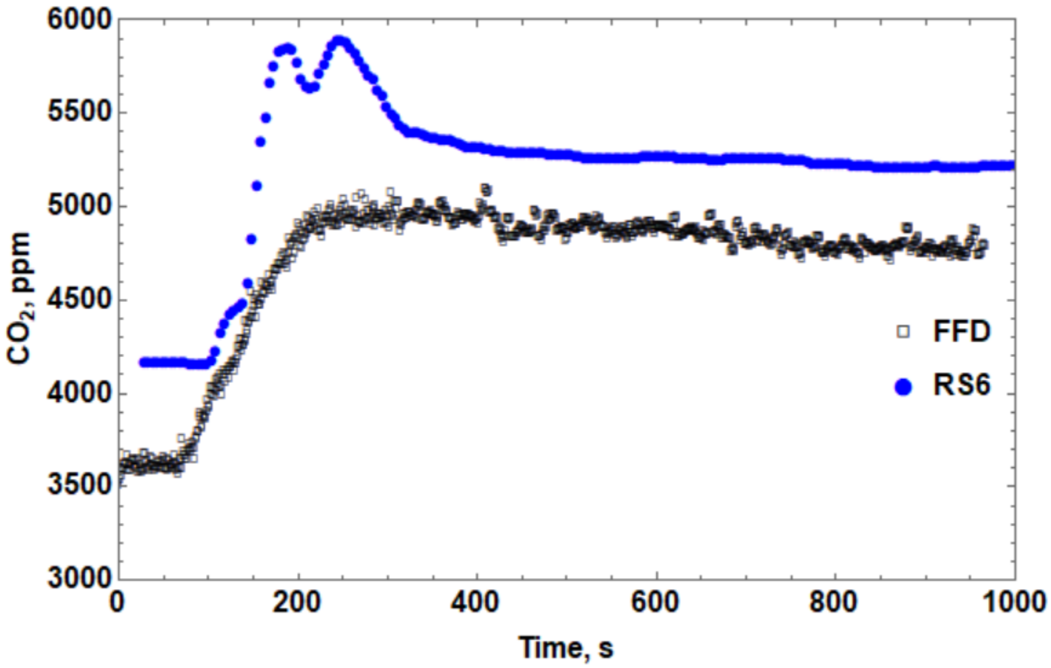

Figure 6.2: CO_2 concentration for the FFD and RS6 during Event 4 SIBAL burn.

the walls of the spacecraft and surfaces of the cargo and got uptake, thereby preventing it from reaching the acid gas sensor in the FFD. This possibility will be explored in the next sections. Since there is a finite capacity to uptake HCl by the surfaces studied in this research, there is less to uptake later with the second release of HCl, which provides some reasoning as to why more HCl would be detected during the second bottle release.

Event 5 burned PMMA, which is often substituted for glass, such as in shatter proof windows. Figure 6.3 shows the HCl concentration measured by the FFD. The gap in data is due to the unexpected reignition of the sample. During the PMMA burn event, the fans were turned off as planned to extinguish the flame. Now with no forced flow, and no buoyant flow due to the lack of gravity, the heat remained near the sample, continuing to vaporize the fuel. When the fan was turned back on, a deflagration wave reignited the sample and this is postulated to be the reason telemetry was disabled for a period of time.

The combustion products of PMMA do not include HCl; however, this event provided the largest response in HCl by the sensor. Much hotter temperatures are produced in this case compared to the SIBAL burn, as shown in Fig. 6.4. This indicates that desorption likely plays a role, which is a naturally occurring phenomenon as temperatures rise. The process is often used to treat contaminants in air and soil [81, 82]. Elam et al. [62] studied desorption of HCl on a single crystal of Al_2O3, determining HCl desorption occurred over a wide temperature range of temperatures (300 to 650 K). This broad temperature range suggests a distribution of surface sites with different binding energies [62].

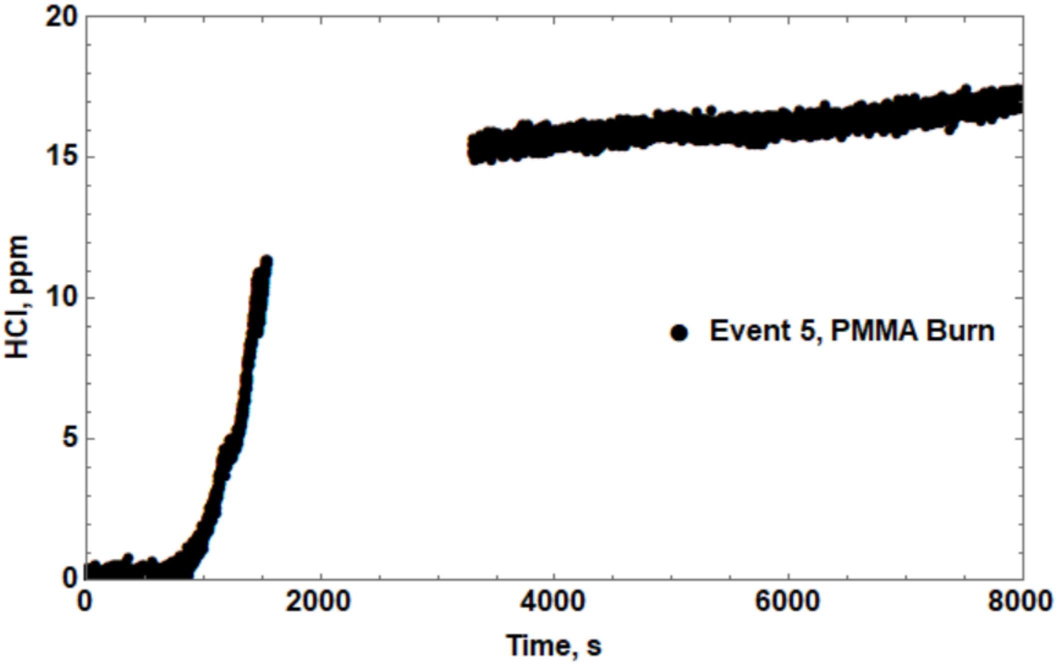

Figure 6.3: HCl concentration for Event 5 (PMMA burn, no HCl release).

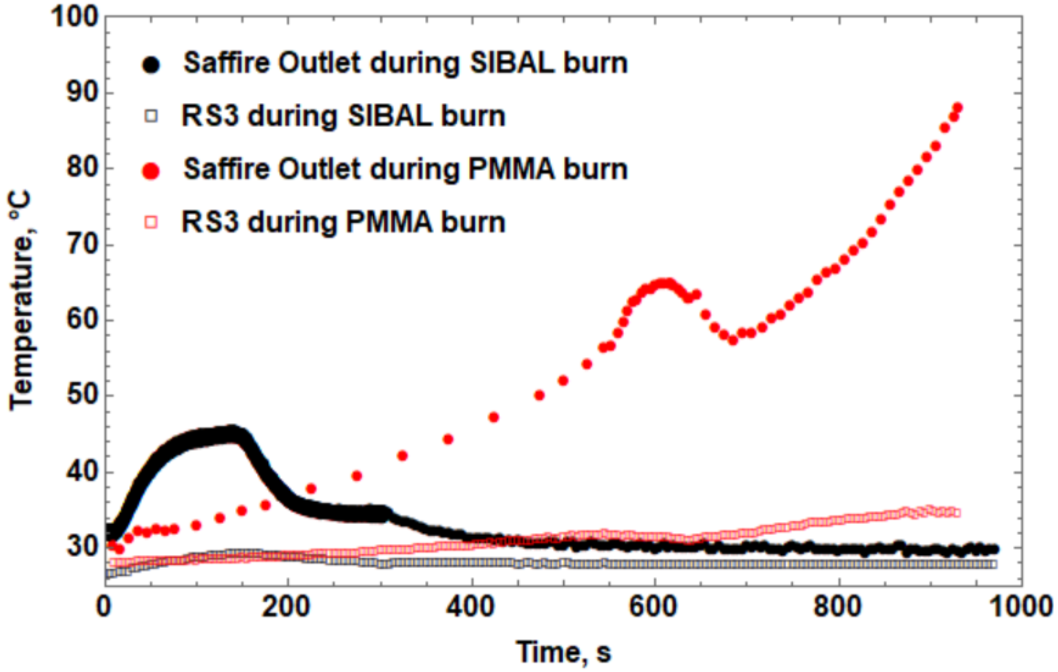

Figure 6.4: Temperature of Saffire outlet and RS3 in Events 4 and 5.

6.2 Large-scale Ground-based Duct Experimental Results and Modeling

A ground-based experiment was created to compare the 0-g results from Saffire to 1-g results, and to help design future 0-g tests. This apparatus is detailed in Ch. 2.5. The flow duct where acid gas interactions are studied was designed to be the size of the forward port standoff in the Cygnus vehicle, (50 cm wide by 45 cm high and 3.6 m in length). Five holes are placed 2.5 cm from the inlet to probe the concentration and velocity entering the duct, as shown in Figure 6.5. There are also holes placed at the mid-length of the duct (z = 1.8 m) and 2.5 cm from the outlet of the duct.

First, CO_2 was flowed through the duct to test the effectiveness of the static mixer and the assumption that the flow would be well mixed at the inlet. A flow of 10 lpm of 100% CO_2 was flowed into the static mixer, while the air flow through the duct was varied to test mixing at different flow rates, given in Table 6.1. Equation 6.1 provides the expected theoretical well mixed

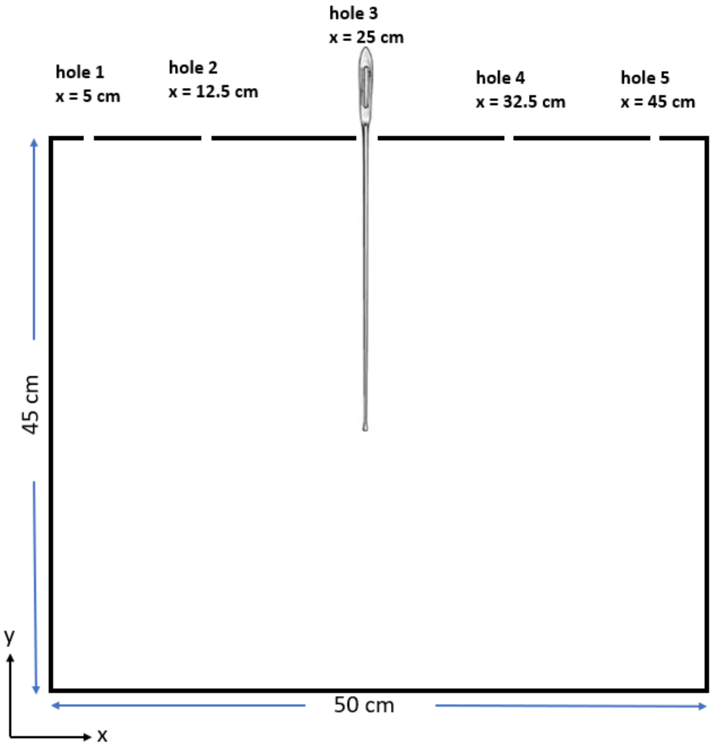

Figure 6.5: Schematic of duct inlet with probing locations.

Table 6.1: Largest percent difference from average CO_2 concentration.

Flow Speed in Duct (cm/s)	Largest difference from average at inlet (%)	Largest difference from average at outlet (%)
28	2.5 (hole 1, y = 5 cm)	1.1 (y = 5 cm)
20	1.9 (hole 1, y = 7.5 cm)	0.9 (y = 40 cm)
10	1.7 (hole 4, y = 5 cm)	0.5 (y = 25 cm)

concentration of CO_2 in the duct (c_{Duct}). For example, for 20 cm/s of air flow, the volume flow rate of the duct ($\dot{V}_{Duct}$) is 0.045m^3/s (2,700 lpm), which for a $\dot{V}_{SM}$ of 10 lpm and c_{SM} of 1,000,000 ppm would give a theoretical well mixed value of 3,700 ppm.

$$c_{Duct} = \frac{c_{SM}\dot{V}_{SM}}{\dot{V}_{Duct}} \tag{6.1}$$

Measurements of the CO_2 mixture were taken at the inlet at all five holes and at 5 cm increments along the y-axis, giving a total of 45 measurements at each flow speed at the inlet. Nine additional measurements were done at the outlet. Table 6.1 shows the largest percent difference of this average for each flow rate. It can be observed that the mixing gets better at lower flow rates. This is logical as the flow spends longer in the static mixer and diffusive mixing evens out the concentration field. As expected, the mixture is more uniform at the outlet as the CO_2 has more time to mix. This data provides confidence that the flow is well mixed, and a single constant concentration value can be used at the inlet for any simulations.

Next, a series of tests was done with an anemometer to determine the flow velocity profile entering the duct. Since there were many turns, (plus the static mixer) from the fan to the duct inlet, the flow was not uniform at the inlet of the duct. Fig. 6.6A shows the flow profile, measured at the same 45 locations as the CO_2. The flow was significantly higher (almost 4 times the bulk average in the top left corner. A series of mesh screens (TWP Inc. 0.0021 inch wire diameter 200 mesh) were used to straighten the flow until the maximum divergence from the mean of the flow was 10%, which was the same requirement for the Saffire payload. These mesh screens were also PTFE treated to minimize interaction with HCl. A minimum of six were required to straighten the flow to within 10%. This velocity profile is shown in Fig. 6.6 B.

The first test of the ground-based duct flowed HCl through a duct with stock aluminum walls. A flow rate of approximately 100 cubic feet per minute gave a velocity of 20 cm/s through the duct. The flow of acid gas into the static mixer ranged from 0 liter per minute to 10 lpm from a 1% HCl bottle (balance air), which provided a theoretical HCl concentration from 0 to 37 ppm at the outlet of the static mixer. Figure 6.7 shows the HCl results at the inlet and outlet, which were probed at 11.25 cm from the top. From the inlet results, it can be deduced that the static mixer, inlet diffuser and flow straighteners uptake a significant amount of HCl. There is not much

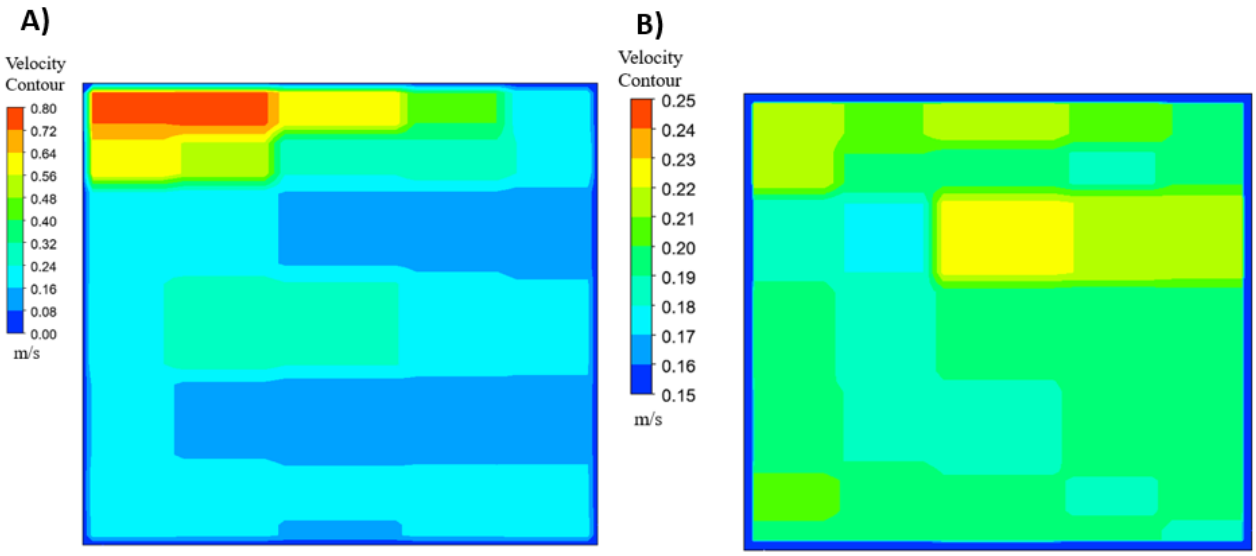

Figure 6.6: Velocity profile of duct inlet without flow straighteners (A) and with six flow straighteners (B).

difference in the inlet and outlet sensor response, due to the low uptake by stock aluminum. By the time the flow was ramping back down to 5 lpm after the 2,000 s mark, the inlet and outlet were almost identical, indicating the walls were saturated. By integrating the inlet and outlet HCl curve, the approximate uptake of HCl was 102 μmol/m^2. This was slightly over the 80.1 μmol/m^2 capacity measured in the reactor experiments. The RH measured at the inlet of the duct was approximately 32%, with less than 1% temporal variability. This is less than the 45% critical RH, but still enough water vapor to enhance the uptake slightly.

A CFD model of the duct was used to predict the HCl at the outlet. The inlet sensor concentration was used as an input, while the site density of 80.1 μmol/m^2 measured in the reactor experiments was used on the walls, along with the other kinetic parameters used in the dry reactor model. Both a 3D and 2D axisymmetric model with a matching hydraulic diameter (0.48 m) were simulated showing no noticeable difference; so, the 2D axisymmetric model was used moving forward. Using the hydraulic diameter and the velocity of 0.2 m/s, the Reynolds number was determined to be 6,400, therefore a k-ε turbulence model was implemented. The turbulent intensity used, calculated by Eq.6.2 was determined to be 5.35%. There are 3,660 cells in the model. Figure 6.7 shows the predicted HCl concentration at the outlet. The agreement is excellent.

$$I = \frac{u'}{u} = 0.16Re^{-1/8} \tag{6.2}$$

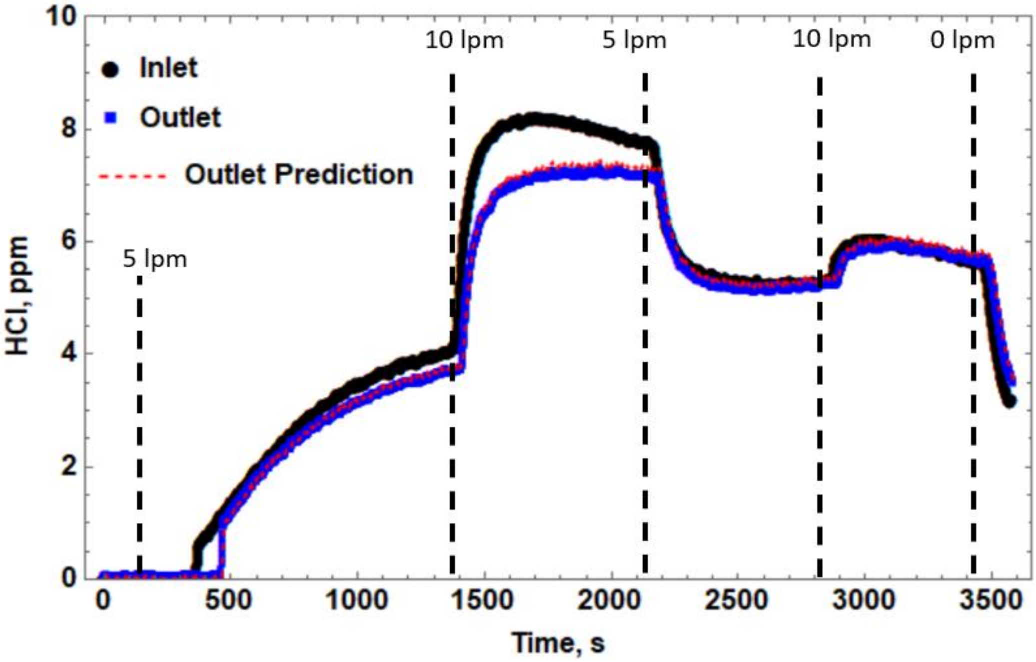

Figure 6.7: Inlet and outlet HCl sensor readings and prediction for stock walls.

When switching out the wall panels to test anodized aluminum, a white substance was found to coat the stock aluminum walls as seen in Fig. 6.8. A sample of this wall was then subjected to XPS testing and was found to be aluminum chloride. The oxide layer is designed to passivate or slow the reaction with HCl, but once HCl reaches past the oxide layer, it becomes more reactive with aluminum [68]. Any humidity in the air enhances mass transfer through the oxide layer, helping the HCl reach the raw aluminum faster. Since the stock aluminum has an oxide layer that is two orders of magnitude thinner than anodized aluminum, a visible amount of aluminum chloride can be realized.

Figure 6.9 presents the results for HCl flow through a circular duct with the anodized walls. A similar ramping up and down of the HCl concentration was used as in the stock aluminum study, with this case reaching up to 20 lpm (theoretical mixture at static mixer outlet of 72 ppm). Since the RH was approximately 45% throughout the test, and anodized aluminum was being used, the multiscale model was deployed to predict the uptake of HCl. Equation 5.2 was used at 45% RH to determine an aluminum chloride diffusion coefficient of 5x10^{-11} m^2/s. The same process described in Section 4.3 was then used to determine the diffusion resistance from the pore model and set an expression for the diffusion coefficient at the cells adjacent to the reacting surface. This expression is as follows:

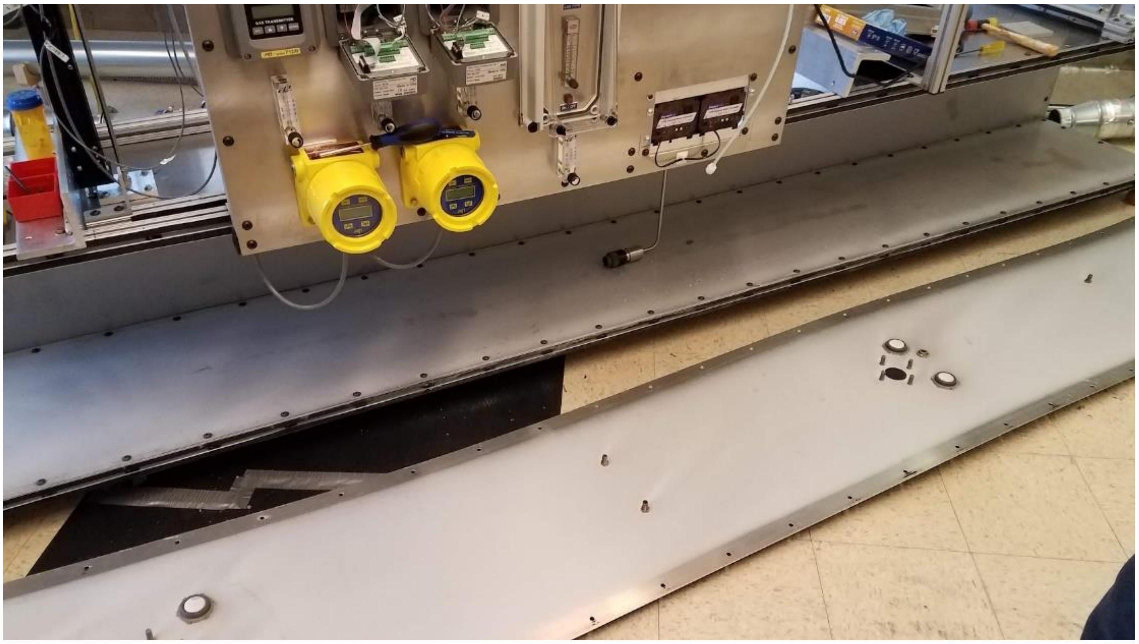

Figure 6.8: Stock aluminum duct walls after being subjected to HCl.

$$D_{eff} = 1.55x10^{-5} e^{-2.5\left(\int_{t_0}^{t} c_w\right)^{0.33}} \tag{6.3}$$

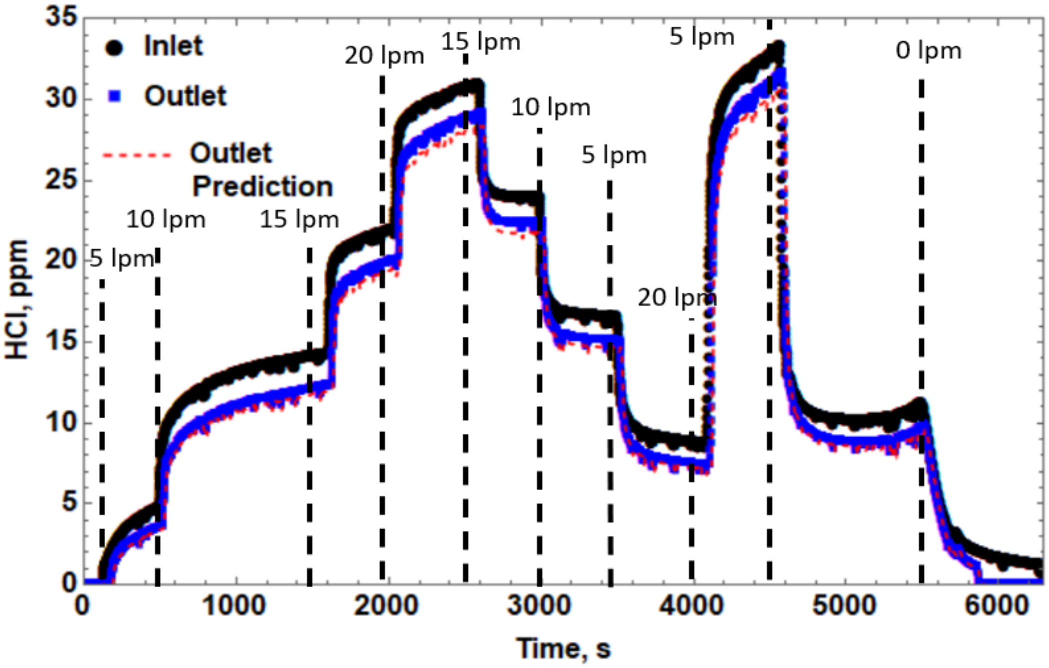

Figure 6.9: Inlet and outlet HCl sensor readings and prediction for anodized aluminum walls.

An excellent agreement between experiments and model predictions is also observed for anodized aluminum.

6.3 Spacecraft Modeling

It was clear from the results of the ground-based duct experiments and model that most of the HCl makes it to the outlet. Since no HCl is detected by the FFD during the first bottle release of the Saffire IV experiments, but the ground-based experiments and models imply a significant amount of HCl would leave the forward port standoff, it stands to reason that the open part of the spacecraft provides significant uptake of HCl. In order to better determine how HCl diffuses in a spacecraft, a volume of the size of the zenith hatch that housed the FFD (3 m in diameter, 1 m in length) was added to the duct model. Cargo comprised of a Nomex surface matching the surface area as described by Saffire IV post mission analysis (6.5 m^2) was also inserted in the model. The turbulent parameters as described by the duct model were used in this model. The additional volume brought the total amount of cells to 5,253. Figure 6.10 shows the schematic of the model used. The walls were made of anodized aluminum. Since the RH in Saffire was approximately 45%, Eq. 6.2 was used in the interaction of anodized aluminum.

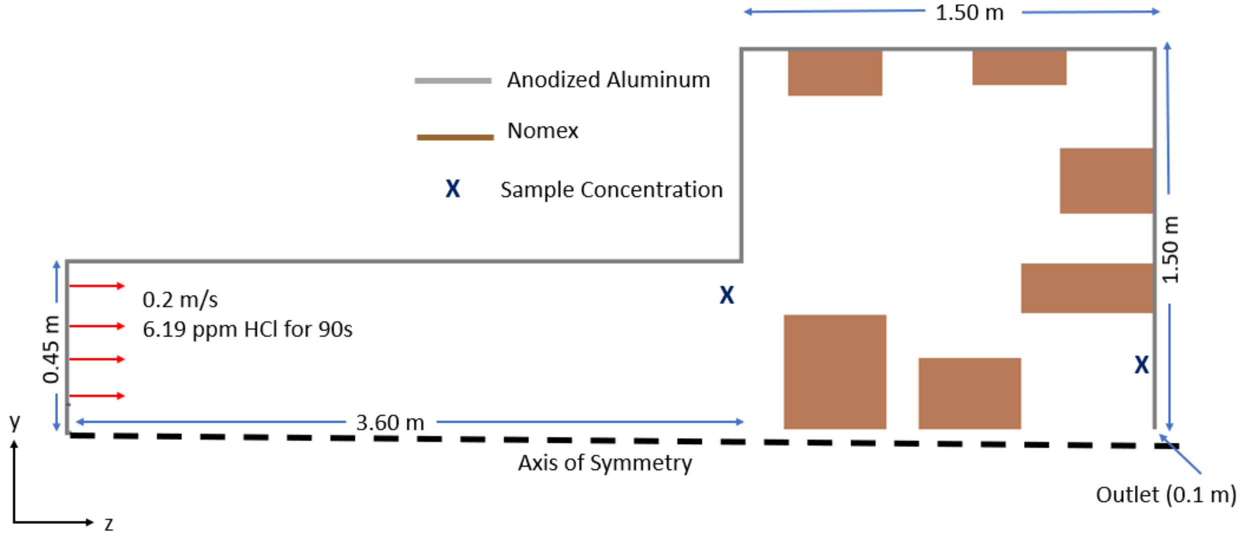

Figure 6.10: Schematic of spacecraft model.

The simulation input parameters were determined from the HCl release events in Saffire IV. Pressure valve data of the cylinder and ground testing were used to estimate a near-constant mass flux of 2.68 kg/m^2-s for 90 s for each bottle, which provides an inlet HCl concentration of 6.19 ppm. The first simulation had the inlet concentration set at this concentration for 90s, and then set to 0 for 600 s as the HCl diffused in the volume. A second 600 s simulation was performed after the first simulation with the same inlet conditions, but without reinitializing the adsorption capacity of the surfaces, to test the HCl uptake by partially saturated surfaces.

This series of predictions serves two purposes. First, it describes how HCl diffuses in a volume like a spacecraft, and if it interacts with the walls before being picked up by a sensor. In a duct the size of the forward port standoff in Saffire IV, most of the HCl makes it from inlet to outlet, as shown during ground tests. This would indicate that sensors in the spacecraft should be able to respond to HCl at some point in time. This was not the case during the first cylinder release. The second purpose is to test the assumption that during the second cylinder release, the reason FFD produced a larger response in comparison to the first release is that most of the uptake capacity had been used up by the first release, allowing more HCl to stay in the spacecraft atmosphere longer.

Figure 6.11 presents the results for the two simulations (HCl bottle releases) at the outlet of the duct and the near the outlet of the model, representing the ECLSS input in Cygnus. These points are marked in the schematic in Fig. 6.10. As was shown in the duct experiments and predicted in the duct model, most of the HCl (over 97% by mass during both HCl releases) ends up coming out of the duct and into the spacecraft volume. During the first simulation, the sensor near the outlet almost reaches 1 ppm (16% of free stream outlet concentration) within 150 seconds and returns to 0 by 600 seconds. The model outlet sensor reaches slightly higher the second time, but not as noticeable of a change as in the Saffire experiment. After the first 600 second simulation, the site fraction (fraction of available sites for adsorption to total sites) of the Nomex surfaces went from 100% to 97%, with another 3% drop the second simulation. This indicates that the lack of available sites is not what causes the response in the FFD sensor during the second HCl bottle release.

This prediction exercise highlights a few important points about the Saffire experiments and spacecraft fire safety in general. First, it shows that significant losses of HCl do not come from the duct portion of the model, but the open volume and cargo. This indicates that the most likely reason no HCl reaches the FFD after the first HCl bottle release in Saffire is that it all interacts with the walls and cargo. Second this prediction isolates the effect of the uptake at ambient temperature.

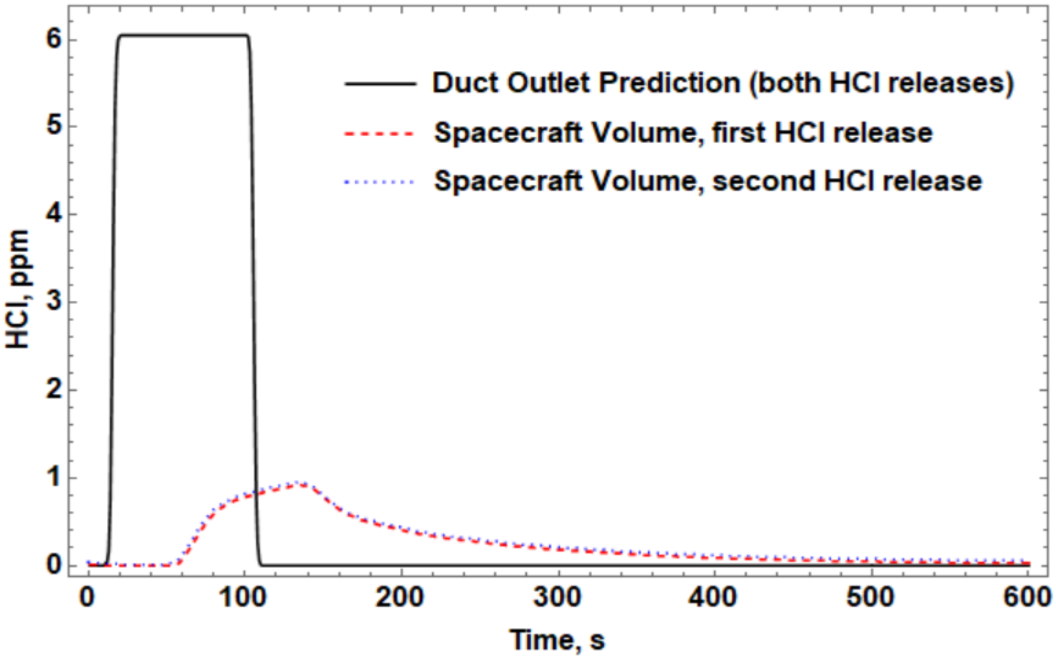

Figure 6.11: Prediction of HCl concentration in spacecraft.

Since the number of available sites alone is not enough to account for an appreciable difference in HCl in the spacecraft after two consecutive HCl bottle releases, the temperature increase from the SIBAL burn must play a role. This is likely in the form of thermal desorption of the first HCl bottle release or decreased adsorption or reaction rate at the elevated temperature. This theory is supported by the large response of the FFD sensor during the Event 5 PMMA burn. These sets of models and experiments also express the need to strategically place sensors in future microgravity experiments to detect HCl. More sensors closer to the source or, at the very least, before it flows to any large open areas would provide more useful data. Power and mass are often constrained in spacecraft missions, allowing for a limited number of sensors. Since CO_2 can diffuse easily throughout the spacecraft, placing CO_2 sensors primarily in the far field, allowing for more HCl sensors closer, to the source of the fire or gas release would provide more useful data.

In most spacecrafts, such as the ISS, smoke detectors that primarily detect CO_2 are placed in constricted areas full of electrical wires, such as science racks and avionics bays. Since there is ambient CO_2 in the atmosphere, the alarm threshold is usually higher in CO_2 sensors, leading to a longer response time compared to sensing a gas that is not found in the ambient air, such as an acid gas. Since a fire in these areas will almost certainly pyrolyze wire insulation, using an acid gas sensor in these areas could provide faster response times and lead to less false alarms.

6.3 Summary

Microgravity acid gas release experiments were performed on NG's Cygnus vehicle as part of the Saffire IV test campaign. The first acid gas release produced no response from the FFD, while only a small response was recorded during the second acid gas release. Modeling efforts infer that this response to the second acid gas release is due to temperature effects, either thermal desorption of the previously adsorbed acid gas, or less uptake of HCl at a higher temperature. These experiments and predictions highlight the importance of acid gas sensors being placed closer to the source in a microgravity spacecraft experiment to optimize the quality of the data, as opposed to a far field sensor.

Chapter 7: SUMMARY AND FUTURE WORK

7.1 Summary

The overall objective of this study was to determine the uptake of gaseous HCl on common spacecraft surfaces, primarily aluminum. To this end, a series of experiments were conducted. Physics-based models were additionally developed and validated to predict the rate of uptake of HCl on these materials. The effect of moisture on HCl uptake was also investigated. Large-scale ground tests were conducted and compared to microgravity tests. This was all completed with the goal of determining the fate of HCl gas during a smoldering fire on a spacecraft.

In order to achieve these goals, a small-scale reactor was first constructed. This reactor allowed HCl to flow over the surfaces of interest. The samples were in the shape of 2.54 cm diameter rods that were inserted into the reactor after the walls of the reactor and pipes leading to the reactor had been saturated with HCl. Under dry air conditions, it was determined that stock, CCC, and anodized aluminum had HCl uptake of 76.2, 409, and 2,900 $\mu mol/m^2$ respectively. The uptake was found to be directly proportional to the thickness of the oxide (alumina) layer on the aluminum surface.

These uptake values, in conjunction with a reactor-scale CFD model, were used to determine (calibrate) the kinetic constants for a one-step global reaction of HCl with aluminum surfaces. This global reaction rate for HCl adsorption was assumed to be first-order Arrhenius expression that accounted for active surface sites and gave excellent agreement with experimental data. These kinetic parameters used in the CFD model were calibrated using data for the CCC surface treatment but were still successful in predicting uptake from stock aluminum, and to a much lesser extent, anodized aluminum. The model was then validated at different operating conditions, such as flow rate, inlet HCl concentration and sample surface area. Nomex, a cloth-like material, was also tested and found to have an uptake of 814 μmol/m^2. For up to 5 minutes, the reactor model predicts the uptake of HCl with acceptable accuracy for all surfaces tested in this research and predicts the uptake of HCl for all time scales for lower capacity materials, deeming it an excellent predictive tool.

The uptake by the anodized aluminum samples was not predicted as well as the other surfaces. Attempts to alter the calibratable constants did not result in a better prediction, indicating other physics was relevant. Chlorine was found using XPS in the oxide layer of all surfaces tested, but much deeper in the anodized case. This chlorine is likely in the form of aluminum chloride, which adds additional mass transport resistance that needs to be accounted for in the model for anodized aluminum to yield a more accurate prediction. The oxide layer in an anodized aluminum sample is at least an order of magnitude thicker than the oxide layer in the other treatments. This realization led to the development of a multiscale model that would account for the transport of HCl into the pores of the oxide layer. First, a pore model was developed where HCl diffused into a pore and reacted with the aluminum oxide walls to create an aluminum chloride layer. This layer clogged the pore and increased the mass transfer resistance, resulting in the stoppage of the HCl-alumina reaction, and saturation of the surface. The pore-scale model was ultimately coupled with the reactor-scale model using a concentration-dependent diffusion coefficient that was used in the cells adjacent to the reacting surface in the reactor model. When compared to the single (reactor)-scale model, the multiscale model reduced the error between experiments and predictions by approximately a factor of two. The same multiscale model was also tested for stock and CCC but provided no significant increase in accuracy over the single (reactor)-scale model, which is indicative of the small oxide layer, and insignificance of its impact on mass transport. However, the results show that the multiscale model can be used to predict uptake for all aluminum surfaces, or a simpler, and likely less computationally expensive reactor-scale model can be used for low capacity or thin oxide layer materials.

Most spacecraft, especially crewed vehicles, will have the temperature and humidity set to enable the comfort and optimal performance of the crew. This means that water vapor will be in the spacecraft’s atmosphere and must be accounted for in testing HCl uptake. It was discovered that water vapor increased the uptake of HCl by aluminum. Relative humidity in the atmosphere had to reach approximately 25% at room temperature before an appreciable difference in uptake was noticed, and a critical RH of approximately 45% marked a difference in uptake behavior where the sample does not appear to saturate at all.

Repeated tests were performed on the same sample to determine how the uptake would change each time, and various treatments were performed in between tests to determine if uptake capacity could be recovered. Anodized aluminum samples subjected to a second dry test exhibited only 23.5% of the original uptake. The same series of tests subjected an anodized aluminum sample to a humid gas stream of 90% RH in between reactor tests and found the sample had an uptake of 35.6% during the second test as compared to the first. A saturated anodized aluminum sample was then submerged in distilled water in between tests, producing a difference of 82.2% between the first and second tests. Previously saturated anodized aluminum samples tested with HCl and a 50% RH air flow produced similar results in multiple repeated tests.

Results from the Saffire microgravity test campaign provided acid gas release in a realistic spacecraft environment. Acid gas released from a 1-liter bottle produced no response for the acid gas sensor in the far field of the spacecraft. A small response to the sensor was realized in the next Saffire campaign event where another 1-liter bottle was released concurrently with a structured cotton burn. The next event, which burned the rigid thermoplastic PMMA, produced significantly more HCl response by the far field sensor, despite HCl not being included in the combustion products of PMMA. Experiments were performed in a ground-based duct, with the size of the forward port standoff in Saffire, and conditions similar to the flow in the Cygnus vehicle during the Saffire campaign events. A model of the duct was constructed using the same kinetic parameters developed in this research and found an excellent prediction of the large-scale duct experiments. The results of the ground-based experiments and model found that most of the acid gas makes it from the inlet of the duct to the outlet.

An additional volume was added to the duct model to test the assumption that the uptake from the surface area in that section of the spacecraft is responsible for the low response of the sensor. In this prediction, most of the HCl reacted with the walls and cargo, leaving very little to be sensed at the far field location. However, during the second release, almost no difference was realized, which was different than the microgravity results, indicating that thermal effects play a role in HCl interaction with surfaces.

The data generated by the experimental results and modeling efforts suggest that HCl and other acid gases will not stay in the atmosphere long in a real spacecraft. This will make them hard to track and difficult to monitor for fire detection. Placing smoke detectors near the areas that have the largest probability of smoldering, such science racks and avionics bays, would be the best strategy for early detection.

7.2 Future Work

As was inferred by the Saffire experiments, temperature influences HCl uptake. Whether that effect is a decrease in reaction rate due to temperature, or desorption of adsorbed HCl, more testing is needed to answer these questions. The reaction rate constant used in the reactor model, shown in Eq. 3.3, has a temperature dependent term that was combined into the pre-exponential factor *A* since all tests were performed at room temperature. Testing at different temperatures could help uncover the activation energy of the reaction. The temperature of the surface could also be increased after a sample had been saturated to test for desorption. An experimental setup is currently being constructed where the sample rods will be replaced with sample tubes and a cartridge heater can be placed inside the sample to deliver a constant heat flux or be controlled to keep the temperature of the surface constant. Figure 7.1 shows the schematic of the planned experimental apparatus.

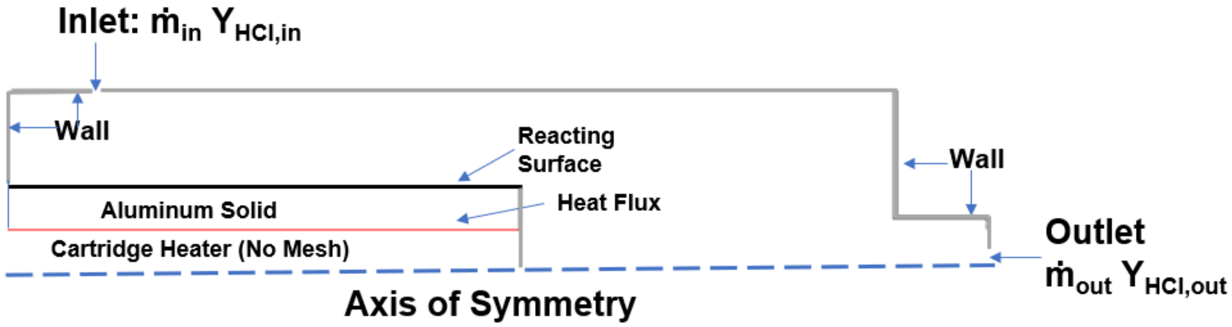

Figure 7.1: Schematic of planned experiment to adjust sample surface temperature.

The smoke from combustion products often includes solid particles, usually containing carbonaceous soot and other aerosols. Wang et al. [83] was able to find differences in particle size distribution from solid fuels burned on the ground vs. in 0-g. Meyer [84] has studied such aerosols that form during combustion in microgravity, and that exist outside of combustion on the ISS. She found dust and aerosols that include metal oxides, such as TiO_2 which is ubiquitous in many consumer products. It is likely that these particles also interact with HCl, further complicating the transport of acid gas. Huynh and McNeill [85] studied the interaction between HCl and $CaCO_3$ aerosols, which often serve as an idealized proxy for calcium rich mineral dust, finding uptake coefficients up to 0.012. Setyan et al. [86] developed experiments in a Knudsen flow reactor showing that solid particles that are present in smoke, such as soot, carbon, and dust, as well as TiO_2 nanoparticles uptake polar molecules, such as HCl and H_2O. Uptake of HCl by aerosols of similar particle density and elemental composition to what is formed during a microgravity fire should be studied. The large-scale ground facility is already designed to flow smoke and aerosols, but more work is needed in a small-scale setting to artificially create the type of smoke on the ground that is created in 0-g, and to test this smoke with HCl in the small-scale reactor.

The Saffire V campaign events involved HF bottle releases, analogous to the Saffire IV bottle releases. The results from this series of tests are presented in Fig. 7.2. The standalone HF release produced no response from the FFD, exactly like the first HCl release in Saffire IV. The second HF release burned a cotton sample concurrently, producing a slight response of HF. Two PMMA burns that did not produce HF or release any HF saw even more of a response, but not nearly as much of a response as the PMMA burn in Saffire IV. There seems to be more uptake of HF than HCl by spacecraft surfaces when comparing results of the large-scale microgravity tests. While the spacecraft is identical in both cases and the cargo configuration is similar, small changes in cargo configuration or atmospheric conditions could be the reason for the difference in acid gas response by the sensor. Small scale tests in the reactor and modeling could help determine if there is a major difference in uptake rate of HF as compared to HCl. Work is currently underway to test the uptake of HF by the same surfaces tested with HCl.

NASA is planning to return to the Moon in the near future, with plans to build habitats on both the Lunar surface and eventually Mars. The models developed in this work could be used to predict the fate of acid gases produced by a fire in such environments. Temperature gradients from the fire in this case would affect both the flow of gas and particles, as well as surface interactions due to gravity, and such thermal effects would have to be accommodated in the models.

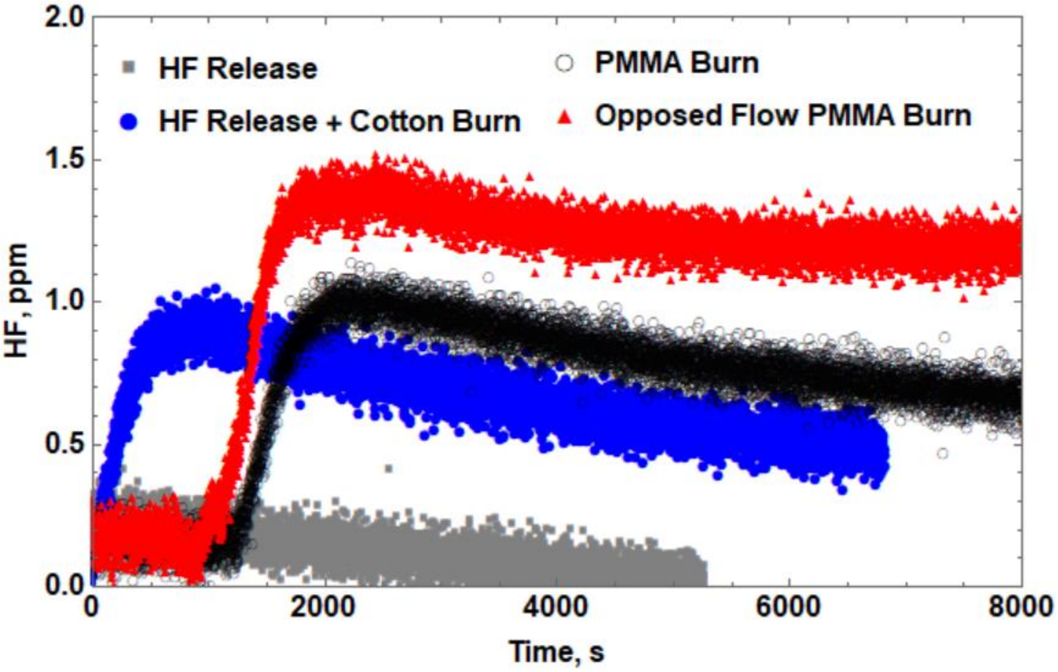

Figure 7.2: HF uptake data from Saffire V test.

Bibliography

[1] Dietrich, D. L., Niehaus, J., Ruff, G., Urban, D., Takahashi, F., Easton, J., Abbott, A., and Graf, J., “Determination of Survivable Fires,” *42nd International Conference on Environmental Systems*, AIAA-2012-3512, 2012.

[2] Miller, F., Olson, S., Johnston, J., and Niehaus, J., “Spacecraft Materials Fire Safety,” NASA-TM-2021-0022397, 2021.

[3] Guibaud, A., Legros, G., Consalvi, J. L., and Torero, J., “Fire safety in spacecraft: Past incidents and Deep Space challenges,” *Acta Astronautica*, Vol. 195, 2022, pp. 344 -354.

[4] Friedman, R., “Risks and issues in fire safety on the space station,” Probabilistic Safety and Management Conference, NASA Technical Memorandum 106430, 1993.

[5] Friedman, R., and Sacksteder. K., “Science and technology issues in spacecraft fire safety,” NASA Technical Memorandum 88933, 1987.

[6] Meyer, Marit E., "Particle Morphology and Elemental Composition of Smoke Generated by Overheating Common Spacecraft Materials,” NASA-TM-2015-218912, 2015.

[7] Stahn, A. C., Werner, A., Opatz, O., Maggioni, M. A., Steinach, M., von Ahlefeld, V. W., Moore, A., Crucian, B., E., Smith, S. M., Zwart, S. R., Schlabs, T., Mendt, S., Trippel, T., Koralewski, E., Koch, J., Chouker, A., Reitz, G., Shang, P., Rocker, L., Kirsch, K. A., and Gunga, H. C., “Increased core body temperature in astronauts during long-duration space missions,” *Scientific reports*, Vol. 7.1, 2017, pp. 1-8.

[8] Belobrajdic, B., Melone, K., and Diaz-Artiles, A., “Planetary extravehicular activity (EVA) risk mitigation strategies for long-duration space missions,” *npj Microgravity*, Vol. 7, 2021, Article 16.

[9] Pierson, D. L., “Microbial Contamination in the Spacecraft,” JSC-CN-6439, June 2001.

[10] Pierson, D. L., Botkin, D. J., Bruce, R. J., Castro, V. A., Smith, M. J., Oubre, C. M., and Ott, C. M., “Microbial monitoring of the international space station,” JSC-CN-28760, May 2013.

[11] Urban, D. L., Dietrich, D. L., Booker, J. E., Meyer, M. E., & Ruff, G. A., “Fire Detection tradeoffs as a function of Vehicle Parameters,” GRC-E-DAA-TN32263, 2016.

[12] Fortenberry, C., Casteel, M., Graf, J., Easton, J., Niehaus, J., Meyer, M., Urban, D., Ruff, G., “Evaluation of Combustion Products from Large-Scale Spacecraft Fires during the Saffire-IV and Saffire-V Experiments,” *50th International Conference on Environmental Systems*, ICES-2021-244, Texas Tech University Libraries, 2021.

[13] Ruff, G. A., Urban, D. L., Fernandez-Pello, A. C., T'ien, J. S., Torero, J. L., Legros, G., Eigenbrod, C., Smirnov, N., Fujita, O., Cowlard, A. J., Rouvreau, S., Minster, O., Toth, B., and Jomaas, G., "Spacecraft Fire Experiment (Saffire) Development Status," *44th International Conference on Environmental Systems*, ICES-2014-265, Texas Tech University Libraries, 2014.

[14] Jomaas, G., Torero, J. T., Eigenbrod, C., Niehaus, J., Olson, S. L., Ferkul, P. V., Legros, G., Fernandez-Pello, C., Cowlard, A. J., Rouvreau, S., Smirnov, N., Fujita, O., T'ien, J. S., Ruff, G. A., and Urban, D. L., "Fire Safety in Space – Beyond Flammability Testing of Small Sample," *Acta Astronautica*, Vol. 109, 2015, pp. 208-216.

[15] Ferkul, P. V., Olson, S., Urban, D. L., Ruff, G. A., Easton, J., T'ien, J. S., Liao, Y.-T. T., Fernandez-Pello, A. C., Torero, J. L., Eigenbrod, C., Legros, G., Smirnov, N., Fujita, O., Rouvreau, S., Toth, B., and Jomaas, G., "Results of Large-Scale Spacecraft Flammability Tests," *47th International Conference on Environmental Systems*, ICES-2017-224, Texas Tech University Libraries, 2017.

[16] Thomsen, M., Fernandez-Pello, A. C., Urban, D. L., Ruff, G. A., and Olson, S. L. "Upward Flame Spread over a Thin Composite Fabric: The Effect of Pressure and Microgravity," *48th International Conference on Environmental Systems*, ICES-2018-231, Texas Tech University Libraries, 2018.

[17] Xiaoyang, Z., Liao, Y-T., T., Johnston, M.C., James, S., Ferkul, P., V., and Olson, S., L., "Concurrent flame growth, spread, and quenching over composite fabric samples in low speed purely forced flow in microgravity," *Proceedings of the Combustion Institute*, Vol. 36.2, 2017, pp. 2971-2978.

[18] Urban, D., Ruff, G., Ferkul, P., Owens, J., Olson, S., Meyer, M., Fortenberry, C., Brooker, J., Graf, J., Casteel, M., Jomaas, G., Toth, B., Eigenbrod, C., T'Ien, J., Liao, Y.-T., Fernandez-Pello, C., Meyer, F., Legros, G., Guibaud, A., Smirnov, N., and Fujita, O., "Preliminary Results from Saffire IV and V Experiments on Large Scale Spacecraft Fires," 50th *International Conference on Environmental Systems*, ICES-2021-266, Texas Tech University Libraries, 2021.

[19] Beitel, J. J., Bertelo, C. A., Carroll Jr, W. F., Gardner, R. O., Grand, A. F., Hirschler, M. M., and Smith, G. F., "Hydrogen Chloride Transport and Decay in a Large Apparatus I. Decomposition of Poly (Vinyl Chloride) Wire Insulation in a Plenum by Current Overload," *Journal of fire sciences*, Vol. 4.1, 1986, pp. 15-41.

[20] Galloway, F. M., and Hirschler, M. M., "Hydrogen chloride release from poly (vinyl chloride): model for its decay," *European polymer journal*, Vol. 23.9, 1987, pp. 667-676.

[21] Galloway, F. M., and Hirschler, M. M., "A model for the spontaneous removal of airborne hydrogen chloride by common surfaces," *Fire Safety Journal*, Vol. 14.4, 1989, pp. 251-268.

[22] Galloway, F. M., Hirschler, M. M., and Smith, G. F., “Surface parameters from small-scale experiments used for measuring HCl transport and decay in fire atmospheres,” *Fire and materials*, Vol. 15.4, 1991, pp. 181-189.

[23] Galloway, F. M., and Hirschler, M. M., “The use of a model for hydrogen chloride transport and decay to predict airborne hydrogen chloride concentrations in a full-scale room-corridor scenario,” *Fire safety journal*, Vol. 19.1, 1992, pp. 73-101.

[24] Tsai, C. J., Huang, C. H., and Lu, H. H., “Adsorption capacity of a nylon filter of filter pack system for HCl and HNO3 gases,” *Separation science and technology*, Vol. 39.3, 2005 pp. 629-643.

[25] Friel, J. J. “Atmospheric corrosion products on Al, Zn and AlZn metallic coatings,” *Corrosion*, Vol. 42.7, 1986, pp. 422-426.

[26] Kumar, C. S., Mayanna, S. M., Mahendra, K. N., Sharma, A. K., and Rani, R. U., “Studies on white anodizing on aluminum alloy for space applications,” *Applied Surface Science*, Vol. 151.3-4, 1999, pp. 280-286.

[27] Pugel, D. B., Rummel, J. R., and Conley, C., “Tiny houses: Planetary protection-focused materials selection for spaceflight hardware surfaces,” *2016 IEEE Aerospace Conference*, IEEE, New York, 2016.

[28] Zähr, J., Oswald, S., Türpe, M., Ullrich, H. J., and Füssel, U., “Characterisation of oxide and hydroxide layers on technical aluminum materials using XPS,” *Vacuum*, Vol. 86.9, 2012, pp. 1216-1219.

[29] Wittberg, T. N., Wolf, J. D., and Wang, P. S., “Aluminium hydroxide growth on aluminium surfaces exposed to an air/1% NO 2 mixture,” *Journal of materials science*, Vol. *23*.5, 1988, pp, 1745-1747.

[30] De la Fuente, D., Otero-Huerta, E., and Morcillo, M., “Studies of long-term weathering of aluminium in the atmosphere,” *Corrosion Science*, Vol. *49*.7, 2007, 3134-3148.

[31] Schuttlefield, J. D., Cox, D., and Grassian, V. H., “An investigation of water uptake on clays minerals using ATR-FTIR spectroscopy coupled with quartz crystal microbalance measurements,” *Journal of Geophysical Research: Atmospheres*, Vol. 112.D21. 2007. pp. 303-317.

[32] Al-Abadleh, H. A., and Grassian, V. H., “FT-IR study of water adsorption on aluminum oxide surfaces,” *Langmuir*, Vol. 19.2, 2003, pp. 341-347.

[33] Volpe, L., “A Technique for Measuring Adsorption of Gases on Flat Surfaces,” *Proceedings of the 10th International Congress on Metallic Corrosion*, 1987, pp. 4091-4097.

[34] Hunter, M. S., and Fowle, P., “Natural and thermally formed oxide films on aluminum,” *Journal of the Electrochemical Society*, Vol. 103.9, 1956, pp. 482-485.

[35] Peri, J. B., and Hannan, R. B., “Surface hydroxyl groups on γ-alumina,” *The Journal of Physical Chemistry,* Vol. 64.10, 1960, pp. 1526-1530.

[36] Santschi, C., and Rossi, M. J., “Uptake of CO2, SO2, HNO3 and HCl on calcite (CaCO3) at 300 K: Mechanism and the role of adsorbed water,” *The Journal of Physical Chemistry A*, Vol. 110.21, 2006, pp. 6789-6802.

[37] McCafferty, E., “Sequence of steps in the pitting of aluminum by chloride ions,” *Corrosion Science,* Vol. 45.7, 2003, pp. 1421-1438.

[38] Carruthers, J. D., Payne, D. A., Sing, K. S. W., and Stryker, L. J., “Specific and nonspecific interactions in the adsorption of argon, nitrogen, and water vapor on oxides,” *Journal of Colloid and Interface Science,* Vol. 36.2, 1971, pp. 205-216.

[39] Bailey, R. R., and J. P. Wightman. “Interaction of gaseous hydrogen chloride and water with oxide surfaces: I. Alumina,” *Journal of Colloid and Interface Science*, Vol. 70.1, 1979, pp. 112-123.

[40] Alwitt, R. S. “The growth of hydrous oxide films on aluminum,” *Journal of the Electrochemical Society,* Vol. 121.10, 1974, pp. 1322-1328.

[41] Itaya, K., Sugawara, S., Arai, K., and Saito, S., “Properties of porous anodic aluminum oxide films as membranes,” *Journal of chemical engineering of Japan,* Vol. 17.5, 1984, pp. 514-520.

[42] Li, F., Zhang, L., and Metzger, R. M., “On the growth of highly ordered pores in anodized aluminum oxide,” *Chemistry of materials,* Vol. 10.9, 1998, pp. 2470-2480.

[43] Lira, H., & Paterson, R., “New and modified anodic alumina membranes: Part III. Preparation and characterisation by gas diffusion of 5 nm pore size anodic alumina membranes,” *Journal of membrane science,* Vol. 206.1-2, 2002, pp. 375-387.

[44] Chen, Z., and Lu, C., “Humidity sensors: a review of materials and mechanisms,” *Sensor letters*, Vol. 3.4, 2005, pp, 274-295.

[45] Nahar, R. K., “Study of the performance degradation of thin film aluminum oxide sensor at high humidity,” *Sensors and Actuators B: Chemical*, Vol. 63, 2000, pp. 49-54.

[46] Peng, D., Jensen, C. D., Juliano, T. J., Gregory, J. W., Crafton, J., Palluconi, S., and Liu, T., “Temperature-compensated fast pressure-sensitive paint,” *AIAA journal*, Vol. 51.10, 2013, pp. 2420-2431.

[47] Jani, A., Losic, D., and Voelcker, N., “Nanoporous anodic aluminium oxide: Advances in surface engineering and emerging applications,” *Progress in Materials Science*, Vol. 58.5, 2013, pp. 636-704.

[48] Kameda, T., Uchiyama, N., Park, K. S., Grause, G., and Yoshioka, T., “Removal of hydrogen chloride from gaseous streams using magnesium–aluminum oxide,” *Chemosphere*, Vol. 73.5, 2008, pp. 844-847.

[49] Kameda, T., Yoshioka, T., Hoshi, T., Uchida, M., and Okuwaki, A., “The removal of chloride from solutions with various cations using magnesium–aluminum oxide,” *Separation and Purification Technology*, Vol. 42.1, 2005, pp. 25-29.

[50] Cao, J., Zhong, W., Jin, B., Wang, Z., and Wang, K., “Treatment of hydrochloric acid in flue gas from municipal solid waste incineration with Ca–Mg–Al mixed oxides at medium–high temperatures,” *Energy & fuels* Vol. 28.6, 2014, pp. 4112-4117.

[51] Paereli, S., “Sorption of Hydrogen Chloride on Solid Sorbents,” M.S. Thesis, Chemical Engineering Dept., Norwegian Univ. of Science and Technology, Trondheim, Norway, 2015.

[52] Digne, M., Raybaud, P., Sautet, P., Guillaume, D., and Toulhoat, H., “Atomic scale insights on chlorinated γ-alumina surfaces,” *Journal of the American Chemical Society*, Vol. 130.33, 2008, pp. 11030-11039.

[53] Deutschmann, O., Behrendt, F., and Warnatz J., “Modelling and simulation of heterogeneous oxidation of methane on a platinum foil,” *Catalysis Today*, Vol. 21.2-3, 1994, pp. 461-470.

[54] Coltrin, M. E., Kee, R. J., and Rupley, F. M., “Surface chemkin: A general formalism and software for analyzing heterogeneous chemical kinetics at a gas-surface interface,” *International Journal of Chemical Kinetics*, Vol. 23.12, 1991, pp. 1111-1128.

[55] Cofer III, W. R., Pellett, G. L., Sebacher, D. I., and Wakelyn, N. T., “Surface chloride salt formation on space shuttle exhaust alumina,” *Journal of Geophysical Research: Atmospheres*, Vol. 89.D2, 1984, pp. 2535-2540.

[56] Scamans, G. M., and Rehal, A. S., “Electron metallography of the aluminium-water vapour reaction and its relevance to stress-corrosion susceptibility,” *Journal of Materials Science*, 14.10, 1979, pp. 2459-2470.

[57] Kytökivi, A., Lindblad, M., and Root, A., “IR and 1 H NMR studies on the adsorption of gaseous hydrogen chloride on γ-alumina,” *Journal of the Chemical Society, Faraday Transactions*, Vol. 91.5, 1995, pp. 941-948.

[58] Bausach, M., Krammer, G., and Cunill, F., “Reaction of Ca (OH) 2 with HCl in the presence of water vapour at low temperatures,” *Thermochimica acta*, Vol. 421.1-2, 2004, pp. 217-223.

[59] Peterson, G. W., and Rossin, J. A., “Removal of chlorine gases from streams of air using reactive zirconium hydroxide based filtration media,” *Industrial & engineering chemistry research*, Vol. 51.6, 2012, pp. 2675-2681.

[60] Bailey, R. R., and Wightman, J. P., “Interaction of hydrogen chloride with alumina,” NASA-CR-2929. 1978.

[61] Stadie, N. P., “Synthesis and Thermodynamic Studies of Physisorptive Energy Storage Materials,” Ph.D. Dissertation, Engineering and Applied Science Division, California Institute of Technology, 2013.

[62] Elam, J. W., Nelson, C. E., Tolbert, M. A., and George, S. M., “Adsorption and Desorption of HCl on a Single-Crystal α-Al2O3 (0001) Surface,” Surface Science, Vol. 450, Nos. 1–2, 2000, pp. 64–77.

[63] Weston, G. F., *Ultrahigh vacuum practice*, Elsevier, 2013.

[64] Hofmann, S., *Auger-and X-ray photoelectron spectroscopy in materials science: a user-oriented guide*, Vol. 49, Springer Science & Business Media, 2012.

[65] Kloprogge, J. T., and Wood, B. J., “*Handbook of Mineral Spectroscopy: Volume 1: X-ray Photoelectron Spectra,”* Elsevier, 2020.

[66] Doss, S. K., and Condas, G. A., “Atmospheric corrosion of magnetic-film structures,” *Metallurgical Transactions A*, Vol. 18.1, 1987, pp. 158-161.

[67] Iannuzzi, M., “Bias Humidity Performance and Failure Mechanisms of Nonhermetic Aluminum SIC's in an Environment Contaminated with Cl_2,” *IEEE Transactions on Components, Hybrids, and Manufacturing Technology*, Vol. 6.2, 1983, pp. 191-201.

[68] Graedel, T.E., “Corrosion mechanisms for aluminum exposed to the atmosphere,” *Journal of the Electrochemical Society*, Vol. 136.4, 1989, pp. 204C-212C.

[69] O’Mara, M. M., “Combustion of PVC,” *Pure and Applied Chemistry*, Vol. 49.5, 1977, pp. 649–660.

[70] Bird, R.B., Stewart, W.E., and Lightfoot, E.N., “*Transport Phenomena*,” 2nd ed., Wiley, 2001.

[71] Mazumder, S. and Lowry, S.A, “The Treatment of Reacting Surfaces for Finite-Volume Schemes on Unstructured Meshes,” *Journal of Computational Physics*, Vol. 173.2, 2001, pp. 512-526.

[72] Mazumder, S., *Numerical methods for partial differential equations: finite difference and finite volume methods*, Academic Press, 2016.

[73] Casanova, F., Chiang, C. E., Li, C. P., Roshchin, I. V., Ruminski, A. M., Sailor, M. J., and Schuller, I. K., “Gas adsorption and capillary condensation in nanoporous alumina films,” *Nanotechnology*, Vol. 19.31, 2008, pp. 315709-315714.

[74] Bruschi, L., Mistura, G., Liu, L., Lee, W., Gösele, U., and Coasne B., “Capillary condensation and evaporation in alumina nanopores with controlled modulations,” *Langmuir*, Vol. 26.14, 2010, pp. 11894-11898.

[75] Leaist, D. G., “Absorption of chlorine into water,” *Journal of solution chemistry*, Vol. 15.10, 1986, pp.827-838.

[76] Tang, M. J., Cox, R. A., and Kalberer, M., “Compilation and evaluation of gas phase diffusion coefficients of reactive trace gases in the atmosphere: volume 1 Inorganic compounds,” *Atmospheric Chemistry and Physics*, Vol. 14.17, 2014, pp. 9233-9247.

[77] Mian, A. A., “Measurement of binary gaseous diffusion coefficients of polar system*,”* MS thesis, Chemical Engineering Dept., University of British Columbia, 1962.

[78] Climent, M. A., de Vera, G., López, J. F., Viqueira, E., and Andrade, C., “A test method for measuring chloride diffusion coefficients through nonsaturated concrete: Part I. The instantaneous plane source diffusion case,” *Cement and concrete Research*, Vol. 32.7, 2002, pp. 1113-1123.

[79] de Vera, G., Climent, M. A., Viqueira, E., Antón, C., and Andrade, “A test method for measuring chloride diffusion coefficients through partially saturated concrete. Part II: The instantaneous plane source diffusion case with chloride binding consideration,” *Cement and concrete research*, Vol. 37.5, 2007, pp. 714-724.

[80] Saetta, A. V., Scotta, R. V., and Vitaliani, R. V., “Analysis of chloride diffusion into partially saturated concrete,” *Materials Journal*, Vol. 90.5, 1993, pp. 441-451.

[81] Zhao, C., Dong, Y., Feng, Y., Li, Y., and Dong, Y., “Thermal desorption for remediation of contaminated soil: A review,” *Chemosphere*, Vol. 221, 2019, pp. 841-855.

[82] de Percin, P. R., “Application of thermal desorption technologies to hazardous waste sites,” Journal of Hazardous materials, Vol 40.2, 1995, pp. 203-209.

[83] Wang, X., Zhou, H., Arnott, W. P., Meyer, M. E., Taylor, S., Firouzkouhi, H., Moosmuller, H., Chow, J. C., and Watson, J. G., “Characterization of smoke for spacecraft fire safety,” *Journal of Aerosol Science*, Vol. 136, 2019, pp. 36-47.

[84] Meyer, M. E., “Further characterization of aerosols sampled on the international space station,” GRC-E-DAA-TN67302, July 2019.

[85] Huynh, H. N., and McNeill, V. F., “Heterogeneous Chemistry of CaCO3 Aerosols with HNO3 and HCl,” *The Journal of Physical Chemistry A*, Vol. 124.19, 2020, pp. 3886-3895.

[86] Setyan, A., Sauvain, J. J., and Rossi, M. J., “The use of heterogeneous chemistry for the characterization of functional groups at the gas/particle interface of soot and TiO 2 nanoparticles,” *Physical Chemistry Chemical Physics*, Vol. 11.29, 2009, pp. 6205-6217.